NTNU
Norwegian University of
Science and Technology

# Damage Assessment of Sevan 1000 FPSO Subjected to Impacts from Shuttle Tankers

Stian Arneborg Hagen

Marine Technology
Submission date: June 2018
Supervisor: Jørgen Amdahl, IMT
Co-supervisor: Zhaolong Yu, IMT

Norwegian University of Science and Technology
Department of Marine Technology

**NTNU**
**Norges teknisk-naturvitenskapelige universitet**
*Institutt for marin teknikk*

MASTER THESIS SPRING 2018

for

Stud. techn. Stian Arneborg Hagen

**Damage assessment of Sevan 1000 FPSO subjected to impacts from shuttle tankers**
*Skadevurdering av Sevan 1000 FPSO utsatt for støt fra skytteltankere*

In deep water - drilling for and production of oil and gas - use of floating platforms/FPSOs are the only viable solutions. The Sevan marine design has proved to be an efficient concept. In many remote fields the only practical possibility for oil transfer to shore is via off take tankers based on tandem offloading or via a single point mooring system. Tandem offloading has shown to be the most economical alternative in this respect. In tandem offloading, the shuttle tanker is moored to the FPSO by hawsers and/or Dynamic Positioning (DP), while the cargo is off loaded through floating hoses. Comment: For the Sevan concept the base case offloading scenario is with a shuttle tanker on DP – i.e. no hawser – and in addition the offloading hose is not a floating hose.

The use of tankers for offshore loading implies risk for various types of collision:

- Collision of powered or drifting tanker with installation (FPSO). This can be treated as for collisions for other passing vessels with platforms, defining the tanker route as part of the shipping traffic data. This scenario is treated as a passing vessel.
- Collision of shuttle tanker with FPSO during offloading. This may be due to human error or machinery failure on approach or due to a mooring or Dynamic Positioning (DP) failure during offloading operations.

The latter scenario was studied among others for the Penguin project by Reinertsen Engineering in 2016. The work showed that the platform had good collision resistance against the selected collision scenarios. The idea of the present Project/Master thesis work is to conduct collision analysis of Sevan 1000 FPSO with the non-linear finite element method (NLFEA). The study shall also include glancing impacts. The results shall be compared with those obtained with simplified methods.

It is recommended to carry out the work in the following steps:

1) Perform an evaluation of the range of impact scenarios taking into account the draft variations of both the FPSO and the shuttle tanker. Prepare also an overview of potential impact scenarios for a supply vessel.

2) Create a finite element model of the Sevan 1000 FPSO for collision assessment with LS-DYNA. This may contain a section modelled in detail with a fine element mesh that captures local damage and a simplified section consisting of large equivalent shell element needed that captures rigid body motions. Discuss how boundary conditions between the detailed and crude section can be modelled properly. Discuss how added mass and damping forces can be represented in the model.

3) Establish the ship model for the tanker and a supply vessel. This model should also represent rigid body motions with the effect of hydrodynamic forces included.

4) Perform finite element simulations of shuttle tanker impact with the coupled model. Describe the damage pattern in the FPSO and the tanker. Establish collision speed limits for penetration into void spaces. Evaluate the stability of the buoy with flooded compartments.

5) Compare the results of the integrated analysis with those predicted by the external mechanics model. Key issues are the rigid body motion components induced by the collision and the demand for energy dissipation. What is the benefit of taking all motion components as sway, surge, roll and yaw into account compared to more fixed directions? Discuss also the significance of the tangential friction in the simplified model; shall it also account for transverse structural damage? Check also if existing simple damage formulations can be used to for internal mechanics assessments.

6) Investigate the sensitivity of the damage prediction using an alternative bow model or by changing some of the parameters of the existing bow model (e.g. ice strengthening may be simulated with increased yield stress and/or modification or plate thickness or intermediate stiffeners.

7) Perform simulation of supply vessel impacts using existing finite element models. Describe the damage in terms of plastic defamations and potential rupture of the shell plating.

8) Conclusions and recommendations for further work.

Literature studies of specific topics relevant to the thesis work may be included.

The work scope may prove to be larger than initially anticipated. Subject to approval from the supervisors, topics may be deleted from the list above or reduced in extent.

In the thesis the candidate shall present his personal contribution to the resolution of problems within the scope of the thesis work.

Theories and conclusions should be based on mathematical derivations and/or logic reasoning identifying the various steps in the deduction.

The candidate should utilise the existing possibilities for obtaining relevant literature.

**Thesis format**
The thesis should be organised in a rational manner to give a clear exposition of results, assessments, and conclusions. The text should be brief and to the point, with a clear language. Telegraphic language should be avoided.

The thesis shall contain the following elements: A text defining the scope, preface, list of contents, summary, main body of thesis, conclusions with recommendations for further work, list

of symbols and acronyms, references and (optional) appendices. All figures, tables and equations shall be numerated.

The supervisors may require that the candidate, in an early stage of the work, presents a written plan for the completion of the work. The plan should include a budget for the use of computer and laboratory resources, which will be charged to the department. Overruns shall be reported to the supervisors.

The original contribution of the candidate and material taken from other sources shall be clearly defined. Work from other sources shall be properly referenced using an acknowledged referencing system.

The report shall be submitted in two copies:

- Signed by the candidate
- The text defining the scope included
- In bound volume(s)
- Drawings and/or computer prints which cannot be bound should be organised in a separate folder.
- The report shall also be submitted in pdf format along with essential input files for computer analysis, spreadsheets, Matlab files etc in digital format.

**Ownership**
NTNU has according to the present rules the ownership of the thesis. Any use of the thesis has to be approved by NTNU (or external partner when this applies). The department has the right to use the thesis as if the work was carried out by a NTNU employee, if nothing else has been agreed in advance.

A Sevan Marine design will be utilized in the thesis work. With the intention of allowing the results of the thesis work publicly available, Sevan Marine reserves the right to ensure that commercially sensitive information is not included in the public part of the thesis. If such issues should arise, confidential information is suggested to be included as an appendix, which is omitted from the openly available thesis.

**Thesis supervisor**
Prof. Jørgen Amdahl
Post Doc Zhaolong Yu

Contact person at Sintef Oceans: Hagbart Alsos

Contact person at Sevan Marine: Audun Nyhus

**Deadline**
June 11, 2018

Trondheim, January 15, 2018
Jørgen Amdahl

# Preface

This report is a master thesis within the field of marine technology. The work was carried out during the spring semester of 2018 at the Norwegian University of Science and Technology (NTNU) in Trondheim. The topic in this thesis is based on proposals from the company Sevan Marine ASA and inputs from the supervisors. Sevan Marine contributed with structural drawings of the Sevan 1000 FPSO and assistance when needed.

The original idea was to study the damage in the Sevan 1000 FPSO when subjected to impacts from shuttle tankers and supply vessels by using a coupled approach. However, a large portion of the time was spent on modelling the FPSO, thus limited time were available for implementing the coupled model in LS-DYNA. In addition, the very large size of the FPSO model resulted in problems when running simulations on the cluster computer Vilje. Nevertheless, I am very happy with the end result.

I would like to thank my supervisors, Prof. Jørgen Amdahl and Post Doc. Zhaolong Yu for excellent guidance throughout both the project thesis and the master thesis. I also wish to thank Post Doc. Yanyan Sha for help with modelling and LS-DYNA simulations, Dr. Martin Storheim for providing the "GeniE-to-Dyna" Python code, Aanund B. Berdal from DNV-GL for excellent help with Sesam GeniE, Audun Nyhus and Tord Broms Thorsen from Sevan Marine ASA for input to the project, and finally my fellow students and friends Erlend Flatøy, Terje S. Bøe, Jorge L. Rangel, Sondre S. Midtbust and Alice Gudem for countless discussions and help when needed.

Stian Arneborg Hagen
Trondheim, June 11, 2018

# Summary

Floating, production, storage and offloading (FPSO) units are the only viable option for oil and gas production in deep waters. Shuttle tankers are normally employed for cargo transfer because they are the most practical solution in remote fields. Cargo offloading can be performed in a tandem configuration where the shuttle tanker is positioned a distance behind the FPSO. During the long-lasting offloading process, various types of failures may result in drive-off and drift-off impact scenarios. Collisions between shuttle tankers and FPSOs are fortunately rare events, but in the case of an accident, the outcome can be catastrophic.

The cylindrical Sevan FPSO concept is designed with respect to i.a. motion characteristics and structural resistance to potential impacts. In this thesis, the damage in the Sevan 1000 FPSO when subjected to impacts from a 150,000 deadweight tonnage shuttle tanker and two types of supply vessels was studied. The emphasis was on shuttle tanker impacts. The objective was to determine the energy dissipation involved in drive-off impacts and to study the relative strength and the local structural response in the striking ship and the struck FPSO.

Impact scenarios were defined by upper limit drive-off velocities and drafts corresponding to the initial and final offloading phase. Both head-on and glancing (non-central) impacts were studied for each scenario. A finite element model of the Sevan 1000 FPSO was created in the software Sesam GeniE and imported into the numerical code LS-DYNA for non-linear finite element analysis.

A decoupled approach was applied for assessment of shuttle tanker impacts, which means that external rigid body dynamics and local structural deformations are studied separately. It was found from analysis of central impacts that the maximum dissipated energy is 204 MJ in the initial offloading phase and 147 MJ in the final offloading phase. For non-central impacts, it was observed that the reduction of energy dissipation is highly affected by the impact angle and a sticking-sliding mechanism, where sliding between the bodies leads to the largest reduction. For supply vessel impacts, the maximum dissipated energy was 15 MJ and 58 MJ when the initial velocity was 2 m/s and 4 m/s, respectively.

From the assessment of local structural response, it was observed that application of a shared-energy design is essential in analysis of shuttle tanker – FPSO collisions. It was found that the relative strength is dependent on the offloading phase due to draft variations. In the initial offloading phase, the shuttle tanker forecastle was crushed by the FPSO superstructure, while in the final offloading phase, the FPSO bilge box was crushed by the bulbous bow of the shuttle tanker. In summary, the main hull of the FPSO is still intact after a drive-off impact, but ruptures can occur in the bilge box and in the superstructure in specific scenarios.

Glancing supply vessel impacts were studied using a coupled model in LS-DYNA which included hydrodynamic effects. From the coupled analysis, it was found that significant pitch

and yaw motions in the striking vessel were generated by the collision process. The intensity of each component depends on the glancing impact angle. For larger angles, it was observed that the importance of frictional energy increased, thus the share of strain energy absorption will be further reduced.

# Sammendrag

Flytende produksjons-, lagrings- og losseenheter (FPSO) er det eneste levedyktige alternativet for olje- og gassproduksjon i dype farvann. Skytteltankere blir normalt benyttet for transport av olje og gass fra avsidesliggende produksjonsfelt. Losseprosessen foregår ofte i en tandemkonfigurasjon der skytteltanken er posisjonert en avstand bak FPSO. Under den langvarige losseprosessen kan ulike typer feil føre til at tankskipet kjører eller driver ut av posisjon. Kollisjoner mellom skytteltankere og FPSO er heldigvis sjeldne hendelser, men hvis en ulykkes først skjer så kan utfallet bli katastrofalt.

Det sylindriske Sevan FPSO-konseptet er designet med hensyn på blant annet bevegelsesadferd og strukturell motstand mot potensielle støt. Denne oppgaven tar for seg skaden i Sevan 1000 FPSO, utsatt for støt fra en 150.000 tonn skytteltanker og to typer forsyningsfartøy. Hovedfokuset var på skytteltankerkollisjoner. Målet med oppgaven var å bestemme energimengden som blir absorbert i ulike «drive-off» kollisjoner og videre bestemme energifordelingen mellom skipet og FPSO, samt studere den strukturelle deformasjonen.

Kollisjonsscenarioene i denne oppgaven ble definert av en øvre grense for drive-off hastighet og en dypgangsvariasjon i samsvar med start- og sluttfasen av losseprosessen. Kollisjoner hvor skipet treffer rett på og skrått på FPSOen ble studert for hvert scenario. En modell av Sevan 1000 FPSO ble laget i programvaren Sesam GeniE og importert til den numeriske løseren LS-DYNA for ikke-lineær elementanalyse.

En ukoblet metode ble anvendt i analysen av skytteltankerkollisjoner, dvs. ekstern stivt legeme dynamikk og lokal strukturell deformasjon ble analysert isolert. Analysene viste at det maksimale energiopptaket er 204 MJ for en kollisjon i startfasen av losseprosessen og 147 MJ i sluttfasen av losseprosessen. For kollisjoner hvor tankskipet treffer med en vinkel ble det observert en reduksjon av energiopptaket som var avhengig av kollisjonsvinkelen og en «sticking-sliding»-mekanisme, hvor gliding førte til den største reduksjonen. For kollisjoner med et forsyningsfartøy var det maksimale energiopptaket på 15 MJ og 58 MJ for henholdsvis 2 m/s og 4 m/s starthastigheter.

Fra analysen av lokal strukturell respons, ble det observert at antagelsen om en delt deformasjonsprosess er nødvendig for at en kollisjonsanalyse mellom en skytteltanker og en FPSO skal gi riktig resultat. Det ble observert at den relative styrken mellom objektene er avhengig av lastkondisjonene i losseprosessen. I startfasen av losseprosessen ble bakkdekket til skytteltankeren knust av FPSO-overbygget, mens i sluttfasen av losseprosessen ble kjølboksen til FPSO knust av bulben til tankskipet. Kort oppsummert så er FPSO-skroget intakt etter alle kollisjonene, men brudd og sprekker kan forekomme i kjølboksen og i overbygget i enkelte scenarioer.

Skrå støt fra forsyningsfartøy ble analysert ved hjelp av en koblet modell med hydrodynamiske

effekter i LS-DYNA. Fra den koblede analysen ble det observert at stampe- og girbevegelser blir introdusert av kollisjonen. Størrelsen til hver komponent avhenger av kollisjonsvinkelen. For store kollisjonsvinkler ble det observert at energiopptaket fra friksjon økte, slik at andelen av tøyningsenergi i det totale energiopptaket ble redusert ytterligere.

# Contents

# List of Tables

# List of Figures

# Nomenclature

| Variable | Unit | Description |
|---|---|---|
| $\vec{n}_i$ | $m$ | Local coordinate in $i$-direction |
| $\vec{r}$ | $m$ | Direction vector |
| $\alpha$ | $deg.$ | Waterline angle |
| $\beta'$ | $deg.$ | Normal frame angle |
| $\theta$ | $deg.$ | Angle between global coordinate systems |
| $\mu_n$ | $-$ | Normal friction factor |
| $\mu_t$ | $-$ | Tangential friction factor |
| $dp_i$ | $Ns$ | Impulse increment in $\vec{n}_i$-direction |
| $\mu_0$ | $-$ | Static friction coefficient |
| $E_i$ | $J$ | Dissipated energy in $\vec{n}_i$-direction |
| $\overline{m}_i$ | $kg$ | Equivalent mass in $\vec{n}_i$-direction |
| $\Delta v_i$ | $m/s$ | Change in relative velocity in $\vec{n}_i$-direction |
| $m_i j$ | $kg$ | element $i j$ in the mass matrix |
| $v_i^0$ | $m/s$ | Initial relative velocity in $\vec{n}_i$-direction |
| $e$ | $-$ | Coefficient of restitution |
| $dv_i$ | $m/s$ | Change in relative velocity in $\vec{n}_i$-direction |
| $\Delta$ | $-$ | Increment |
| $\mathbf{R}$ | $-$ | External load vector |
| $\mathbf{K_I}$ | $-$ | Incremental (tangent) stiffness matrix |
| $\mathbf{r}$ | $-$ | Nodal displacement vector |
| $\phi$ | $Pa$ | Yield function |
| $\sigma_y$ | $Pa$ | Yield stress |
| $\sigma_0$ | $Pa$ | Initial yield stress |
| $K$ | $Pa$ | Strength coefficient |
| $\epsilon_p$ | $-$ | Plastic strain |
| $n$ | $-$ | Strain hardening exponent |
| $d\sigma$ | $Pa$ | Stress increment |
| $d\epsilon$ | $-$ | Strain increment |
| $E_t$ | $Pa$ | Tangential modulus |
| $D$ | $-$ | Accumulated damage |
| $\dot{D}$ | $-$ | Damage rate |
| $\epsilon_{cr}$ | $-$ | Critical strain |
| $\sigma_{eq}$ | $Pa$ | Equivalent stress |
| $\sigma_1$ | $Pa$ | Normal stress |
| $\dot{\epsilon}_{eq}$ | $-$ | Equivalent strain rate |
| $T$ | $-$ | Stress triaxiality |

| | | |
|---|---|---|
| $\mathbf{M}$ | – | Mass matrix |
| $R^{ext}$ | – | External load vector |
| $R^{int}$ | – | Internal load vector |
| $\dot{\mathbf{r}}$ | – | Nodal velocity vector |
| $\ddot{\mathbf{r}}$ | – | Nodal acceleration vector |
| $\Delta t_{n+1}$ | $s$ | Time increment forward in time |
| $\Delta t_n$ | $s$ | Time increment backwards in time |
| $\Delta t$ | $s$ | Time-step |
| $h_e$ | $m$ | Characteristic length of element $e$ |
| $c$ | $m/s$ | Sound speed in the material |
| $E$ | $Pa$ | Young's modulus |
| $\rho$ | $kg/m^3$ | Material density |
| $m$ | $kg$ | Mass |
| $I_{zz}$ | $kgm^2$ | Moment of inertia about z-axis |
| $u$ | $m/s$ | Velocity in x-direction |
| $\dot{u}$ | $m/s^2$ | Acceleration in x-direction |
| $v$ | $m/s$ | Velocity in y-direction |
| $\dot{v}$ | $m/s^2$ | Acceleration in y-direction |
| $r$ | $rad/s$ | Angular velocity about z-axis |
| $\dot{r}$ | $rad/s^2$ | Angular acceleration about z-axis |
| $X_{hydro}$ | $N$ | Hydrodynamic force in x-direction |
| $Y_{hydro}$ | $N$ | Hydrodynamic force in y-direction |
| $N_{hydro}$ | $Nm$ | Hydrodynamic moment about z-axis |
| $X_{dist}$ | $N$ | Disturbance force in x-direction |
| $Y_{dist}$ | $N$ | Disturbance force in y-direction |
| $N_{dist}$ | $Nm$ | Disturbance moment about z-axis |
| $x_{cog}$ | $m$ | Longitudinal distance to centre of gravity |
| $\delta$ | $deg.$ | Rudder angle |
| $n$ | $rpm$ | Propeller revolution rate |
| $\rho$ | $kg/m^3$ | Sea water density |
| $\psi$ | $deg.$ | Yaw angle |
| $\mu$ | – | Engine output ratio |
| $a$ | $kg$ | Added mass |
| $V$ | $m/s$ | Velocity |
| $T$ | $N$ | Thrust |
| $F_D$ | $N$ | Drag force |
| $V_t$ | $m/s$ | Terminal velocity |
| $S$ | $m$ | Distance |
| $S_c$ | $m$ | Characteristic distance |

| | | |
|---|---|---|
| $\rho_w$ | $kg/m^3$ | Sea water density |
| $C_D$ | – | Drag coefficient |
| $A_p$ | $m^2$ | Projected area |
| $P$ | $W$ | Engine effect |
| $\eta$ | – | Overall efficency |
| $\phi$ | $deg.$ | Impact angle |
| $C_{wp}$ | – | Waterplane coefficient |
| $C_m$ | – | Mid-section coefficient |
| $C_b$ | – | Block coefficient |
| $\hat{m}_x$ | – | Added mass factor in surge |
| $\hat{m}_y$ | – | Added mass factor in sway |
| $\hat{m}_z$ | – | Added mass factor in heave |
| $\hat{j}_{xx}$ | – | Added mass factor in roll |
| $\hat{j}_{yy}$ | – | Added mass factor in pitch |
| $\hat{j}_{zz}$ | – | Added mass factor in yaw |
| $\hat{R}_{xx}$ | $m$ | Radius of gyration about x-axis |
| $\hat{R}_{yy}$ | $m$ | Radius of gyration about y-axis |
| $\hat{R}_{zz}$ | $m$ | Radius of gyration about z-axis |
| $\mu_s$ | – | Steel-to-steel friction factor |
| $\mu_d$ | – | Equivalent friction factor |

# Abbreviations

| | | |
|---|---|---|
| ALS | - | Accidental limit state |
| COG | - | Centre of gravity |
| DP | - | Dynamic positioning |
| DOF | - | Degree-of-freedom |
| DWT | - | Deadweight tonnage |
| FE | - | Finite element |
| FEA | - | Finite element analysis |
| FEM | - | Finite element method |
| FPSO | - | Floating, production, storage and offloading unit |
| HPC | - | High-performance computer |
| GUI | - | Graphical user interface |
| MPP | - | Massively parallel processing |
| NCS | - | Norwegian continental shelves |
| NLFEA | - | Non-linear finite element analysis |
| RTCL | - | Rice-Tracey Cockroft-Latham criterion |
| SMP | - | Shared memory parallel processing |
| SSP | - | Sevan Stabilized Platform |
| UKCS | - | UK continental shelves |

# Chapter 1

# Introduction

## 1.1 Background

Floating, production, storage and offloading (FPSO) units are in most cases the only viable option for oil and gas production in deep waters. Traditionally, converted tankers have been employed in less harsh environments, e.g. parts of Africa and South-Asia, however, FPSO design has evolved into withstanding tougher environments like the North Sea and the North Atlantic (Vinnem et al. 2015). The Sevan 1000 is one good example of a FPSO concept designed for operating in such harsh environments. The characteristic cylindrical hull of the Sevan 1000, as shown in figure 1.1, results in absence of weather vaning and therefore removes the need for a swivel. A large bilge box extension of the double bottom results in good motion behaviour, making the FPSO suitable for any environment.


Figure 1.1: Concept drawing of the Sevan 1000 FPSO Goliat, from Steensen (2009)

FPSOs usually operates in distant oil and gas fields. The only reasonable option for cargo transfer is therefore shuttle tankers. Cargo offloading is usually carried out in a tandem configuration, i.e. the tanker is positioned a distance behind the FPSO and connected through a hawser and a loading hose as illustrated in figure 1.2 (Chen & Moan 2004). A traditional ship-shaped FPSO rotates about the turret because of environmental loads. Positioning of the shuttle tanker is then either controlled by a dynamic positioning system (DP mode) or by applying astern thrust and a small tension on the hawser (taut hawser mode). In the North Sea, DP mode is most common (Vinnem et al. 2015).

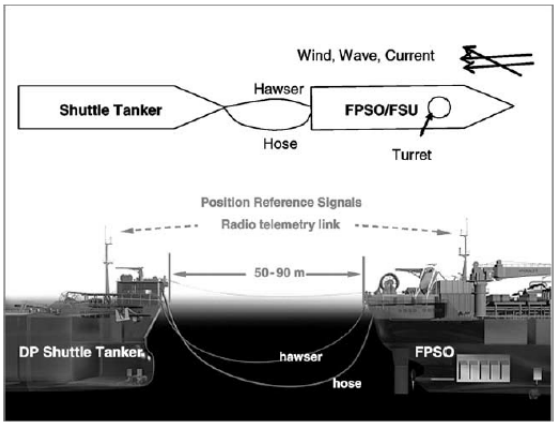


Figure 1.2: Tandem offloading configuration, from Chen & Moan (2004)

DP shuttle tankers may experience "drive-off" and "drift-off" scenarios during offloading due to technical failure or human error. Chen & Moan (2004) defines drive-off as the scenario when the tanker unintentionally drives away from its position by its own thrusters. Such a scenario may lead to a collision if the ship motion is directed towards the FPSO. Another scenario is "drift-off" due to blackout, but as stated by Chen & Moan (2004), drift-off scenarios are usually not of interest since the tanker will most likely drift away from the FPSO because of environmental loads.

Shuttle tanker - FPSO collisions are fortunately rare events, but in the case of an accident, the consequences can be catastrophic. Oil spillage, loss of platform stability, structural collapse and loss of human life are the worst-case scenarios. K. Lundborg (2014) estimated the collision frequency between DP shuttle tankers and FPSOs to be in the range of $4.5 \cdot 10^{-4}$ to $8.0 \cdot 10^{-4}$ per offloading on the UK and Norwegian continental shelves (UKCS and NCS) in the time period 1995-2013. The estimated frequency is higher than the cut-off criterion of $1.0 \cdot 10^{-4}$ accidents per platform year which is the basis in an accidental limit state (ALS) design check. Proper damage assessment, in addition to preventive actions, is therefore crucial to ensure safety at all levels.

## 1.2 Thesis objective and scope

In this master thesis, the damage in the Sevan 1000 FPSO when subjected to impacts from a 150,000 deadweight tonnage (DWT) shuttle tanker, a 7,500 DWT supply vessel and an ULSTEIN X-BOW supply vessel is studied. The damage assessment is carried out by using a coupled and decoupled approach, where the coupling is between rigid body dynamics and local structural damage.

The objective is to determine the dissipation of energy and the relative strength for a variety of drive-off scenarios during cargo offloading, and to identify the main energy absorbing parts in the striking ship and the struck FPSO. The collision scenarios include head-on central and glancing (non-central) impacts. Additional supply vessel impacts are included to study the damage from different bow geometries. Key elements of the damage assessment are:

- Energy dissipation
- Rigid body motions
- Relative strength
- Local structural response

The decoupled approach is used in the analysis of shuttle tanker and X-BOW supply vessel impacts, i.e. external dynamics and internal mechanics are studied separately. External dynamics are analysed by using a 6 degree-of-freedom (DOF) model developed by Liu & Amdahl (2010). Internal mechanics are analysed by non-linear finite element analysis (NLFEA) in the numerical code LS-DYNA. In addition, a coupled hydrodynamic model in LS-DYNA, developed by Yu & Amdahl (2016), where tested for supply vessel impacts. Originally, the coupled model was to be implemented into the NLFEA of shuttle tanker impacts. However, due to a very time-consuming process of creating the Sevan 1000 FPSO model, limited time was available for implementing the coupled model. Comparisons between the coupled and decoupled methods are thus only carried out for supply vessel impacts.

Extensive discussions regarding ice-strengthened shuttle tankers are unfortunately excluded from the thesis to limit the work load. This includes modifications of the shuttle tanker model to simulate ice strengthening. An analysis of an ice-strengthened supply vessel collision is, however, included since the X-BOW supply vessel model is ice-strengthened. Simplified methods for assessment of internal mechanics and analysis of FPSO stability with flooded compartments are omitted due to time limitations.

## 1.3 Thesis organization

**Chapter 1 - Introduction**
Chapter 1 presents background, objectives and organization of this master thesis.

**Chapter 2 - Impact Mechanics of Ship Collisions**
Chapter 2 describes the relevant theory of impact mechanics of ship collisions. This includes decoupling of the impact problem, non-linear finite element analysis and coupling between structural and hydrodynamic response.

**Chapter 3 - Impact scenarios**
Chapter 3 describes the general offloading procedure for a Sevan FPSO and addresses potential impact scenarios. The impact scenarios studied in this thesis are defined in this chapter through offloading phase, loading conditions and drive-off velocity.

**Chapter 4 - Setup for External Dynamic Analysis**
Chapter 4 presents an overview of the details regarding the external dynamic analysis, including input values, coordinate systems, hydrodynamic effects and friction factors. A MATLAB script which defines all of the input values in the external dynamic analysis is included in appendix D.

**Chapter 5 - Finite Element Models**
Chapter 5 presents the four finite element models that were used in this thesis: the FPSO model, a shuttle tanker model, a supply vessel model and a supply vessel model with X-BOW. The primary focus is on the Sevan 1000 FPSO model and the process of creating it. The striking ship models used in this thesis were pre-existing models available from the Department of Marine Technology at NTNU.

**Chapter 6 - Setup for Finite Element Analysis in LS-DYNA**
Chapter 6 describes key features of LS-DYNA which were applied in the finite element analysis. The keyword file which contains all the control settings in LS-DYNA is included in appendix C.

**Chapter 7 - Decoupled Analysis of Impacts from a Shuttle Tanker and Supply Vessels**
Chapter 7 presents the results from the decoupled analysis of shuttle tanker and supply vessel impacts. Relevant discussions are included in this chapter to improve readability with respect to figures, plots and tables. The combination of results and discussions in the same chapter was chosen based on recommendations and discussions with the supervisors.

**Chapter 8 - Coupled Analysis of Impacts from a Supply Vessel**
Chapter 8 presents the results from the coupled analysis of supply vessel impacts. Results and discussions are also combined in this chapter, similar to chapter 7.

**Chapter 9 - Conclusions and Recommendations for Future Work**

Chapter 9 concludes the thesis work and presents recommendations for future work.

**Appendix A**
Appendix A presents empirical equations for estimation of hydrodynamic coefficients for a ship.

**Appendix B**
Appendix B presents some additional force-deformation curves of shuttle tanker impacts.

**Appendix C**
Appendix C includes a LS-DYNA keyword file which contains control settings.

**Appendix D**
Appendix D includes a MATLAB script used in the external dynamic analysis.

# Chapter 2

# Impact Mechanics of Ship Collisions

## 2.1 Accidental limit state design

Classification societies have established some general criteria for assessment of accidental actions, so-called accidental limit states. The main idea behind the ALS design check is to prevent disproportional outcomes with respect to the original cause (Storheim 2016), meaning that a structure must be designed so that possible accidental loads will not cause total failure, e.g. collapse or loss of stability. However, there are a lot of uncertainties involved in ALS analyses and ALS design does not guarantee structural integrity in the case of an accident. According to Storheim (2016), the performance criteria for ship collisions concerns:

- Energy dissipation
- Local strength
- Resistance to deformation
- Ductility (to avoid cracks)

## 2.2 Relative strength

NORSOK-N004 (2004) categorizes ship-installation impacts by three relative strength scenarios: Ductile design, shared-energy design and strength design. The relationship can be seen in figure 2.1.

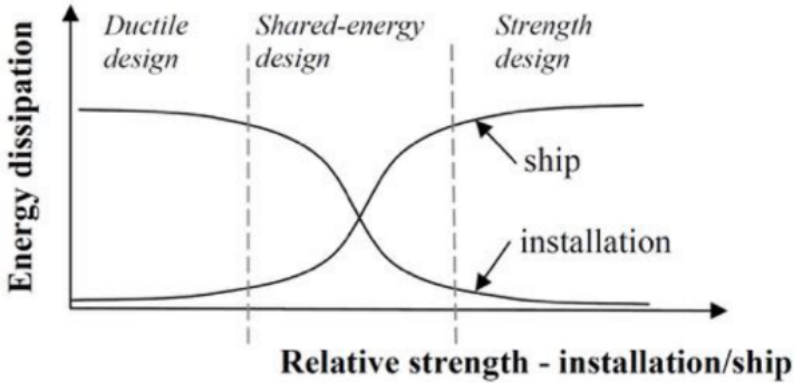


Figure 2.1: Categories of relative strength in ALS design, from NORSOK-N004 (2004)

In ductile design, the striking ship is assumed rigid, thus all energy is dissipated by the installation (the struck object). Deformations will only take place in the installation regardless of the impact scenario, thus ductile design is likely to result in oversizing. The opposite approach to ductile design is strength design where the striking ship is assumed to dissipate most of the energy. This is a reasonable assumption if the installation is designed to resist the total crushing force and local hot spots with good margin (Storheim 2016).

Shared-energy design allows significant deformations in both the striking ship and the struck installation. The instantaneously weaker body will deform and the structure that constitutes the weaker body can change throughout the deformation process. The challenge is to estimate the distribution of dissipated strain energy between the colliding bodies. A common method is to establish force-deformation curves for the bodies involved. Figure 2.2 shows a typical force-deformation diagram for a shared-energy deformation process.

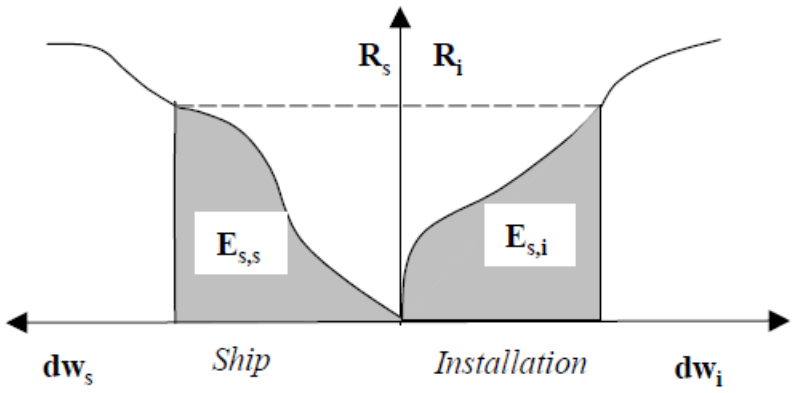


Figure 2.2: Dissipation of strain energy in ship and installation, from NORSOK-N004 (2004)

## 2.3 Decoupling of ship collision mechanics

A ship collision is a coupled process between global motions and local structural response, however in ALS design check, a common approach is to decouple the problem into two parts: *external* and *internal* mechanics (Liu & Amdahl 2010). Decoupling of the problem reduces the complexity and allows for application of simplified methods that are time-efficient. External dynamics deals with rigid body motions and energy dissipation, while internal mechanics distributes the dissipated strain energy and assesses local structural damage. The concept is illustrated in figure 2.3. The initial kinetic energy of the striking ship is absorbed as a combination of strain energy, hydrodynamic dissipation, acceleration of structural and hydrodynamic added mass, etc. (Storheim 2016), however, it is common to simplify and assume that all energy dissipation is taken as strain energy, i.e. plastic deformation. The following subsections presents methods for assessment of external and internal mechanics.

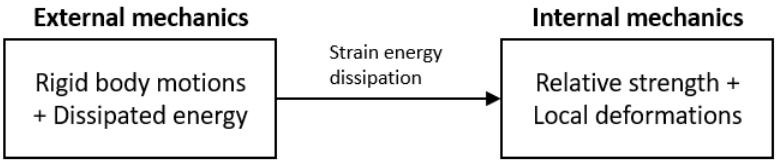


Figure 2.3: Relationship between external and internal mechanics

### 2.3.1 6DOF formulation of external mechanics

Liu & Amdahl (2010) developed a 6 degree-of-freedom (DOF) model for external dynamics of ship collisions based on the theory of three-dimensional (3D) impacts by Stronge (2004). The advantage of this model is the application of a local coordinate system at the contact point, enabling closed form solutions of the dissipated energy in each direction. The local coordinate system $(\vec{n}_1, \vec{n}_2, \vec{n}_3)$ defines a common tangent plane at the contact point (referred to as the contact surface). Two additional body fixed coordinates systems are established in the centre of gravity (COG) of the colliding bodies. The coordinate systems are illustrated in figure 2.4. A direction vector $\vec{r}$ connects the contact point and the COG.

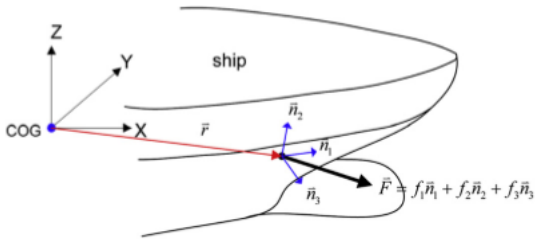


Figure 2.4: Global and local coordinate systems, from Liu & Amdahl (2010)

The orientation of the contact surface is dependent on the geometry of the master object at the contact point. The master object is selected based on relative strength; the object that is believed to deform the least and has a governing geometry, i.e. flat or slightly curved, is used as master (Liu & Amdahl n.d.). A set of hull angles defined by DNV (2016) are used to establish a transformation matrix between the local and global coordinate system. These are shown in figure 2.5.

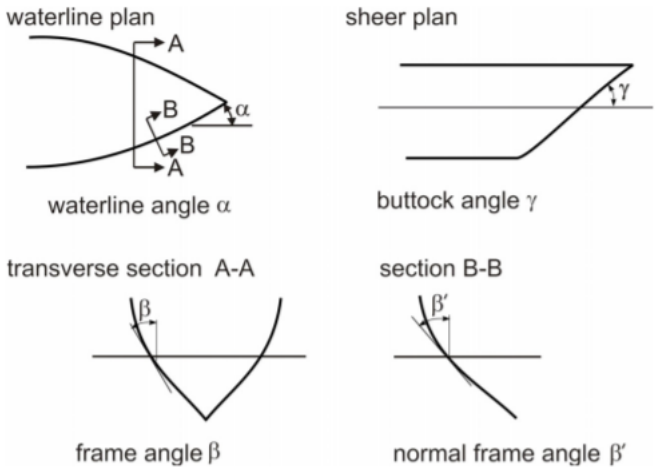


Figure 2.5: Definition of hull angles, from DNV (2016)

The global-to-local transformation matrix then becomes:

$$T_{lg} = \begin{bmatrix} \cos(\alpha) & -\sin(\alpha) & 0 \\ -\sin(\alpha)\sin(\beta') & -\cos(\alpha)\sin(\beta') & -\cos(\beta') \\ \sin(\alpha)\cos(\beta') & \cos(\alpha)\cos(\beta') & -\sin(\beta') \end{bmatrix} \tag{2.3.1}$$

where $\alpha$ is the waterline angle and $\beta'$ is the normal frame angle. In addition, a transformation matrix between the two global coordinate systems is used:

$$T_{ab} = \begin{bmatrix} \cos(\theta) & \sin(\theta) & 0 \\ -\sin(\theta) & -\cos(\alpha) & 0 \\ 0 & 0 & 1 \end{bmatrix} \tag{2.3.2}$$

where $\theta$ is the angle between the global coordinate systems.

Liu & Amdahl (2010) introduces two friction factors: The normal friction factor $\mu_n$ and the tangential friction factor $\mu_t$. These factors can be estimated by the impulse ratio:

$$\mu_n = sign(dp_1)\frac{\sqrt{dp_1^2 + dp_2^2}}{dp_3} \tag{2.3.3}$$

$$\mu_t = \frac{dp_2}{dp_1} \tag{2.3.4}$$

where $dp_1$, $dp_2$ and $dp_3$ are the incremental change in reaction impulse in $\vec{n}_1$-, $\vec{n}_2$- and $\vec{n}_3$-direction, respectively. The $sign()$ fuction returns the sign of the input value:

$$sign(x) = \begin{cases} 1 & \text{if} x > 0 \\ 0 & \text{if} x = 0 \\ -1 & \text{if} x < 0 \end{cases}$$

The normal friction factor is compared with a user-defined static friction coefficient $\mu_0$ to determine if a sticking or sliding mechanism applies. If $|\mu_n| \leq |\mu_0|$, the colliding bodies will stick together during impact, while if $|\mu_n| > |\mu_0|$, the bodies will slide against each other. The sticking-sliding mechanism is essential for solving the energy dissipation problem since it provides necessary boundary conditions. For a complete derivation of the dissipated energy it is referred to Liu & Amdahl (2010). The dissipated energy is given by:

$$E_i = \frac{1}{2} abs\left(\overline{m}_i \Delta v_i^2\right) \tag{2.3.5}$$

where $\overline{m}_i$ is the equivalent mass in $\vec{n}_i$-direction, $abs()$ returns the absolute value of the input, $\Delta v_i$ is the change in relative velocity in $\vec{n}_i$-direction and $i = 1,2,3$ in accordance with the local coordinate system (see figure 2.4). The equivalent masses are computed by equation (2.3.6), (2.3.7) and (2.3.8) which adds the corresponding mass components, scaled according to the force ratio. The force ratios are expressed by the friction factors $\mu_n$ and $\mu_t$.

$$\frac{1}{\overline{m}_1} = m_{11}^{-1} + m_{12}^{-1}\mu_t + m_{13}^{-1}\frac{\sqrt{1+\mu_t^2}}{\mu_n} \tag{2.3.6}$$

$$\frac{1}{\overline{m}_2} = m_{21}^{-1} + m_{22}^{-1}\mu_t + m_{23}^{-1}\frac{\sqrt{1+\mu_t^2}}{\mu_n\mu_t} \tag{2.3.7}$$

$$\frac{1}{\overline{m}_3} = m_{31}^{-1}\frac{\mu_n}{\sqrt{1+\mu_t^2}} + m_{32}^{-1}\frac{\mu_t\mu_n}{\sqrt{1+\mu_t^2}} + m_{33}^{-1} \tag{2.3.8}$$

Here, $m_{11}, m_{12}, m_{13} \ldots, m_{33}$ are elements in the mass matrix. Hydrodynamic effects are included in a simplified manner by constant added mass factors. By applying boundary conditions to equation (2.3.5), the dissipated energy in each direction can be formulated as fol-

lows.

**Sticking case**

When $|\mu_n| \leq |\mu_0|$, the equivalent mass $\overline{m}_i$ and the change in relative velocity $\Delta v_i$ are known in all directions. $\mu_n$ and $\mu_t$ are found from equation (2.3.3) and (2.3.4). The dissipated energy then becomes:

$$E_1 = \frac{1}{2} abs\left(-\overline{m}_1 \left(v_1^0\right)^2\right) \tag{2.3.9}$$

$$E_2 = \frac{1}{2} abs\left(-\overline{m}_2 \left(v_2^0\right)^2\right) \tag{2.3.10}$$

$$E_3 = \frac{1}{2} abs\left(\overline{m}_3 \left(e^2 - 1\right)\left(v_3^0\right)^2\right) \tag{2.3.11}$$

where $v_i^0$ is the initial relative velocity in $\vec{n}_i$-direction and $e$ is the coefficient of restitution. $e$ has a value between $0 \leq e \leq 1$, where $e = 0$ corresponds to an entirely plastic impact and $e = 1$ corresponds to a perfect elastic impact.

**Sliding case**

If sliding is the case, the normal friction factor is adjusted according to the static friction coefficient: $\mu_n = \mu_0$. However, a problem arises for the tangential friction factor $\mu_t$ since the incremental change in relative velocity in $\vec{n}_1$- and $\vec{n}_2$-direction are unknown. The solution is to assume a tentative sticking mechanism so that equation (2.3.4) can be used. The dissipated energy then becomes:

$$E_1 = \frac{1}{2} abs\left(\overline{m}_1 d v_1 \left(d v_1 + 2 v_1^0\right)\right) \tag{2.3.12}$$

$$E_2 = \frac{1}{2} abs\left(\overline{m}_2 d v_2 \left(d v_2 + 2 v_2^0\right)\right) \tag{2.3.13}$$

$$E_3 = \frac{1}{2} abs\left(\overline{m}_3 \left(e^2 - 1\right)\left(v_3^0\right)^2\right) \tag{2.3.14}$$

where $d v_1$ and $d v_2$ is the change in relative velocity in $\vec{n}_1$- and $\vec{n}_2$-direction, respectively.

### 2.3.2 Internal mechanics by non-linear finite element method

Internal mechanics deals with the distribution of dissipated strain energy between the colliding bodies and assessment of local structural response. Today, non-linear finite element analysis (NLFEA) is considered the most powerful tool for analysis of structural response in collisions (Yu 2017). The finite element method (FEM) enable simulations of physical events in a "virtual environment" on computer systems. Application of FEM in a structural problem is done by discretizing the geometry into a set of elements. A numerical procedure based on equilibrium, kinematic compatibility between strains and displacements, and strain-stress relationship (a material model) can then be applied to solve the problem (Moan 2003). Finite element theory is extensive and is not covered in full extent in this thesis. However, non-linear effects and explicit analysis, which are key elements in NLFEA of collisions, are described in the following.

Linear analysis assumes small displacements and linear-elastic material behaviour (Moan 2003), however these assumptions are not valid in most impact problems because of large plastic deformations. In finite element analysis (FEA) of impact problems, non-linearities are introduced in the form of:

- Geometrical non-linear behaviour (i.e. the change in geometry is accounted for)
- Boundary conditions (e.g. contact between objects)
- Non-linear material behaviour (e.g. plastic behaviour)

The following subsections describes these non-linear effects.

#### Geometric non-linearities

If the structural problem involves large displacements, the change in the geometry must be considered to improve accuracy. A common approach is to use a so-called corotational system where each element has a local coordinate system that follow the structure during deformation (Moan 2003). The loading is applied in a stepwise manner, hence it is convenient to express the static equilibrium equation on an incremental form:

$$\Delta \mathbf{R} = \mathbf{K}_I \Delta \mathbf{r} \tag{2.3.15}$$

Here, $\mathbf{R}$ is the external load vector, $\mathbf{K}_I$ is the incremental (tangent) stiffness, $\mathbf{r}$ is the nodal dispalcements and $\Delta$ denotes the increments. To account for the changing geometry, the local coordinate systems (on element level) are updated with respect to a fixed, global coordinate system. This is done by changing the transformation matrices, which tells the relation between local and global coordinates, at every time- and load-step.

### Contact conditions

Interactions between contacting surfaces can be included in the FEA by using a penalty-based approach on pre-defined master and slave segments (Hallquist 2006). At every time-step, algorithms are searching for penetrations of the master segment by slave nodes. If a nodal penetration is detected, a spring that acts between the slave node and the contact surface is inserted into the stiffness matrix. The contact spring-force is proportional to the penetration depth so that the penetration is resisted.

### Material model

Impact mechanics involve yielding, crushing, tearing and fracture of materials. To represent such non-linear phenomena, elastic-plastic material models and ductile failure criteria are implemented into the FEA. The basic principles that govern elastic-plastic material models are: yield criterion, hardening rule and flow rule (Hopperstad & Børvik 2017). In general, the yield criterion is formulated as:

$$f = \phi - \sigma_y = 0 \tag{2.3.16}$$

where $\phi$ is the yield function, which measures the magnitude of the stress state, and $\sigma_y$ is the yield stress, which is a material property. $f < 0$ gives elastic deformation, while yielding occurs when $\phi = \sigma_y$. Observations from experiments shows that metallic materials work-harden when exposed to plastic deformation (Hopperstad & Børvik 2017), i.e. the strength increases with plastic straining. Work-hardening can be included in the yield criterion as a function of the plastic strain:

$$f = \phi - (\sigma_0 + R) = 0 \tag{2.3.17}$$

Here, $\sigma_0$ is the initial yield stress and $R$ is the work-hardening rule which is a function of the plastic strain. One frequently used hardening rule is the power law:

$$R(\epsilon_p) = K\epsilon_p^n \tag{2.3.18}$$

where $K$ is the strength coefficient, $\epsilon_p$ is the plastic strain and $n$ is the strain hardening exponent. $K$ and $n$ are material properties. The strain-stress relation for an elastic-plastic material with work-hardening is shown in figure 2.6.

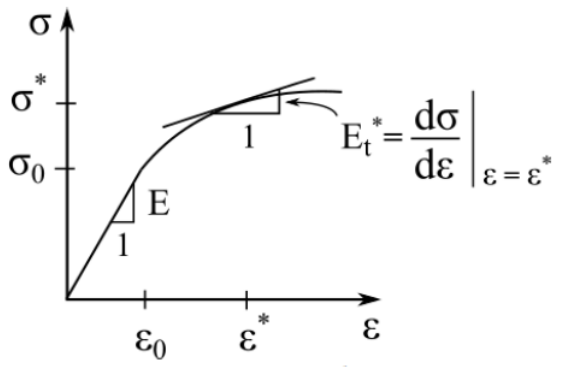


Figure 2.6: Elastic-plastic material with work-hardening, from Langseth et al. (2017)

A flow rule describes the relationship between stress increments $d\sigma$ and strain increments $d\epsilon$. For uniaxial stress, the flow rule is simply:

$$d\sigma = E_t d\epsilon \tag{2.3.19}$$

where $E_t$ is the tangential modulus as seen in figure 2.6.

**Ductile failure criteria**

Ductile fracture in metallic materials occurs because of microscopic voids, induced by local stress concentrations, that grows and possibly merges when the material is exposed to external loading (Anderson 2005). The void growth process is largely influenced by stress triaxiality (Hopperstad & Børvik 2017), i.e. stress components in all three directions, hence ductile fracture criteria depend on the stress state.

According to Storheim (2016), the Rice-Tracey Cockroft-Latham (RTCL) damage criterion, proposed by Törnqvist (2003), is well suited for stiffened panel structures like ships. RTCL uses stress triaxiality to characterize the damage by determining if shear or tension is dominating. The RTCL criterion is given by:

$$D = \frac{1}{\epsilon_{cr}} \int \dot{D} dt \tag{2.3.20}$$

where $D$ is the accumulated damage, $\epsilon_{cr}$ is the critical strain and $\dot{D}$ is the damage rate, which is dependent on the stress state $T$ (i.e. stress triaxiality). The damage rate is determined from:

$$\dot{D} = \begin{cases} 0 & \text{if } T < -1/3 \\ \frac{\sigma_1}{\sigma_{eq}}\dot{\epsilon}_{eq} & \text{if } -1/3 \leq T < 1/3 \\ exp\left(\frac{3T-1}{2}\right)\dot{\epsilon}_{eq} & \text{if } 1/3 \leq T \end{cases}$$

where, $\sigma_1$ is the normal stress, $\sigma_{eq}$ is the equivalent stress and $\dot{\epsilon}_{eq}$ is the equivalent strain rate.

In NLFEA, failed elements can be removed from the analysis to model fracture (Hopperstad & Børvik 2017). Elements are deleted when the accumulated damage inside an element reaches the critical value of the damage criterion ($D = 1$). This technique is called *element erosion*.

**Explicit analysis**

In general, there are two main types of FEA: *Implicit* and *explicit*. An implicit solver can be applied in both static and dynamic problems, while an explicit solver only can be applied for dynamic problems. In non-linear implicit analysis, iterations are necessary to establish equilibrium (LSTC and DYNAmore 2018*b*), and in addition, implicit analysis requires inversion of the stiffness matrix which increases the computational cost.

In explicit analysis, nodal accelerations can be computed directly because a diagonal lumped mass matrix $\mathbf{M}$ is used, hence inversion becomes trivial. The equation of motion can be derived in a semi-discrete form, i.e. discretized in space, by using the principle of virtual power (Hopperstad & Børvik 2017):

$$\mathbf{M}\mathbf{r} = \mathbf{R}^{ext} - \mathbf{R}^{int}(\mathbf{r}) \tag{2.3.21}$$

Here, $\mathbf{r}$ is the global nodal displacement vector, $\mathbf{R}^{ext}$ is the external load vector and $\mathbf{R}^{int}$ is the internal nodal force vector which is dependent on $\mathbf{r}$. A common method for solving equation (2.3.21) in time is to apply a finite difference method, e.g. the central difference method. The central difference time integration scheme is explicit because nodal accelerations, velocities and displacements from previous time steps are used to obtain the nodal velocities and dispalcements at the next time step (Moan 2003). In the central difference method, the nodal velocities $\dot{\mathbf{r}}$ and nodal displacements $\mathbf{r}$ are given by:

$$\dot{\mathbf{r}}_{n+\frac{1}{2}} = \dot{\mathbf{r}}_{n-\frac{1}{2}} + \frac{\Delta t_{n+1} + \Delta t_n}{2}\ddot{\mathbf{r}}_{\mathbf{n}} \tag{2.3.22}$$

$$\mathbf{r}_{n+1} = \mathbf{r}_n + \Delta t_{n+1}\dot{\mathbf{r}}_{n+\frac{1}{2}} \tag{2.3.23}$$

where $\Delta t_{n+1}$ is the time increment forward in time, $\Delta t_n$ is the time increment backwards in time, $\ddot{\mathbf{r}}$ is the nodal acceleration vector and $n-1$, $n$ and $n+1$ denotes points in time. This is illustrated in figure 2.7. The nodal accelerations are given by:

$$\ddot{\mathbf{r}}_n = \mathbf{M}^{-1}\left(\mathbf{R}_n^{ext} - \mathbf{R}^{int}(\mathbf{r}_n)\right) \tag{2.3.24}$$

at time-step $n$. The central difference scheme is only conditionally stable, hence very small time-steps are necessary in order to maintain stability. The maximum allowable time-step is given by:

$$\Delta t < min\left(\frac{h_e}{c}\right) \quad e \in [1, n_e] \tag{2.3.25}$$

where $h_e$ is the characteristic length of element $e$, $c$ is the current wave speed in the material given by equation (2.3.26) and $n_e$ is the total number of elements.

$$c = \sqrt{\frac{E}{\rho}} \tag{2.3.26}$$

In equation (2.3.26), $E$ is Young's modulus and $\rho$ is the material density. From equation (2.3.25) and (2.3.26), it can be seen that the time-step can be modified by fictitiously changing the material density. This is called *mass scaling*. However, mass scaling is only reasonable in structural problems where inertia effects are insignificant.

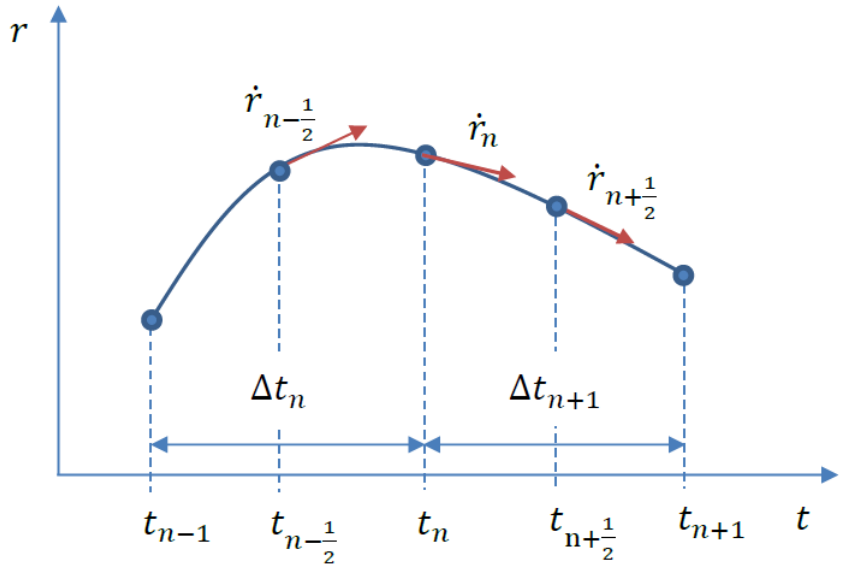


Figure 2.7: Illustration of the time discretization used in the central difference scheme, from Hopperstad & Børvik (2017)

## 2.4 Coupled analysis with hydrodynamic effects

Yu & Amdahl (2016) have developed a 6DOF coupled dynamic model for NLFEA of impact problems which includes surrounding water effects. Until today, sea water effects have been a major obstacle in most numerical codes (Yu 2017), especially codes that are designed for NLFEA. Fluid-structure interactions ought to be included in ship collisions in order to accurately represent the rigid body motions.

In the current coupled model, fluid effects for a ship are implemented into the numerical code LS-DYNA by using a traditional ship manoeuvring model proposed by Norrbin (1971). The manoeuvring model computes hydrodynamic loads in the horizontal plane, i.e. hydrodynamic loads for surge, sway and yaw motions. The equations of motion in the horizontal plane, using a body fixed coordinate system with the origin in the COG of the ship, are given by Newton's 2nd law (Yu 2017):

Surge:

$$m\left(\dot{u} - r\,u - x_{cog}r^2\right) = X_{hydro} + X_{dist} \tag{2.4.1}$$

Sway:

$$m\left(\dot{v} - r\,v - x_{cog}\dot{r}^2\right) = Y_{hydro} + Y_{dist} \tag{2.4.2}$$

Yaw:

$$I_{zz}\dot{r} + m x_{cog}\left(\dot{v} + r\,u\right) = N_{hydro} + N_{dist} \tag{2.4.3}$$

Here, $m$ is the mass and $u$, $v$ and $r$ are the velocities in surge, sway and yaw, respectively. $x_{cog}$ is the position coordinate of the COG in the longitudinal direction and $X_{hydro}$, $Y_{hydro}$ and $N_{hydro}$ are the hydrodynamic forces in calm water in surge, sway and yaw, respectively. Finally, $X_{dist}$, $Y_{dist}$ and $N_{dist}$ are the disturbance forces and moments due to wind, waves, current and collision. The ship manoeuvring model by Norrbin (1971) is used to determine the hydrodynamic forces $X_{hydro}$, $Y_{hydro}$ and $N_{hydro}$. The mathematical representation of the manoeuvring model is quite complex and for details regarding this model it is reffered to Norrbin (1971) and Yu et al. (2016). In summary, the hydrodynamic forces are given as functions of the instantaneous velocities ($u$,$v$ and $r$) and accelerations ($\dot{u}$,$\dot{v}$ and $\dot{r}$), the rudder angle $\delta$, the propeller revolution rate $n$, the sea water density $\rho$, the yaw angle $\psi$ and the engine output ratio $\mu$:

$$X_{hydro} = X\left(\psi, u, v, r, \dot{u}, \dot{v}, \dot{r}, \delta, n, \rho, \mu\right) \tag{2.4.4}$$

$$Y_{hydro} = Y\left(\psi, u, v, r, \dot{u}, \dot{v}, \dot{r}, \delta, n, \rho, \mu\right) \tag{2.4.5}$$

$$N_{hydro} = N\left(\psi, u, v, r, \dot{u}, \dot{v}, \dot{r}, \delta, n, \rho, \mu\right) \tag{2.4.6}$$

The manoeuvring model is a steady-state representation of the hydrodynamic forces acting on the ship, however, Yu et al. (2016) found that the model was suitable for collisions with a duration of more than 2 s.

Yu & Amdahl (2016) assumes that the out-of-plan motions, i.e. heave, roll and pitch, can be modelled as single DOF spring-damper subsystems so that there is no coupling with in-plane motions. Consequently, there is no coupling between heave, roll and pitch. Necessary added mass factors can be estimated by the empirical equations derived by Popov et al. (1969) (see appendix A). The restoring terms can be obtained if the natural periods are known; the natural periods can be computed in e.g. Sesam HydroD if a finite element (FE) model of the entire ship is available. Damping is computed empirically.

In LS-DYNA, the hydrodynamic forces from the manoeuvring model are applied to a node that represent the COG of the ship. The COG node is connected to a FE model, for example a bow model, through a set of rigid beams which constitutes the hull girder. A major advantage with this approach is the simple representation of the hull girder which limits the size of the FE model (the number of elements). Thus, only the colliding section of the ship needs detailed geometry.

# Chapter 3

# Impact Scenarios

This chapter addresses hazards in relation to cargo offloading. The emphasis is on shuttle tanker activity, but also supply vessel scenarios are mentioned. Other types of vessels, e.g. passing shipping vessels, are excluded since the probability of an impact scenario is negligible. Amdahl (2005) describes the frequency of occurrence and associated potential consequence for relevant striking vessels. A summary is given in table 3.1. As can be seen from the table, shuttle tankers and supply vessels constitute the greatest hazard for offshore structures.

Table 3.1: Potential striking vessels for offshore structures.

| Striking vessel | Frequency of occurrence | Potential consequence |
|---|---|---|
| Supply vessels | High | Low |
| Passing vessels | Low | High |
| Shuttle tankers | Medium | High |

## 3.1 Cargo offloading procedure

According to Sevan Marine ASA (2017), the cargo offloading procedure is typically executed as described in the following. The shuttle tanker approaches the FPSO with a heading towards a 50 m radial distance ”heading-offset circle” as can be seen in figure 3.1 (the inner circle). The velocity in the approaching phase is 0.5 knots (approximately 0.26 m/s). The tanker maintains a heading-offset throughout the offloading process to minimize the risk of drive-off collisions.

In the initial phase, the tanker manoeuvres towards a pick-up zone to receive a messenger line. The pick-up zone is located between the inner yellow sector and the 120 m radial dis-

tance marked in figure 3.1. At this stage, the distance between the tanker and the FPSO is at its smallest. A potential drive-off scenario is therefore affected by the limited acceleration field, hence the velocity at impact is limited. Cargo offloading starts after a offloading hose is connected and the tanker has moved back into the offloading sector (the green sector in figure 3.1). The probability of drive-off and drift-off accidents is highest during the offloading phase due to the lengthy duration (Vinnem et al. 2015). It can typically last around 20 hours or more.

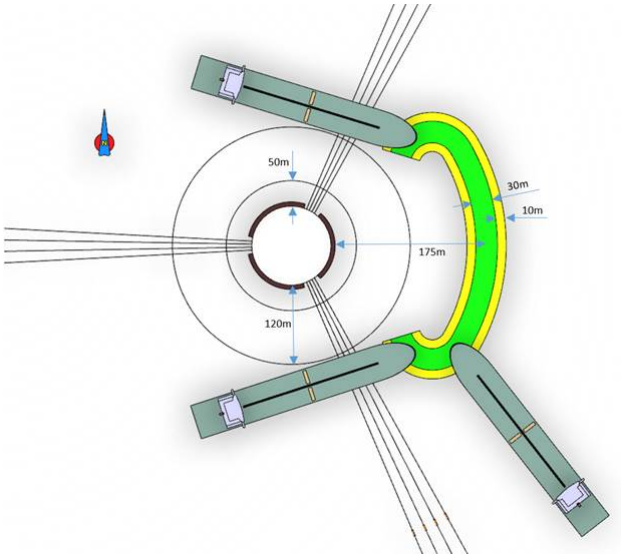


Figure 3.1: Shuttle tanker orientation during offloading, from Sevan Marine ASA (2017)

The heading of the shuttle tanker during offloading implies that head-on (front) collisions are the most likely scenario. In stationary weather conditions, a collision requires that the tanker turns towards the FPSO if drive-off or drift-off happens. The reason is that the heading-offset circle is designed so that a collision is avoided if the tanker should start moving forwards. However, in unstable weather conditions, the tanker will be exposed to weather vaning, thus the heading offset will continuously change. Variations of glancing collisions are therefore likely.

The cylindrical hull design of the Sevan 1000 results in no weather-vaning, hence the relative motions between the tanker and the FPSO will be of a different character compared to a ship-shaped FPSO. The tanker is always positioned in tandem configuration behind a ship-shaped FPSOs (with elements of surging and yawing) because of weather-vaning operations, see figure 3.2. This means that stern impacts are the most likely scenario. For the Sevan 1000 however, the tanker will move with a pendulum motion around the FPSO, with a heading according to the environmental loads. This leaves a large sector exposed for potential collisions. If the wind changes direction so that the tanker must perform a base point transition, i.e. the base point on the heading-offset circle is moved to the other side of the FPSO, a short period of central heading occurs.

Figure 3.2: Tandem offloading seen from the shuttle tanker, from Chen & Moan (2004)

## 3.2 Loading conditions

Contact between the FPSO and the shuttle tanker is dependent on individual loading condition. In the early offloading stage, the FPSO is fully loaded while the tanker is in ballast condition. First contact is then likely to be made between the tanker forecastle and the FPSO superstructure as shown in figure 3.3a. Crushing of the tanker forecastle is then expected, but also penetration of the FPSO hull may occur if the bulbous bow makes contact.

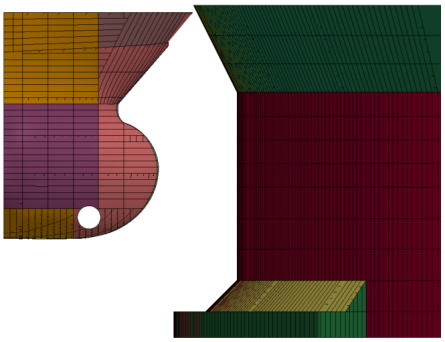

(a) **Scenario 1:** The Shuttle tanker is in ballast condition and the FPSO is fully loaded

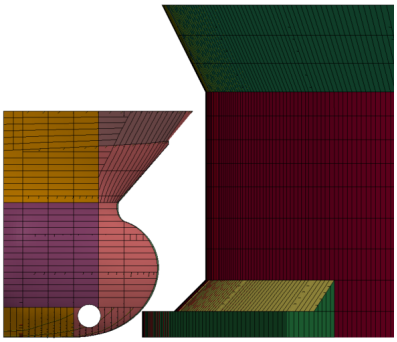

(b) **Scenario 2:** The shuttle tanker is fully loaded and the FPSO is in ballast condition fully loaded

Figure 3.3: Loading conditions and definition of scenario 1 and 2

When the shuttle tanker is fully loaded and the FPSO is in ballast condition, corresponding to the final offloading stage, contact is likely to be made between the bilge box and the bulbous bow as shown in figure 3.3b. It should be mentioned that the tanker draft in figure 3.3b is slightly increased to match the bilge box level and maximize bilge box damage. This modified draft is used in the analyses of scenario 2.

## 3.3 Upper limit drive-off velocity

The initial velocity of the striking ship is one of the key input values in a ship collision analysis. An upper limit drive-off velocity was estimated for the shuttle tanker based on a similar approach to the "dropped objects" model in DNV-RP-C204 (2010). It was assumed that in a drive-off scenario during offloading, the shuttle tanker will accelerate from a stagnant condition over a distance of 175 m (based on the distance in figure 3.1). The velocity profile of the tanker was derived from Newton's second law and a simple model with only drag resistance, see equation (3.3.1) and the illustration in figure 3.4.

$$(m+a)\frac{dV}{dt} = T - F_D \tag{3.3.1}$$

In equation (3.3.1), $m$ is the mass of the ship, $a$ is the added mass, $V$ is the velocity of the ship, $T$ is the thrust and $F_D$ is the drag force.

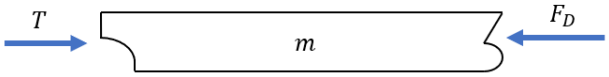


Figure 3.4: Simplified drive-off model

By using the initial condition $V = V_0 = 0$ and assuming constant thrust, the following solution to the differential equation (3.3.1) was obtained:

$$\left(\frac{V}{V_t}\right)^2 = 1 + exp\left(-\frac{S}{S_c}\right) \tag{3.3.2}$$

Here, $V_t$ is the terminal velocity, $S$ is the distance moved and $S_c$ is the characteristic distance which is given by:

$$S_c = \frac{m+a}{\rho_w C_D A_P} \tag{3.3.3}$$

Here, $\rho_w$ is the sea water density, $C_D$ is the drag coefficient and $A_P$ is the projected area of the ship. The drive-off velocity profile is shown in figure 3.5.

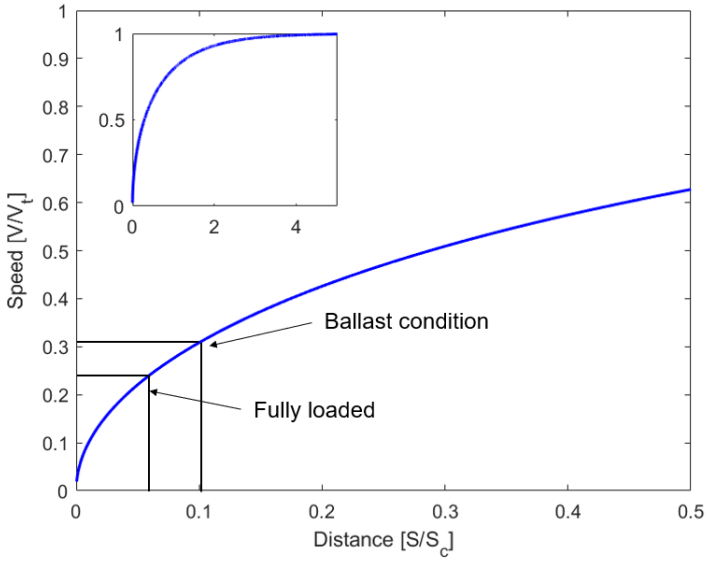


Figure 3.5: Velocity profile for shuttle tanker during drive-off

The drag coefficient was estimated using specifications for the shuttle tanker Jasmine Knutsen. Knutsen OAS Shipping (2018) states that the design speed (terminal velocity in equation (3.3.2)) is 7.7 m/s and the main enigine effect $P$ is 15.4 MW. It is assumed a loss of 20 %. By using equation 3.3.4, the thrust was estimated to 1.6 MN.

$$T = \frac{P\eta}{V_t} \tag{3.3.4}$$

In equation (3.3.4), $\eta$ is the overall efficency of the propulsion system. The drag coefficient was estimated to be 0.076 by using steady state considerations, i.e. $V = V_t$ and $T = F_D$, and equation (3.3.5).

$$C_D = \frac{F_D}{\frac{1}{2}\rho_w A_P V_t^2} \tag{3.3.5}$$

The shuttle tanker velocity at the instant of impact in ballast and fully loaded condition, corresponding to scenarios in the initial and final offloading phase, are given in table 3.2.

Table 3.2: Shuttle tanker speed at the instant of impact

| Scenario # | Loading condition | Characteristic distance $S_C$ [m] | Impact speed [m/s] |
|---|---|---|---|
| 1 | Ballast condition | 1649.9 | 2.4 |
| 2 | Fully loaded | 2749.8 | 1.9 |

## 3.4 Impacts with supply vessels

Tvedt (2014) presents a set of generic collision scenarios which covers all failures, with a significant probability, that may lead to a supply vessel – offshore installation collision. An overview of the scenarios is shown in figure 3.6. In summary, the initiating events for the scenarios are: Voyage with autopilot navigation using a ”way-point” (reference point for the route) set on the exact location of the installation, and manually or autopilot navigation of the vessel in close distance to the installation. Preventive actions, like radar surveillance systems and safety zones, are employed to reduce the probability of impacts (Moan et al. 2017), however such barrier functions may also fail. Last minute preventive actions are included in the model by Tvedt (2014) as ”emergency collision avoidance”.

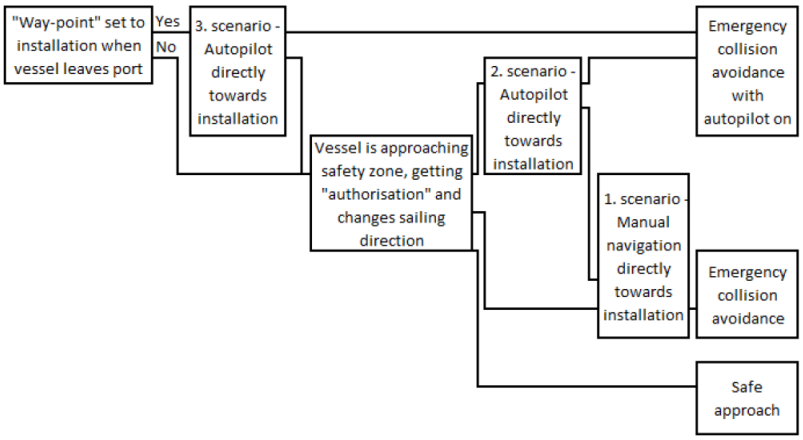


Figure 3.6: Overview of supply vessel - offshore installation collision scenarios, from Tvedt (2014)

Moan et al. (2017) describes a trend of increasing supply vessel size and innovative ship bow design, which together with modern DP systems results in an increase of impact velocity and kinetic energy. Two good examples of modern ship bow designs that are available on the marked today are the ULSTEIN X-BOW design, shown in figure 3.7, and the Vard design shown in figure 3.8. In the case of collisions with FPSOs, striking ships with sharp bow geometries are likely to induce local fracture in the FPSO hull since the contact force is highly concentrated. For this reason, an ULSTEIN X-BOW supply vessel is included in the FEA in this thesis, in addition to a more traditional supply vessel design, so that bow effects can be studied. Larger rounded geometries, like a shuttle tanker bow, are more likely to induce crushing of structural components because of the larger contact area. This type of deformation is associated with a larger energy dissipation (Børvik et al. 2017).


Figure 3.7: The supply vessel Esvagt Aurora, from Eni-Norway (2017)

Figure 3.8: The supply vessel Stril Barents, from Eni-Norway (2017)

## 3.5 An overview of the scenarios studied

Table 3.3 presents an overview of the scenarios that are studied by NLFEA in this thesis. External dynamic analyses are carried out for every scenario except for the X-BOW scenario because this vessel is assumed to be similar to the other supply vessel. The scenario numbering stated in the table will be used throughout this thesis (especially scenario 1 and 2).

Table 3.3: An overview of impact scenarios included in the NLFEA (ST = shuttle tanker, SV = supply vessel and X = included)

| Number | Scenario | Impact angle | | |
|---|---|---|---|---|
| | | Head-on | 30-degree | 60-degree |
| 1 | ST in ballast and FPSO in full load | X | X | X |
| 2 | ST in full load and FPSO in ballast | X | X | X |
| 3 | SV-FPSO impacts (coupled analysis) | - | X | X |
| 4 | X-BOX collision | X | - | - |

# Chapter 4

# Setup for External Dynamic Analysis

A MATLAB subroutine developed by Dr. Z. Liu was used for external dynamic analysis. This subroutine implements the method by Liu & Amdahl (2010) to estimate rigid body motions together with the total dissipated energy. A review of the theory involved was presented in section 2.3.1. A MATLAB script defining the geometry and hydrodynamic properties of the FPSO and the striking ships was created as an input to the analysis, see appendix D. Fully plastic impacts are assumed, i.e. the restitution factor is $e = 0$. The following section presents the key configurations of the external dynamic analysis.

## 4.1 Coordinate systems

Two body fixed coordinate systems was established in the COG of the striking ship and the FPSO as illustarted in figure 4.1. Both coordinate systems have the same oriantation with parallel longitudinal axes. The angle between the negative x-axis of the FPSO ($x_P$) and the radial line drawn from the COG of the FPSO to the contact point is defined as the "impact angle", $\phi$, in this paper. Thus, an impact angle of zero degrees corresponds to a central impact and at 90 degrees, the striking ship will drive right past the FPSO with no contact. $\alpha$ is the waterline angle as defined described in section 2.3.1.

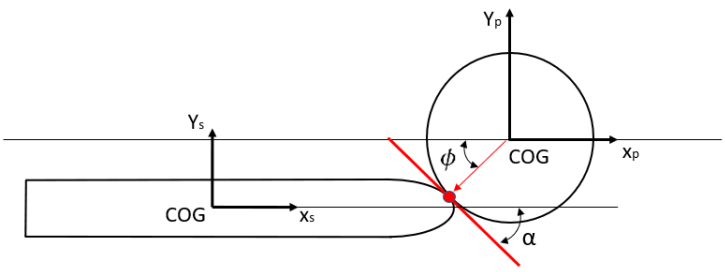


Figure 4.1: Body fixed coordinate systems used in the external dynamic analysis

A local coordinate system is established at the contact point and forms the contact plane (marked red in figure 4.1). According to Liu & Amdahl (n.d.), the stronger object should be used as the master object. In this analysis, it is assumed that the FPSO is the stronger object. In addition, the very large diameter hull of the Sevan 1000 FPSO naturally makes the FPSO the master object. The orientation of the contact plane normal $\vec{n}_3$ is dependent on draft variations as illustrated in figure 4.2.


(a) Scenario 1 (b) Scenario 2

Figure 4.2: Orientation of the contact plane in scenario 1 and 2

The contact plane is oriented with a normal frame angle of $\beta' = 26.6$ degrees as illustarted in figure 4.2a when the FPSO is fully loaded ($\beta' = -26.6$ in the MATLAB script). When the FPSO is in ballast condition, $\vec{n}_3$ is chosen to be perpendicular to the FPSO bilge box and also the main hull. The point of contact will also move in the horizontal plane (along the outer hull of both the striking ship and the FPSO) when the impact angle $\phi$ changes.

## 4.2 Hydrodynamic effects

Hydrodynamic effects are included in terms of constant added mass. Added mass factors and radius of gyration for the striking ships were estimated by empirical equations derived by Popov et al. (1969), see appendix A. The principal dimensions and the shape coefficients of the ship are the input parameters in these equations, thus shape coeffecient had to be assumed. Table 4.1 shows the selected shape coefficients. Principal dimensions are presented later in section 5.2 and 5.3 for the shuttle tanker and the supply vessel, respectively.

Table 4.1: Shape coefficients of the striking ships.

| Coefficient | | Shuttle tanker | Supply vessel |
|---|---|---|---|
| Waterplane coeff. | $C_{wp}$ | 0.9 | 0.8 |
| Mid-section coeff. | $C_m$ | 0.9 | 0.8 |
| Block coeff. | $C_b$ | 0.8 | 0.7 |

As a simplification, the added mass of the Sevan 1000 FPSO were assumed to be equal to the displaced mass. The same assumption was made by Amdahl (2005) for a similar buoy, the SSP300 FPSO. An overview of the added mass factors is given in table 4.2.

Table 4.2: Estimated added mass factors for the striking ships and the FPSO

| Component | Shuttle tanker | | FPSO | Supply Vessel |
|---|---|---|---|---|
| | Ballast | Full load | Ballast and full load | - |
| $\hat{m}_x$ | 0.0 | 0.0 | 1.0 | 0.0 |
| $\hat{m}_y$ | 0.40 | 0.83 | 1.0 | 0.66 |
| $\hat{m}_z$ | 1.76 | 0.86 | 1.0 | 1.03 |
| $\hat{j}_{xx}$ | 0.25 | 0.25 | 1.0 | 0.25 |
| $\hat{j}_{yy}$ | 1.96 | 0.96 | 1.0 | 0.98 |
| $\hat{j}_{zz}$ | 0.58 | 0.58 | 1.0 | 0.54 |

The radius of gyration in roll, pitch and yaw for the Sevan 1000 FPSO was estimeted by assuming the FPSO to be a cylinder with uniformly distributed mass. Equations of moments of inertia from Young & Freedman (2011) were then used. Table 4.3 shows the radius of gyration for the striking ships and the FPSO.

Table 4.3: Estimated radius of gyration for the striking ships and the FPSO

| Component [m] | Shuttle tanker | FPSO | Supply Vessel |
|---|---|---|---|
| $\hat{R}_{xx}$ | 15.93 | 26.22 | 7.14 |
| $\hat{R}_{yy}$ | 65.76 | 26.22 | 21.29 |
| $\hat{R}_{zz}$ | 65.50 | 32.88 | 22.50 |

## 4.3 The normal friction factor

The friction factor $\mu_0$ has a major influence on the energy dissipation in tangential direction to the contact surface. Liu & Amdahl (n.d.) suggests an effective friction factor that combines steel-to-steel plate friction and the resistance to transverse deformation:

$$\mu_0 = \mu_s + \mu_d \tag{4.3.1}$$

Here, $\mu_s$ is the steel-to-steel friction factor and $\mu_d$ is an equivalent friction factor that takes the indentation force caused by structural deformation into account. Liu & Amdahl (n.d.) suggests to estimate the tangential damage by a method that is similar to the grounding

process described by Alsos (2008) because sliding may generate a similar damage pattern to a grounding process. Figure 4.3 shows the grounding process (a) and a proposed model by Alsos (2008) for estimation of the indentation force (b).

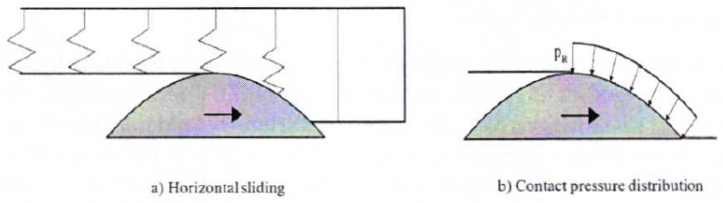


Figure 4.3: Illustration of structural deformation during a grounding process, fromAlsos (2008)

The friction factor $\mu_0$ used in this analysis was chosen based on the suggestions from Liu & Amdahl (n.d.) and discussions with the supervisors. Details are summarized in table 4.4.

Table 4.4: The normal friction factor.

| Component | Symbol | Value |
|---|---|---|
| Steel-to-steel plate friction | $\mu_s$ | 0.3 |
| Equivalent friction factor | $\mu_d$ | 0.3 |
| Effective friction factor | $\mu_0$ | 0.6 |

# Chapter 5

# Finite Element Models

## 5.1 Sevan 1000 FPSO model

The FE model of the Sevan 1000 FPSO is based on concept drawings provided by Sevan Marine ASA. A model of the complete geometry was created with the inclusion of a fully detailed sector for assessment of local structural response. Unfortunately, this model ended up being too large, hence only the fine mesh section of the double hull was used in the analysis. Some minor modifications were made to the radial bulkheads due to lack of information about plate thicknesses in the drawings, however, these modifications do not stand out because they adapt properties of neighbouring sections.

### 5.1.1 Structural arrangement

The Sevan FPSO design is characterized by the large diameter cylindrical hull which makes room for ballast, fuel and cargo storage tanks. A bilge box is added to the double bottom to improve motion characteristics by increasing the added mass. Ballast tanks are located inside the double hull, inside the bilge box and inside the double bottom. The cargo storage tanks are located in the inner sections as shown in figure 5.1. The main deck protrudes outside the main hull and creates a superstructure.

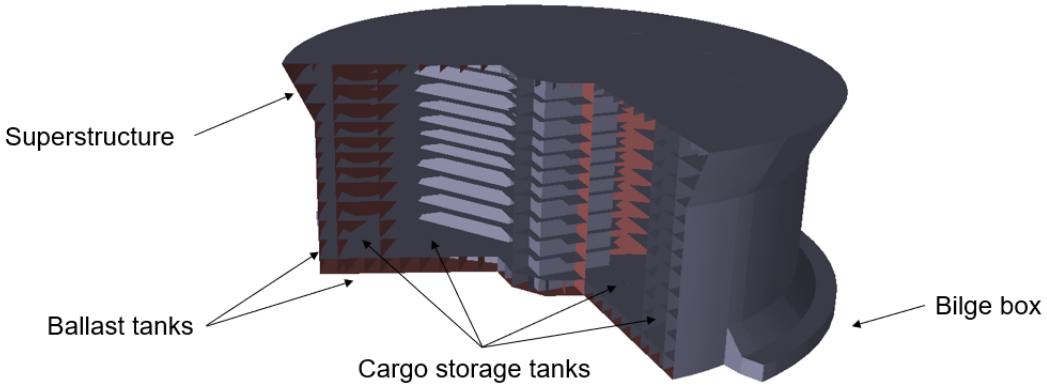


Figure 5.1: Internal view of the Sevan 1000 FPSO FE model in Sesam GeniE.

The principal dimensions of the Sevan 1000 FPSO are summarized in table 5.1.

Table 5.1: Principal dimensions of the Sevan 1000 FPSO

| Dimension | Condition | Value | Unit |
|---|---|---|---|
| Main deck diameter | | 104.0 | m |
| Main hull diameter | | 93.0 | m |
| Bilge box diameter | | 109.0 | m |
| Main deck height | | 42.0 | m |
| Draft | Fully loaded | 28.3 | m |
| Displacement | Fully loaded | 215 000 | tonnes |
| Draft | Ballast | 20.0 | m |
| Displacement | Ballast | 155 000 | tonnes |

Section properties varies with respect to the water depth. The largest stiffener profiles are in the bottom part of the structure, except for the outer plate stiffeners in the superstructure. Stiffener profiles are either T-profiles or flat bars. Table 5.2 presents an overview of the profiles used together with comments on typical locations. The main hull and the radial bulkheads are strengthened by vertical stiffeners and 10 decks with flat-bar stiffening (the horizontal frame).

Table 5.2: A simple overview of the stiffener profiles used in the FE model of the Sevan 1000 FPSO. The left column comments on typical locations, however, profiles may also occur at other locations.

| Profile dimensions [mm] | Typical location |
|---|---|
| T 500x15+150x19 | Outer plating of the superstructure |
| T 450x12+150x22 | Outer vertical plates in the bilge box |
| T 400x12+150x20 | Bottom part of the double hull and radial bulkheads |
| T 350x12+150x19 | mid-part of bulkheads in ballast tanks |
| T 300x12+15x16 | mid- and upper part of the double hull and bulkheads, and the main deck |
| T 200x11+15x14 | Vertical sections of upper main hull frame |
| FB 250x15 | Stiffening of horizontal frames |

Plate thicknesses are in the interval from 12 mm up to 23 mm as shown in figure 5.2.

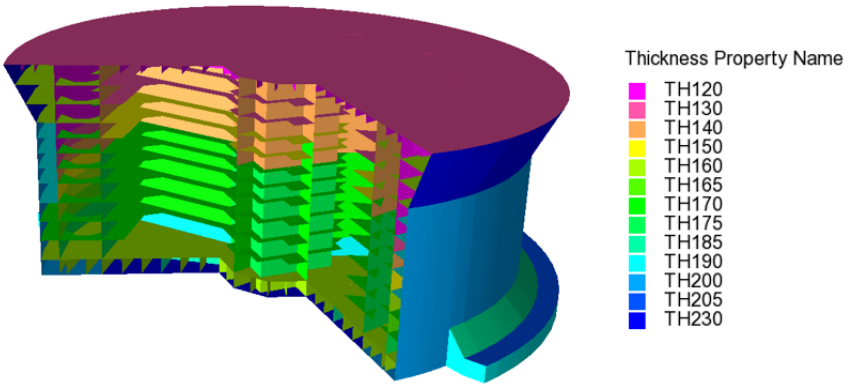


Figure 5.2: An overview of plate thicknesses. "Thickness Property Name" gives the thickness in mm.

It should be mentioned that a bulwark structure which extends the superstructure from the main deck is not included in the FE model. To create impact scenarios of interest, the shuttle tanker draft in ballast condition was therefore modified to match the main deck of the FPSO. Also, the topside is not considered apart from the accompanying mass.

### 5.1.2 The modelling process

The process of creating the Sevan 1000 FPSO FE model was quite complex and time consuming. Personal modelling experience was in many ways the reason, but also software limitations caused delays. Modelling and pre-processing were performed in two different

programs mainly because of personal preference, but also because of availability of software licences. An overview of the workflow is illustrated in figure 5.3.

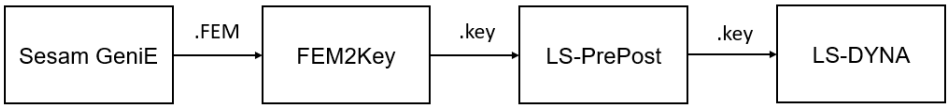


Figure 5.3: An overview of the modelling process of the Sevan 1000 FPSO. The square boxes represent computer programs, while the arrows in between shows the input and output file formats

The process started with creating the geometry in the FE software Sesam GeniE. Sesam GeniE was also used for generating mesh. After generating the mesh, the model was exported as a FEM-file and subsequently converted into a key-file using a Python program, "FEM2Key", designed for converting GeniE models to LS-DYNA. The key-file was imported into LS-PrePost for pre-processing. The NLFEA was carried out by the high-performance computer (HPC) "Vilje" at NTNU. Finally, LS-PrePost and MATLAB were used for post-processing of the results. The final version of the large Sevan 1000 FE model from Sesam GeniE is shown in figure 5.4.

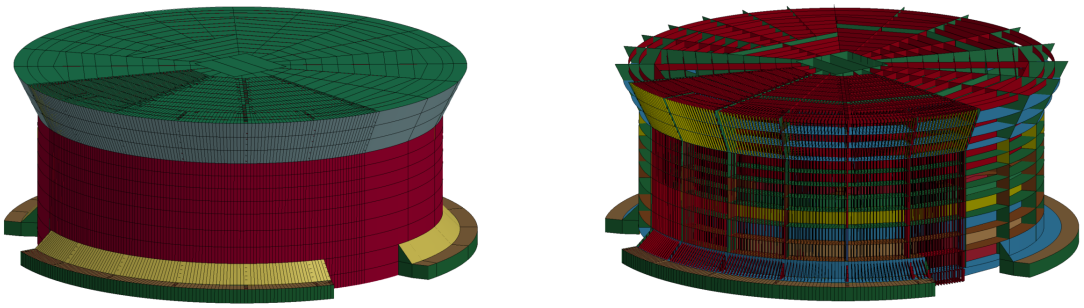

(a) Exterior view

(b) Interior view

Figure 5.4: The large FE model of the complete Sevan 1000 FPSO without mesh in LS-PrePost

### 5.1.3 Simplifications

As already mentioned, a model of the complete Sevan 1000 structure was created (seen in figure 5.4). Sections with various levels of structural detail was utilized and a fine mesh section was created to capture local structural deformations. However, this version of the model turned out to be too big and problems arose when running simulations on Vilje HPC. In addition, the mesh quality was hard to improve in the transition zones because of a conflict between the desire to reduce the number of elements and the complex geometry. The solution was to only use the fine mesh sector of the double hull as shown in figure 5.5.

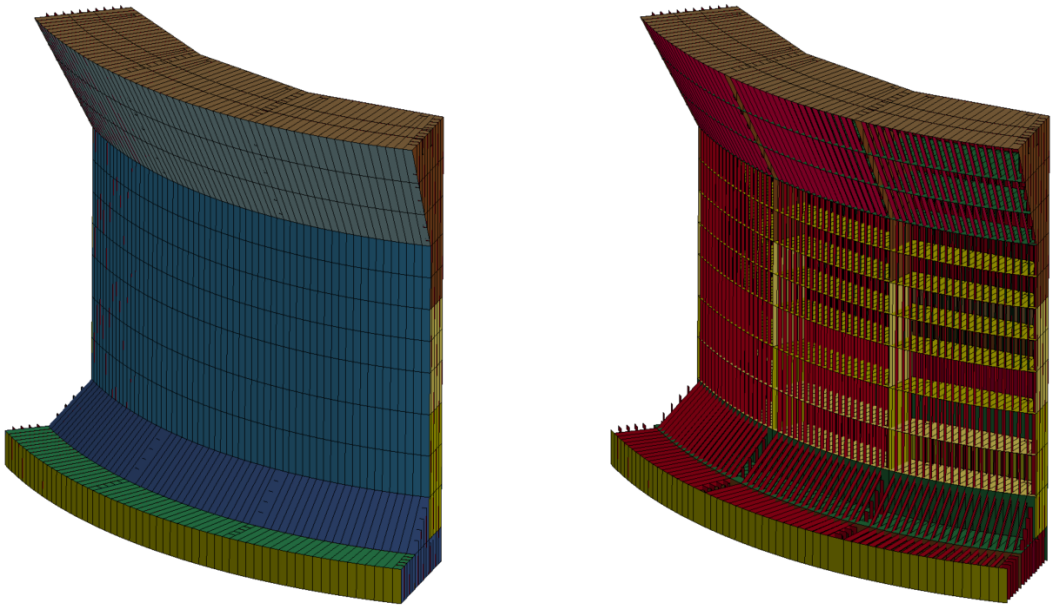

(a) Exterior view (b) Interior view

Figure 5.5: The small FE model of the Sevan 1000 double hull in LS-PrePost

### 5.1.4 Mesh

A mesh size of 140 mm was applied to all sections except the T-bar flange in Sesam GeniE (called mesh density in GeniE). This mesh size was selected based on a trial and error process. The goal of this process was to ensure good mesh quality for the stiffener web. A finer mesh than 140 mm resulted in a very high number of elements which was not desired because of increasing computational time. For the T-bar flange, a mesh size of 75 mm was applied in accordance with the width of the flange. Table 5.3 presents the number of elements in the current model.

Table 5.3: Number of elements in the Sevan 1000 FE model

| # Quad-elements | # Tri-elements | Total |
|---|---|---|
| 707352 | 2830 | 710182 |

In general, it is desired to minimize the ratio of triangular to quadrilateral elements (Storheim 2016). The ratio in the current model is approximately 0.4 %, which is satisfactory. Storheim (2016) recommends having a minimum of three elements per side in the model. This recommendation was fulfilled in the larger stiffener profiles with three (or more) elements over the stiffener web height. Smaller web heights have only two elements over the web height so that the total number of elements is kept at a minimum. The T-profile flange has one el-

ement over half the width, i.e. one element on each side of the web as can be seen in figure 5.6. Figure 5.6 shows an interior view of the mesh in the superstructure.

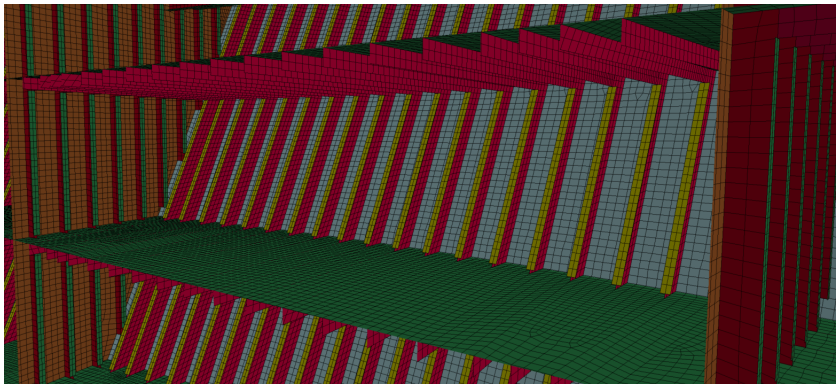

Figure 5.6: An interior view of the mesh inside the FPSO superstructure in LS-PrePost

The flanges of the T-profiles were disconnected from walls and decks, and only connected to the stiffener web. The free ends were modelled by cutting off a part of the flange, leaving a gap between the flange and the plate. The cut-offs can be seen in figure 5.7. Only nodes on the stiffener web were connect to walls and decks. By preventing connections between flanges and plates, the amount of ”partially split plates” was reduced and consequently the mesh quality improved. Boundary edges and internal connections could easily be controlled in Sesam GeniE by double-clicking on the desired plate and look for white lines indicating topology edges. The ”heal structure” feature could be used to remove undesired topology edges that affected the mesh quality.

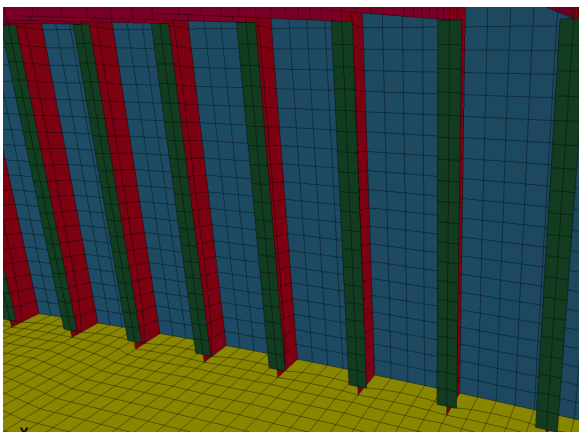

Figure 5.7: Modelling of T-profile stiffeners

### 5.1.5 Boundary conditions

The inner plate of the double hull was fixed at nodes that were located at the edge of bulkheads, decks or girders that are continuous in radial direction. These nodes are highlighted with blue colour in figure 5.8. It is assumed that these boundary conditions will simulate a reasonable structural behaviour when subjected to impacts because the radial bulkheads and the decks will act as supports for the inner plate of the double hull. A problem will arise if the striking ship penetrates both the outer and the inner plate, however, it is assumed that a very large amount of energy is required to achieve such a scenario. That amount of energy is not expected in this analysis.

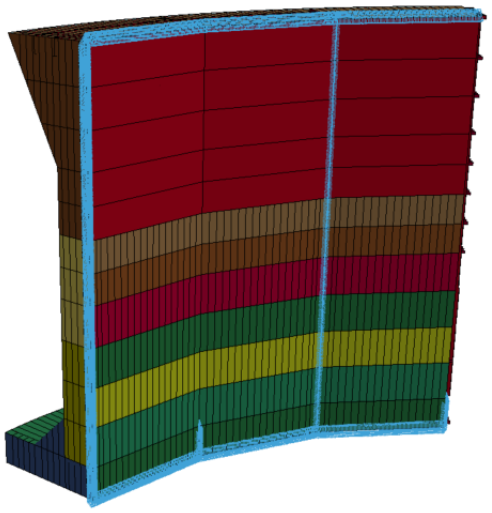

Figure 5.8: Boundary conditions on the Sevan 1000 FE model

### 5.1.6 Hydrodynamic properties

Hydridynamic properties were not included in FE model of the Sevan 1000 FPSO. This is because of the fixed boundary conditions that were applied to the model, i.e. the model cannot move. If the large version of the model was used, the one in figure 5.4, constant added mass could have been added to the model by scaling the total mass to study rigid body motions. However, with this approach the constant added mass would be the same in each direction.

### 5.1.7 Modelling challenges

The FE software Sesam GeniE was chosen based on the user friendly graphical user interface (GUI) and the powerful guiding geometry feature. Guiding geometry allows the user

to create complex geometry from a large selection of guiding points, curves and planes in the graphics window. However, problems arise when unintentional snap-points, generated by the program itself, interferes with the guiding geometry and results in misplacement of structural parts. This leads to inaccuracies in the model, e.g. undesirable ”short edges” and ”sliver faces” on the scale of millimetres as shown in figure 5.9. Short edges and sliver faces may result in poor mesh quality and very small elements. Such accuracy issues made the modelling process very time consuming and occasionally quite challenging.

A solution to the problem mentioned above was the ”model verification” feature in Sesam GeniE which identifies problems in the model. DNV-GL (2016) recommends to regularly verify the model and also enable ”interactive model checking” which gives pop-up warnings when a problem arises. Model problems were usually fixed by re-creating the affected sections. Sometimes, the heal structure feature could also solve the problem.

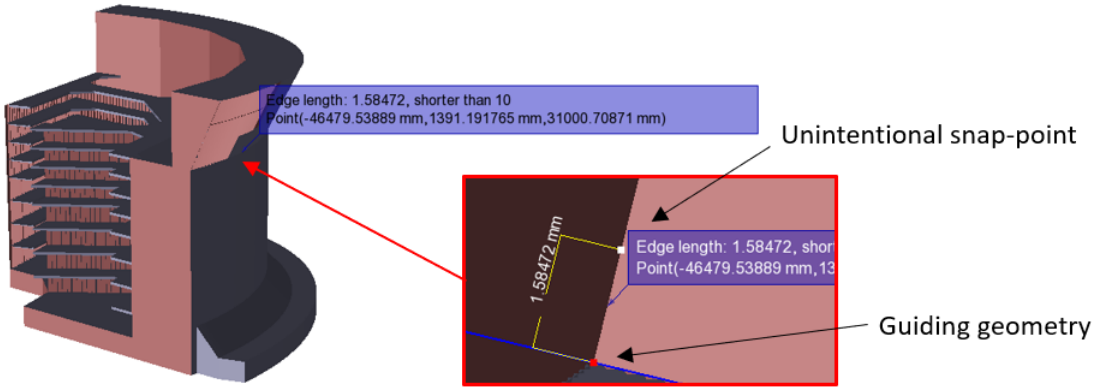


Figure 5.9: An example of a ”short edge” problem. The identified short edge is only 1.58 mm

The Sevan 1000 FE model was created in Sesam GeniE version 7.4, however this version had problems generating mesh for the final version of the FE model. The solution was to upgrade to the newest version of Sesam GeniE (version 7.8) which has an improved mesh generator. Due to the size of the model, it became particularly challenging to verify the mesh quality. Computer performance dramatically reduced when visualising the mesh results.

## 5.2 Shuttle tanker model

A pre-existing FE model of a Samsung shuttle tanker bow was used in the NLFEA. The bow model is similar to the 150,000 DWT shuttle tanker Jasmine Knutsen which is shown in figure 5.10. The principal dimensions are summarized in table 5.4. Hydrodynamic properties of the ship have been presented earlier in section 4.2.

Figure 5.10: Jasmine Knutsen, from Canship Ugland Ltd (2017)

Table 5.4: Principal dimensions of the shuttle tanker

| Dimension | Loading condition | Value | Unit |
|---|---|---|---|
| Length | | 262.0 | m |
| Width | | 46.0 | m |
| Height | | 28.6 | m |
| Draft | Fully loaded | 19.0 | m |
| Mass | Fully loaded | 150000 | tonnes |
| Draft | Ballast | 9.3 | m |
| Mass | Ballast | 90000 | tonnes |

Figure 5.11 shows the shuttle tanker bow FE model. The geometry of the bow contains a large blunt bulbous bow with horizontal stiffening and a forecastle with vertical stiffening. The outer hull stiffeners, the transverse bulkheads and the decks can be seen in figure 5.11b. All decks have longitudinal stiffening. The forecastle has a centred cut-out for the offloading hose inlet. Structural components related to the hose fairlead and traction winch is not included in the FE model.

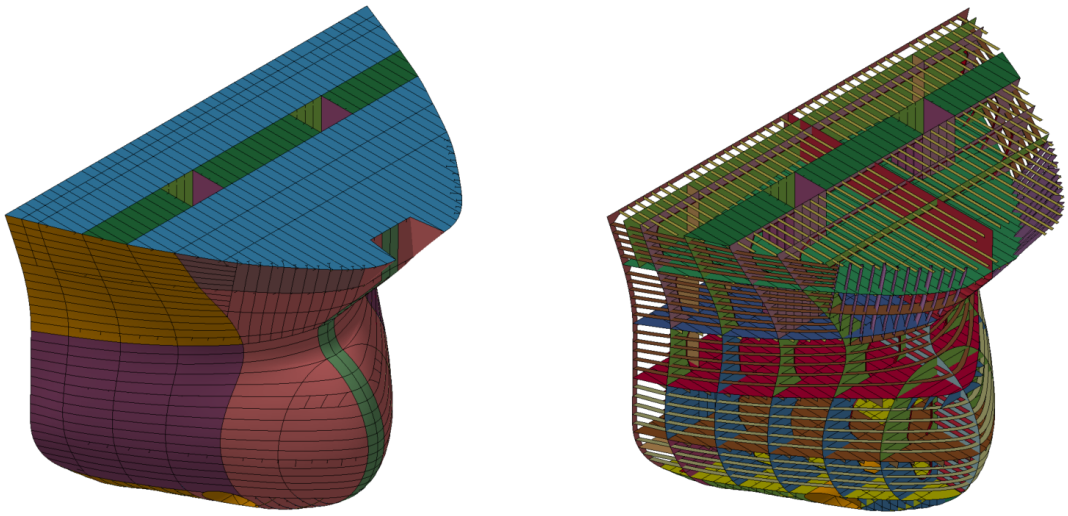

(a) Exterior view

(b) Interior view

Figure 5.11: The FE model of the shuttle tanker bow in LS-PrePost

The shuttle tanker bow model used a quadrilateral element mesh. The mesh is gradually refined towards the front of the bow. Table 5.4 presents details about the number of elements present in the model. As can be seen from the table, the ratio between quadrilateral and triangular elements was sufficient (0.32 %). The FE model includes a rigid back which was used for applying pre-described motion in the uncoupled analysis.

Table 5.5: Number of elements in the shuttle tanker bow FE model

| # Quad-elements | # Tri-elements | Total |
|---|---|---|
| 304597 | 964 | 305561 |

## 5.3 Supply vessel model

Like with the shuttle tanker model, a pre-existing FE model of a supply vessel was used in the NLFEA. The principal dimensions of the supply vessel are summarized in table 5.6.

Table 5.6: Principal dimensions of the supply vessel

| Dimension | Value | Unit |
|---|---|---|
| Length | 90.0 | m |
| Width | 18.8 | m |
| Height | 15.5 | m |
| Draft | 6.2 | m |
| Mass | 7500 | tonnes |

Plate thicknesses varies from 7 mm to 12.5 mm, with the largest thicknesses in the bulbous bow section. T-profiles are used for deck girders and flat-bar stiffeners are used for stiffening of decks and hull plating. Stiffener spacing is approximately 600 mm. Details regarding the structural arrangement can be seen in figure 5.12a and 5.12b.

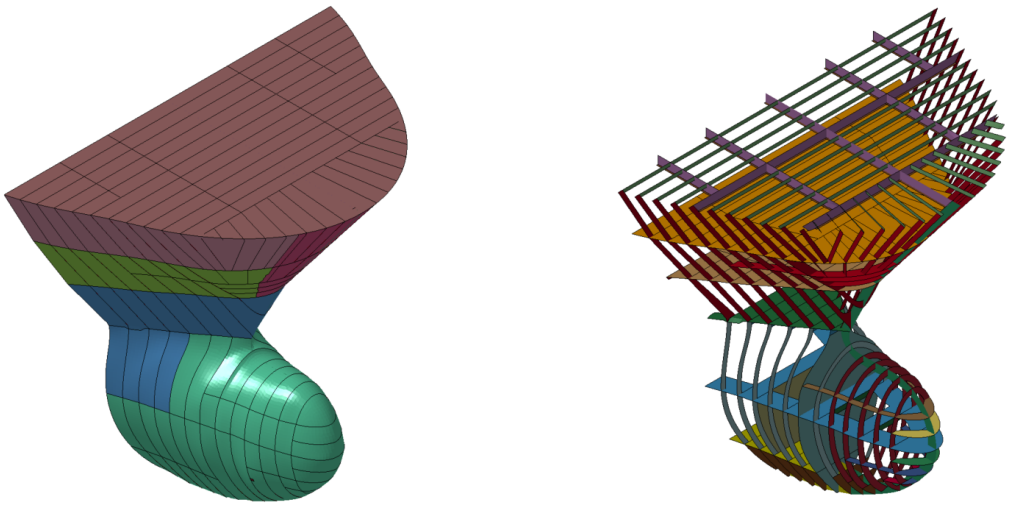

(a) Exterior view

(b) Interior view

Figure 5.12: The FE model of a supply vessel bow in LS-PrePost

The model size and mesh quality are summarized in table 5.7.

Table 5.7: Number of elements in the FE model of the supply vessel bow

| # Quad-elements | # Tri-elements | # Beam elements | Total |
|---|---|---|---|
| 70322 | 189 | 5 | 70511 (+5) |

The supply vessel model is compatible with coupled analysis. The model was modified by Post Doc. Zhaolong Yu during his work on hydrodynamic aspects of ship collisions (see Yu

et al. (2016), Yu & Amdahl (2016) and Yu (2017)). The FE model includes the hull girder, represented by a set of rigid beam elements, with the ship's COG at the rear end as seen in figure 5.13. An inertia part is located at the COG. It is used for applying mass and inertia properties to the ship model. The mass applied to the inertia part is calibrated with respect to the bow section so that the total mass is correct. At the COG, a horizontal cross of rigid beams is used for applying the hydrodynamic loads. Only minor modification had to be made to the coupled model when importing the Sevan 1000 FE model: Update material model, modify contact properties, positioning of the Sevan 1000 model and application of boundary conditions.

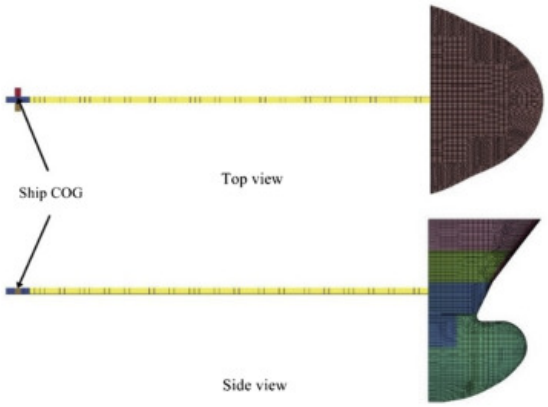


Figure 5.13: FE model of supply vessel with rigid hull girder, from Yu & Amdahl (2016)

## 5.4 ULSTEIN PX105 X-BOW model

In addition to the "traditional" supply vessel bow model presented above, a model of the ULSTEIN PX105 supply vessel X-BOW, created by Pettersen (2008), was used. This model was included in the NLFEA to study the effect of a different bow geometry with ice-strengthening. Figure 5.14a and 5.14b shows the structural arrangement of the vessel. For more details about the X-BOW model it is referred to Pettersen (2008). Table 5.8 summarizes the mesh quality and the size of the model.

Table 5.8: Number of elements in the FE model of the X-BOW supply vessel

| # Quad-elements | # Tri-elements | Total |
|---|---|---|
| 327911 | 16735 | 344646 |

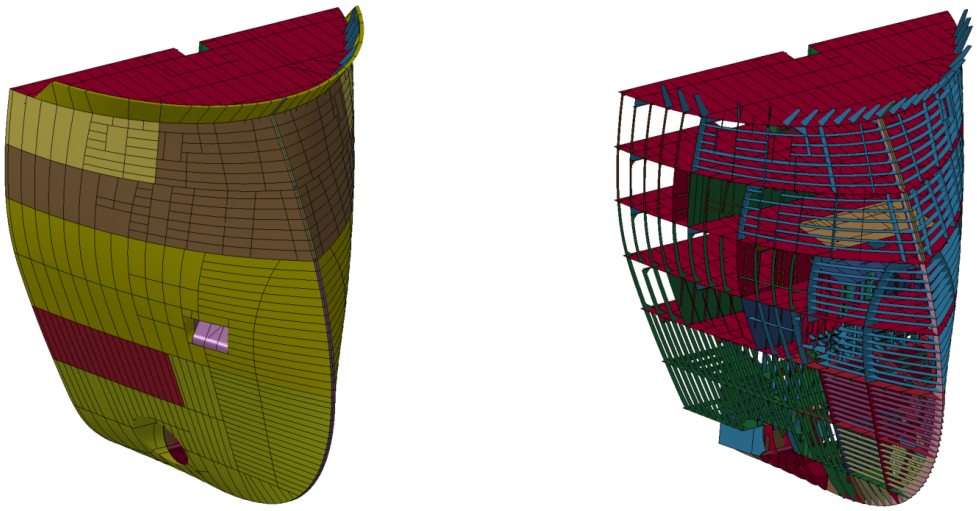

(a) Exterior view

(b) Interior view

Figure 5.14: The FE model of the ULSTEIN X-BOW bow in LS-PrePost

# Chapter 6

# Setup for Finite Element Analysis in LS-DYNA

## 6.1 Material models

A user defined material model was applied to all deformable parts in both the striking ship and the FPSO (material model 41-50 in LS-DYNA). This particular material model has been used a similar work by Ma (2014). The material is an elastic-plastic material with power law hardening rule. The RTCL damage criterion, which was described in section 2.3.2, is applied.

Similar mild steel properties were applied to both the striking ship and the FPSO. For this reason, the estimated strength of the striking ship and the FPSO is conservative ($\sigma_0$ and $K$ in table 6.1 are believed to be larger for the FPSO). A rigid material (material model 20 in LS-DYNA) was applied for rigid parts. In the uncoupled analysis with prescribed motion, displacement and rotation constraints were added to the rigid material so that only rigid body motion in surge was allowed for the striking ship (CMO=+1 in the MAT keyword). Table 6.1 presents the properties of the two materials. Here, $\rho$ is the density, $\sigma_0$ is the initial yield stress, $E$ is Young's modulus, $\upsilon$ is Poisson's ratio, $n$ is the power law exponent, $K$ is the strength coefficient and $\epsilon_{cr}$ is the critical strain. $\epsilon_{cr} = 0.71$ was assumed reasonable, although it might be somewhat high. The material is therefore quite ductile.

Table 6.1: Material properties

| | $\rho$ $[kg/m^3]$ | $\sigma_0$ $[MPa]$ | $E$ $[GPa]$ | $\upsilon$ [-] | $n$ [-] | $K$ $[MPa]$ | $\epsilon_{cr}$ [-] |
|---|---|---|---|---|---|---|---|
| User defined material | 7830 | 235 | 207 | 0.3 | 0.24 | 670 | 0.71 |
| Rigid material | 7830 | - | 207 | 0.3 | - | - | - |

## 6.2 Element properties

"Belytschko-Tsay" shell elements were applied to all FE models in LS-PrePost (ELFORM=2 in the ELEMENT_SHELL keyword). The element consists of 4 nodes with 5 DOFs: translation in local x-, y- and z-direction, and rotation about local x- and y-axis as illustrated in figure 6.1a. The Belytschko-Tsay shell element is the default shell element in LS-DYNA and it is the preferred choice for explicit analyses because of its computational efficiency (Hallquist 2006). One-point Gauss integration (reduced integration) is standard for efficiency reasons (ICOMP=0 for Gauss Quadrature rule) (Haufe et al. 2013). 5 through-shell-thickness integration points was selected; see figure 6.1b for illustration of the through-shell-thickness integration points.

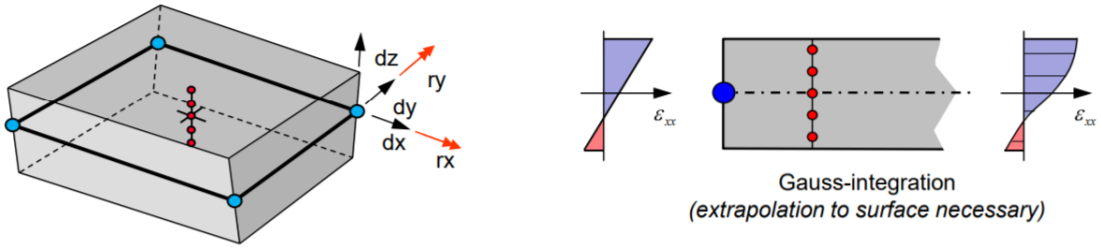


(a) Reduced integration shell

(b) Through-shell-thickness integration points

Figure 6.1: Belytschko-Tsay shell element, from Haufe et al. (2013)

Since reduced integration is used, so-called hourglass modes can occur in the elements. These are modes of deformation that results in zero strain and stress inside the element (Hallquist 2006). Hourglass modes can be limited by adding stiffness to the shell elements using the CONTROL_HOURGLASS keyword. Hourglass control type 4 was used in this thesis. The hourglass energy, i.e. the energy related to the added stiffness, can be included in the total energy output in LS-DYNA by setting HGEN=2 in the CONTROL_ENERGY keyword.

## 6.3 Element erosion

Erosion of failed elements was enabled in the NLFEA (IFAIL=1 in the MAT keyword). The RTCL damage criterion was used. As described in section 2.3.2, element erosion is an efficient way of modelling fracture. An element is deleted from the analysis if the accumulated damage $D$ inside the element is equal (or close) to the critical value determined by the critical strain $\epsilon_{cr}$. Figure 6.2 shows an example of element erosion from the NLFEA.

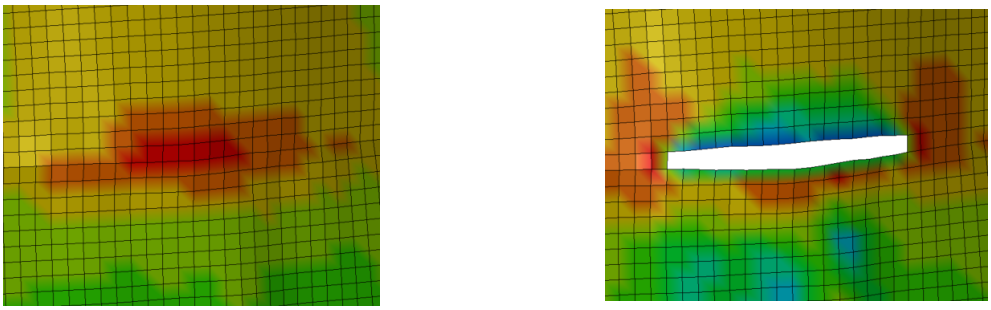

(a) Before fracture

(b) After fracture

Figure 6.2: Occurence of element erosion in the NLFEA

## 6.4 Selevtive mass scaling

As described in section 2.3.2, the smallest element size determines the time-step. The length of the time-step is designed so that an elastic stress wave cannot propagate across an element undetected. Good mesh quality and a reasonable element size are therefore essential. In this master thesis project, limited time was spent on mesh refinement and quality checks. Mass scaling was therefore applied as a quick fix for areas with poor mesh quality and very small elements.

The time-step limit parameter DT2MS in the keyword file was set to $-2.5 \cdot 10^{-6}$ seconds (found under CONTROL_TIMESTEP in the keyword input). It should be mentioned that the benefits of using a negative value was unfortunately discovered quite late in the work process, thus only some of the analyses uses the negative DT2MS value. According to LSTC and DYNAmore (2018*c*), a positive DT2MS value adds or takes away mass so that the time-step is always equal to the DT2MS value, while a negative value only adds mass to elements that require a time-step lower than |DT2MS|. Storheim (2016) does not recommend using selective mass scaling for ship collisions because the energy balance might be affected. However, the ratio between the physical mass and the nonphysical scaled mass in the NLFEA was only around 0.02, thus the effect on the energy balance is assumed to be insignificant.

## 6.5 Contact

Contact between the striking ship and the FPSO were defined using the automatic contact feature AUTOMATIC_SURFACE_TO_SURFACE. Every element that is included in the contact definition has a contact surface normally projected out from the element mid-plane (LSTC and DYNAmore 2018*a*). The normal distance is given by half the shell thickness (the default contact thickness value). At the edges of the element, the contact surface wraps around with

a radius equal to the specified thickness. A master-slave relation was established and the FPSO was selected as the master segment.

Internal contact, i.e. contact between sections belonging to the same structure, were defined using the AUTOMATIC_SINGELE_SURFACE feature. A static friction coefficient of 0.3, corresponding to the steel-to-steel friction, was applied for all contact definitions. No dynamic friction was applied. Initial penetrations was allowed (IGNORE=1 in the CONTROL_CONTACT keyword).

## 6.6 Prescribed motion

Internal mechanics of ship collisions does not concern rigid body motions as described in section 2.3. For this reason, a prescribed surge motion with constant velocity 5 m/s was applied to the striking ships in LS-DYNA. The striking ship velocity is independent of the initial conditions defined in the external, thus a larger velocity can be applied so that the computational time is reduced. Structural damage related to the scenarios defined in the external dynamic analysis can be found by comparing the internal energy in the NLFEA to the required energy dissipation from the external analysis. The time-step where the internal energy matches the required energy dissipation, gives the resulting structural damage. In this thesis, it is assumed that all of the dissipated energy is taken as strain energy, thus the structural damage is somewhat overestimated.

## 6.7 User-defined loading

The coupled hydrodynamic model by Yu & Amdahl (2016) utilizes a user-defined load subroutine in LS-DYNA, called LOADUD, to implement the ship manoeuvring model. The LOADUD subroutine allows users to create custom loading from the input variables which are nodal displacements, velocities and accelerations. In the case of the current coupled model, nodal displacements and velocities at the COG of the ship are used for computing the hydrodynamic loads at each time-step. As of today, the hydrodynamic solver is not generalized, thus implementation of a new ship model requires recalibration of the subroutine. This makes the coupled model quite challenging to use.

It should be mentioned that nodal accelerations for rigid bodies are not provided in the LOADUD subroutine, hence the nodal acceleration must be estimated by the velocity history (Yu 2017). A consequence of the acceleration problem is possible numerical instabilities. However, no issues related to this was encountered in this thesis. For further details about

the estimation of the nodal accelerations and the user-defined subroutine in LS-DYNA, it is referred to Yu (2017), Yu et al. (2016) and Yu & Amdahl (2016).

# Chapter 7

# Decoupled Analysis of Impacts from a Shuttle Tanker and Supply Vessels

## 7.1 Energy dissipation

As a start, the dissipation of energy is studied for central and glancing impacts by external mechanics. Both 3DOF (in the horizontal plane) and 6DOF analysis are carried out for shuttle tanker and supply vessel impacts, but the emphasis is on 6DOF analysis. An in-depth study of 30- and 60-degree impacts is given in the final subsection. Key input data has been described in chapter 4.

### 7.1.1 Shuttle tanker impacts

Table 7.1 presents the maximum dissipated energy obtained from 3DOF and 6DOF analysis of shuttle tanker impacts. Recall that scenario 1 contains the shuttle tanker in ballast condition (initial offloading phase), while scenario 2 contains the shuttle tanker in fully loaded condition (final offloading phase). The FPSO has the opposite loading condition of the tanker in agreement with the current offloading stage. The upper limit initial velocity of the shuttle tanker depends on the loading condition: 2.4 m/s in scenario 1 and 1.9 m/s in scenario 2. The initial kinetic energy is 259.2 MJ in scenario 1 and 270.8 MJ in scenario 2. Fully plastic behaviour is assumed, i.e. $e = 0$, and an effective friction coefficient of $\mu_0 = 0.6$ is used.

Central impacts resulted in the largest energy dissipation as expected. For planar impacts, approximately 82.7% and 67.4% of the initial kinetic energy are dissipated in scenario 1 and 2, respectively. For multi-planar impacts, the dissipation of energy is somewhat lower: 78.7% in scenario 1 and 54.1% in scenario 2. The reduction is due to 3D motions; the COG of the

striking ship and the FPSO is not at the same vertical level as the contact point, hence out-of-plane motions will occur in addition to the in-plane motions (figure 4.2 in chapter 4 shows the position of the contact point).

Table 7.1: Maximum dissipated energy in shuttle tanker - FPSO impacts

| # DOFs | Impact scenario | Max. dissipated energy [MJ] |
|---|---|---|
| 3 | 1 | 214.3 |
| | 2 | 182.4 |
| 6 | 1 | 203.9 |
| | 2 | 146.5 |

Figure 7.1 shows the development of energy dissipation for all glancing impact angles. It is apparent that central and small angle impacts are the worst-case scenarios. This is expected. However, an interesting observation is that impacts involving the shuttle tanker in ballast condition (scenario 1) results in the largest dissipated energy. This is because of the greater difference in mass between the colliding bodies in scenario 1, hence it requires more energy to accelerate the FPSO in scenario 1 than in scenario 2.

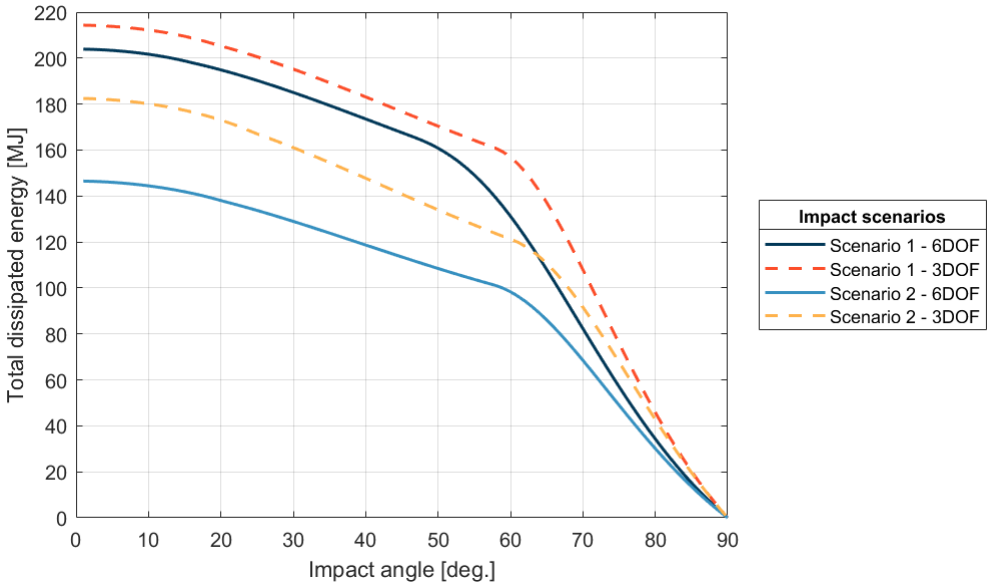


Figure 7.1: Energy dissipation in non-central shuttle tanker - FPSO impacts

It is observed that the gradients in figure 7.1 changes noticeably in the interval [50, 70] degrees because of a change from a sticking to a sliding mechanism. Sticking is when the colliding objects hook together and experience shared residual motions. Sticking or sliding is determined by comparing the absolute value of the impulse ratio $\mu_n$ (the estimated normal

friction coefficient) and the static friction coefficient $\mu_0$ as described in section 2.3.1. Figure 7.2 shows the development of the impulse ratio.

Figure 7.3 compares the same planar impact with $\mu_0 = 0.3$ and $\mu_0 = 0.6$. As can be seen from the figure, $\mu_0$ has a great influence on the duration of the sticking mechanism with respect to impact angle. The effect of using a larger $\mu_0$ is an increase of dissipated energy for sliding impacts because of the extended stick phase. This effect is reasonable due to the inclusion of transverse structural deformation in the larger effective friction coefficient $\mu_0 = 0.6$.

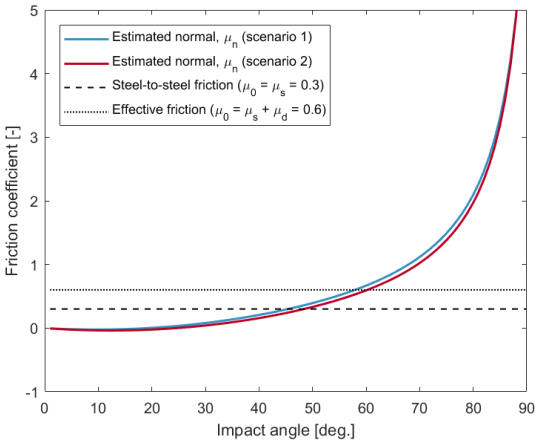


Figure 7.2: The development of the impulse ratio $\mu_n$ in planar analysis of shuttle tanker - FPSO impacts

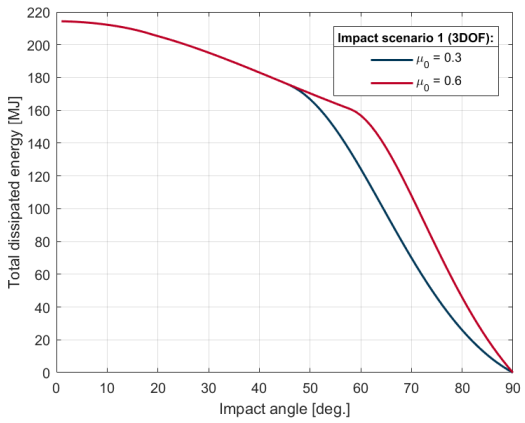


Figure 7.3: The effect of the static friction coefficient $\mu_0$ on energy dissipaton in planar analysis of shuttle tanker - FPSO impacts

### 7.1.2 Supply vessel impacts

Table 7.2 presents the maximum dissipated energy obtained from the analysis of head-on impacts from a supply vessel. It was observed that the variation of FPSO loading condition had a minor effect on the dissipated energy, thus only fully loaded FPSO was used throughout the analysis. Both 3DOF and 6DOF analyses were carried out. Two initial velocities were considered: 2 m/s and 4 m/s. Fully plastic behaviour was assumed and an effective friction coefficient of $\mu_0 = 0.6$ was used.

Table 7.2: Maximum dissipated energy in supply vessel - FPSO impacts

| # DOFs | Initial velocity [m/s] | Max. dissipated energy [MJ] |
|---|---|---|
| 3 | 2 | 14.7 |
| | 4 | 59.0 |
| 6 | 2 | 14.5 |
| | 4 | 57.8 |

The maximum energy dissipation occurs for central impacts as expected. It is observed that planar analysis estimates the largest amount of dissipated energy, however the difference is not that distinct as for shuttle tanker impacts. This can be seen in figure 7.4 which shows the development of dissipated energy for increasing impact angles. In the 6DOF analysis, 96.7% of the initial kinetic energy is dissipated in the central impact.

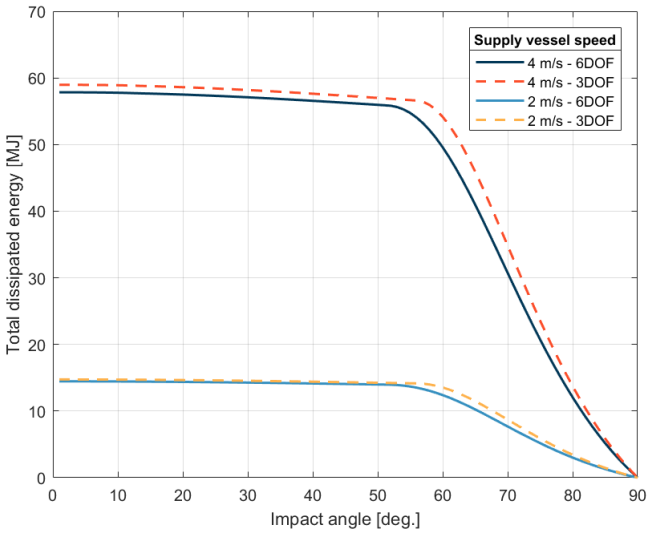


Figure 7.4: Total amount of dissipated energy for supply vessel-FPSO collisions

The dissipation of energy follows the same pattern of sticking and sliding as discussed for shuttle tanker impacts. An interesting observation is the approximately constant energy level when the sticking mechanism applies. The reason is that the FPSO behaves almost like a fixed body because of the much larger mass and the result is no significant residual motions (see the next section 7.2 on global rigid body motions). The amount of dissipated energy is thus approximately constant during sticking. A reduction of dissipated energy is not prominent until sliding occurs, which is between 50 and 60 degrees.

### 7.1.3 30- and 60-degree glancing impacts

Two non-central impacts are studied in more detail in the following. 30 and 60 degrees impact angles were chosen to represent one instances of sticking and sliding, respectively. Table 7.3 presents the total dissipated energy $E_{total}$, the dissipated energy in normal direction to the contact surface $E_n$, the dissipated energy in tangential direction to the contact surface $E_t$ and the impulse ratio $\mu_n$ obtained from the analyses. 6DOF analysis was employed.

Table 7.3: Dissipated energy for 30- and 60-degree impacts with the shuttle tanker

| Impact scenario | Angle [deg.] | $E_{total}$ [MJ] | $E_n$ [MJ] | $E_t$ [MJ] | $\mu_n$ [-] |
|---|---|---|---|---|---|
| 1 | 30 | 183.33 | 142.70 | 40.63 | 0.52 |
| | 60 | 133.73 | 61.90 | 71.83 | 0.92 |
| 2 | 30 | 131.72 | 129.30 | 2.42 | 0.13 |
| | 60 | 104.00 | 60.05 | 43.95 | 0.70 |

It is observed that size of the impact angle and the orientation of the contact surface affects normal-tangential ratio of the dissipated energy. In scenario 1, i.e. when the shuttle tanker forecastle impacts the FPSO superstructure, the dissipated energy in tangential direction constitutes approximately 22% of the total dissipated energy in the 30-degree impact and approximately 54% in the 60-degree impact. In scenario 2 on the other hand, only 1.8% and 42% of the energy is dissipated in tangential direction in the 30- and 60-degree impact, respectively (see also the impulse ratio). This is because the contact surface was selected to be perfectly vertical in scenario 2, while in scenario 1, the contact surface was angled according to the FPSO superstructure ($\beta'$ = 26.6 degrees as indicated in figure 4.2 in chapter 4).

It can be argued that the orientation of the contact surface in scenario 2 is somewhat unrealistic. However, at this point it is unknown if ductile design, strength design or shared-energy design applies for the contact between the FPSO bilge box and the bulbous bow of the shuttle tanker. A shared-energy deformation process will give a contact surface orientation based on a combination of the bulbous bow curvature and the bilge box geometry. The problem in this case is that such geometric dependency is difficult to implement into the external dynamic analysis and may introduce uncertainties. Therefore, it is assumed that the FPSO is the strongest body and determines the orientation of the contact surface.

Table 7.4 presents the energy dissipation for 30- and 60-degree impacts from a supply vessel. Fully loaded FPSO was used in this analysis, hence contact is established between the supply vessel forecastle and the FPSO superstructure. The bulbous bow was neglected like in scenario 1 for shuttle tanker impacts. The FPSO was believed to be the strongest body, hence the normal frame angle was selected in agreement with the slope of the FPSO superstructure ($\beta'$ = 26.6 degrees).

A similar behaviour to shuttle tanker impacts is observed. The dissipation of energy in normal direction dominates for 30-degree impacts, while the distribution of energy in normal and tangential direction is similar for 60-degree impacts. By increasing the initial velocity, the total dissipated energy increases by a factor equal to the ratio of the change in initial velocity raised to the power of two (this is expected). The impulse ratio is not affected by the

change in initial velocity.

Table 7.4: Dissipated energy for 30- and 60-degree impacts with the supply vessel

| Initial velocity | Impact angle [deg.] | $E_{total}$ [MJ] | $E_n$ [MJ] | $E_t$ [MJ] | $\mu_n$ [-] |
|---|---|---|---|---|---|
| 2 m/s | 30 | 14.26 | 11.87 | 2.39 | 0.36 |
| | 60 | 12.41 | 5.82 | 6.60 | 0.80 |
| 4 m/s | 30 | 57.05 | 47.48 | 9.57 | 0.36 |
| | 60 | 49.65 | 23.27 | 26.39 | 0.80 |

## 7.2 Global rigid body motions

Global rigid body motions obtained from the external dynamic analysis are presented in the following. Effects from hydrodynamic drag and anchor lines are not considered, hence the response may be somewhat overestimated.

As expected, it is observed that the sticking mechanism highly affects the residual motions. The set of impact angles that results in sticking depends on the applied friction coefficient $\mu_0$ as described at the end of section 7.1.1. The set of angles that results in sticking is large since $\mu_0 = 0.6$ was used in the analysis. The effect of sticking is evident in figure 7.5 which shows the residual speeds (the absolute value of the residual velocity) for glancing impacts with the shuttle tanker (7.5a) and the supply vessel (7.5b).

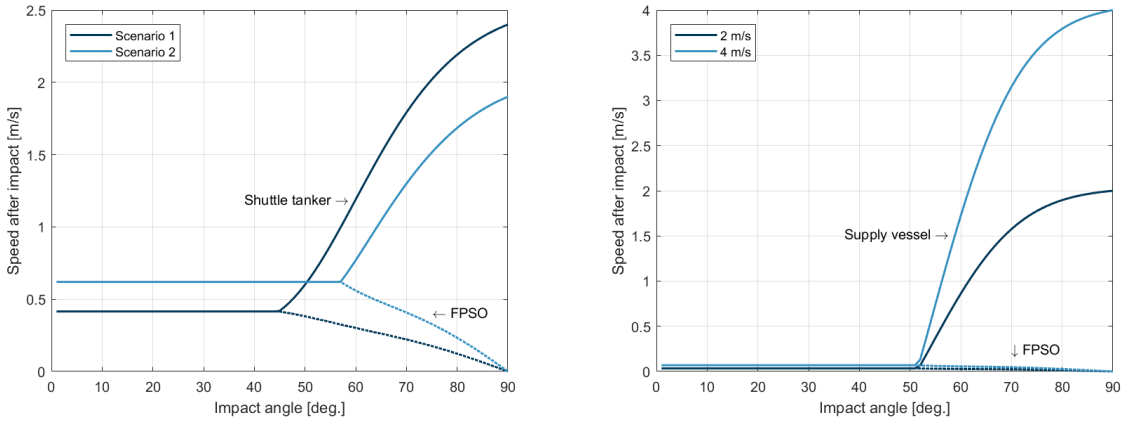


(a) Shuttle tanker impacts

(b) Supply vessel impacts

Figure 7.5: Residual speed of the FPSO and the striking ship

It is observed that supply vessel impacts do not generate any significant motions in the FPSO. This is because of the very large difference in mass. Shuttle tanker impacts on the other

hand results in larger FPSO motions because of the more even mass ratio. Scenario 2, which corresponds to the final offloading phase, will therefore generate the largest residual motions in the FPSO. The mass ratio is ≈ 1 in this scenario.

Table 7.5 presents the velocity components for 30- and 60-degree impacts with the shuttle tanker. The velocity components are obtained at the contact point and are converted into global coordinates. The translational velocities are the only outputs due to the 3x3 formulation of the model (translational and rotational DOFs are combined). The vertical component $V_z$ will thus generate roll and pitch motions, the transverse component $V_y$ will generate roll and yaw motions, and the longitudinal component $V_x$ will generate pitch and yaw motions. The level of influence is determined by comparing the component's normal distance from the COG to the contact point with the radius of gyration. It is assumed that sway and heave motions in the shuttle tanker are insignificant, hence pitch and yaw motions will dominate. This is because of the longitudinal distance of the contact point which is approximately twice the length of the estimated radius of gyration in pitch and yaw (see $\hat{R}_{yy}$ and $\hat{R}_{zz}$ in table 4.3 in chapter 4). The transverse position of the contact point is only slightly larger than the radius of gyration in roll, hence roll motions are assumed to be less prominent. The same applies for the vertical distance to the contact point.

It should be mentioned that the vertical geometry of the shuttle tanker bow was not considered. The current tanker geometry is thus a vertical extrusion of the planar geometry shown in figure 4.1 in chapter 4. The same applies for the supply vessel.

Table 7.5: Residual velocities for 30- and 60-degree impacts with the shuttle tanker

| | | Residual velocity [m/s] | | | | | |
|---|---|---|---|---|---|---|---|
| | | Shuttle tanker | | | FPSO | | |
| Impact scenario | Impact angle [deg.] | $V_x$ | $V_y$ | $V_z$ | $V_x$ | $V_y$ | $V_z$ |
| 1 | 30 | 0.415 | 0.0 | 0.0 | 0.415 | 0.0 | 0.0 |
| | 60 | 1.112 | -0.449 | -0.235 | 0.269 | 0.132 | 0.136 |
| 2 | 30 | 0.620 | 0.0 | 0.0 | 0.620 | 0.0 | 0.0 |
| | 60 | 0.762 | -0.112 | 0.004 | 0.551 | 0.099 | -0.003 |

It is observed that 30-degree impacts from the shuttle tanker results in a shared surge motion due to sticking. This is the case in both scenario 1 and 2. For 60-degree impacts, transvers and vertical velocity components ($V_y$ and $V_z$) are introduced due to sliding. In scenario 1, the geometry of the FPSO superstructure results in the shuttle tanker bow being pushed down and away from the FPSO. This can be derived from the negative $V_y$ and $V_z$ that generates significant yaw and pitch motions. It is believed that the FPSO experience significant sway motion due to the cylindrical hull and the smaller radius of gyration in yaw, i.e. surge and

sway will dominate instead of yaw motion. In addition, $V_z$ is smaller for the FPSO, hence only minor roll and pitch motions are present.

In scenario 2, the vertical position of the contact point results in a change in sign of the transverse and the vertical components. The pitch and roll motions are therefore reversed compared to scenario 1. The orientation of the contact surface in this scenario results in a much smaller vertical component of the contact force, hence $V_z$ is small and in-plane motions will dominate in both bodies (i.e. surge, sway and yaw motions). The yaw motion in the shuttle tanker is less prominent compared to scenario 1. This may be because of the lower initial velocity and the larger surge motion of the FPSO.

Table 7.6 presents the velocity components obtained from analysis of 30- and 60-degree impacts with the supply vessel. It is observed that the residual motions of the FPSO are insignificant when subjected to impacts from the supply vessel.

Table 7.6: Residual velocities for 30- and 60-degree impacts with the supply vessel

| | | Residual velocity [m/s] | | | | | |
|---|---|---|---|---|---|---|---|
| | | Supply Vessel | | | FPSO | | |
| Initial velocity | Impact angle [deg.] | $V_x$ | $V_y$ | $V_z$ | $V_x$ | $V_y$ | $V_z$ |
| 2 m/s | 30 | 0.034 | 0.0 | 0.0 | 0.034 | 0.0 | 0.0 |
| | 60 | 0.673 | -0.482 | -0.210 | 0.023 | 0.014 | 0.007 |
| 4 m/s | 30 | 0.069 | 0.0 | 0.0 | 0.069 | 0.0 | 0.0 |
| | 60 | 1.345 | -0.964 | -0.419 | 0.046 | 0.028 | 0.015 |

A similar response to the shuttle tanker is observed for the supply vessel in 60-degree impacts. This is because both vessels have a similar ratio between the perpendicular distance between the COG and the contact point, and the radius of gyration in roll, pitch and yaw. It is therefore assumed that $V_y$ will generate significant yaw motion and $V_z$ will generate moderate roll motion in the supply vessel.

## 7.3 Local structural response

The following subsections presents the internal mechanics of the collision scenarios studied in the external dynamic analysis in the previous sections (section 7.1 and 7.2). Internal mechanics were studied by NLFEA in LS-DYNA. The structural response is in accordance with a prescribed motion of the striking ship; the ship velocity is constant and the heading does not change. For this reason, the final time-step in the NLFEA does not necessarily corre-

spond with the end result of the external dynamic analysis. Still, the complete duration of the NLFEA is presented because the extended part may be of interest.

### 7.3.1 Shuttle tanker impacts

#### Central impacts

Figure 7.6 shows the development of internal energy for head-on central impacts with the shuttle tanker. The internal energy consists of elastic strain energy and work done in plastic deformation. Scenario 1 is shown in figure 7.6a and scenario 2 in figure 7.6b. The vertical dashed lines marks the cut-off point where the total internal energy corresponds to the total dissipated energy from the external dynamic analysis. It is assumed that all of the dissipated energy from the external dynamic analysis is absorbed as strain energy.

At the energy cut-off point, it is found that the ratio of internal energy between the shuttle tanker and the FPSO is approximately 2.0124 in scenario 1 and 1.0014 in scenario 2. This means that the shuttle tanker absorbs 66.8% of the total dissipated energy in scenario 1, while in scenario 2, the amount of absorbed energy is equal.

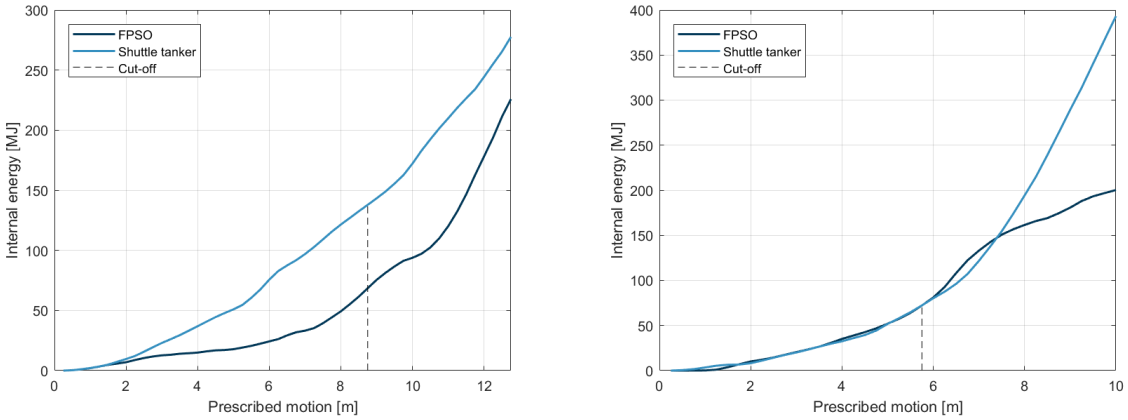


(a) Scenario 1

(b) Scenario 2

Figure 7.6: Development of internal energy in head-on central impacts from the shuttle tanker

In scenario 1, it is observed that the FPSO superstructure is crushing the shuttle tanker forecastle. A progressive buckling process occurs in the upper decks of the forecastle. The folding is most prominent in the top deck and can be seen in figure 7.7. A similar behaviour is also observed in the second upper deck at a later time-step, however the folding is not that distinct. This folding mechanism constitutes approximately half of the energy dissipated by the shuttle tanker.

A bending process of the outer hull shells, including stiffeners, constitutes the rest of the energy dissipated by the shuttle tanker. Plastic bending occurs at the side and bottom boundaries of the contact area between the FPSO and the shuttle tanker. The top boundary is involved in the progressive buckling process. The damage in the shuttle tanker after a central impact in scenario 1 (initial offloading phase) can be seen in figure 7.8a. The colour contours are according to the von Mises stress, however, the legend is excluded from the figures since the stress levels are not emphasized. Still, the colouring indicates which sections that are affected by the deformation process.

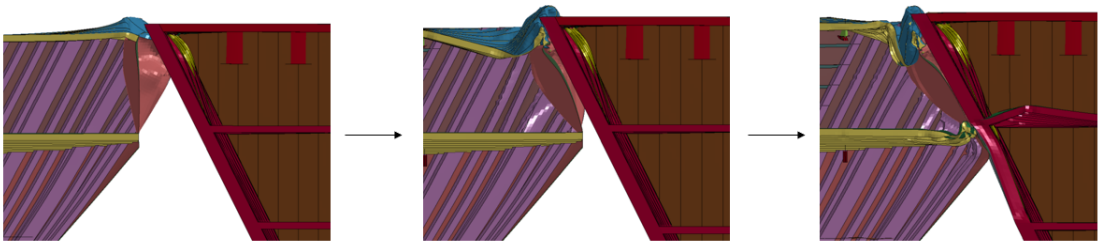

Figure 7.7: Plastic folding of the shuttle tanker top deck

The shuttle tanker forecastle slowly imprints the FPSO superstructure. Eventually, the second upper deck in the FPSO starts buckling, as can be seen at the final time-step in figure 7.7 and in figure 7.9. The current deck is located at approximately the same height as the second upper deck in the shuttle tanker. Both decks buckle as the crushing process continues. Plastic bending occurs in the FPSO hull at the boundary of the contact area. However, the FPSO superstructure is much stronger than the shuttle tanker forecastle, thus the depth of the imprint is limited. The FPSO hull is fully intact when the internal energy matches the external dynamic analysis. The damage in the FPSO can be seen in figure 7.8b. The bulbous bow has not yet made contact as seen in figure 7.9.

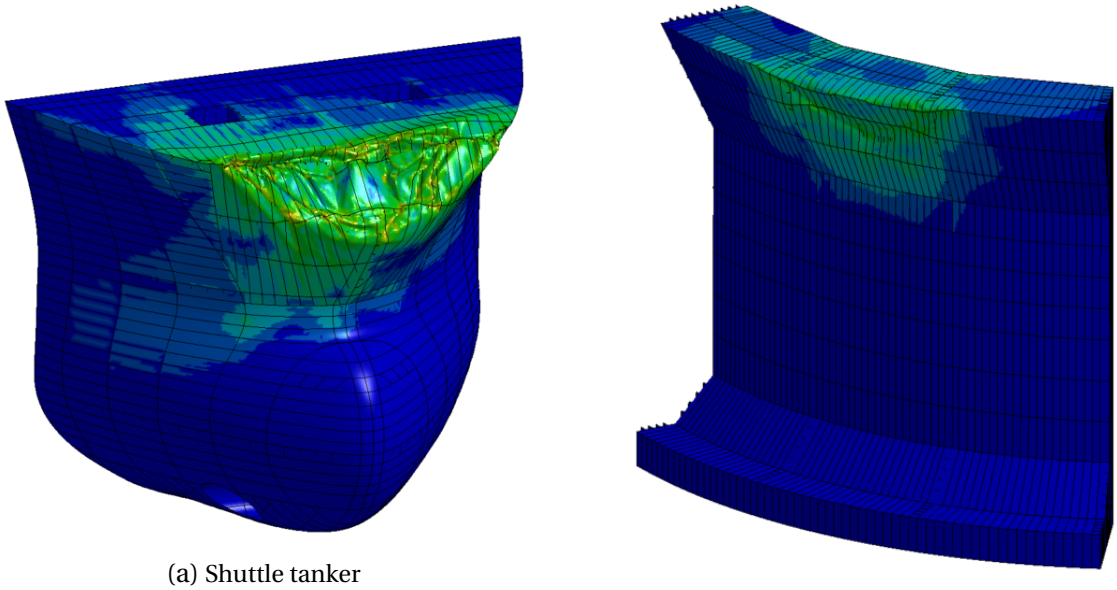

(a) Shuttle tanker

(b) FPSO

Figure 7.8: Damage in the shuttle tanker and the FPSO in scenario 1

Figure 7.9 shows a longitudinal cross-section view at the same time-step as in figure 7.8.

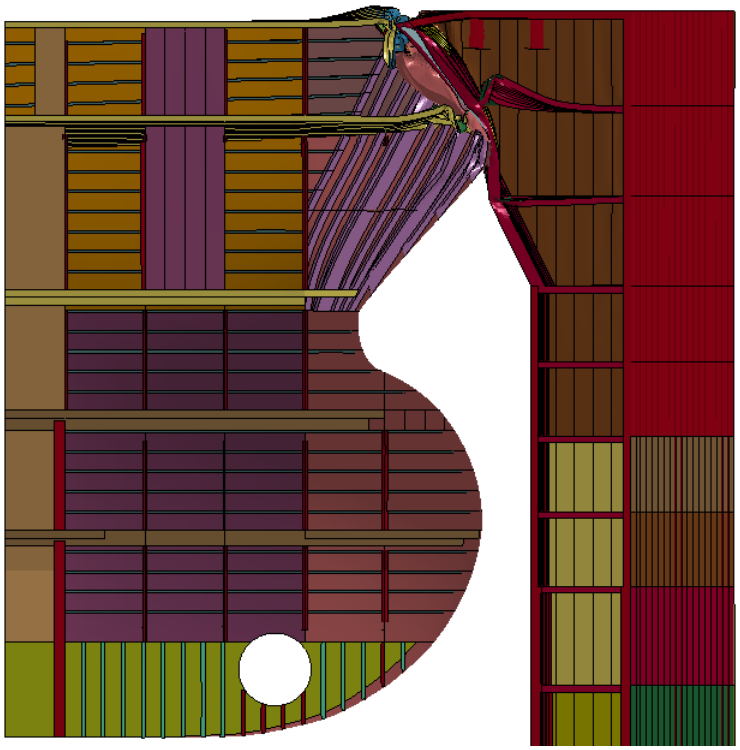

Figure 7.9: Crushing of shuttle tanker forecastle in scenario 1

In scenario 2 (final offloading phase), the shuttle tanker is fully loaded, hence first contact is made between the bulbous bow of the shuttle tanker and the FPSO bilge box. The bulbous bow experience only minor deformations and is crushing the bilge box. A cross-section view of the deformation process is shown in figure 7.10. This indicates that the assumed relative strength between the FPSO bilge box and the bulbous bow in the external dynamic analysis is incorrect, thus the contact surface should have been determined by the curvature of the bulbous bow in scenario 2.

It is observed that the bilge box ruptures when penetrated by the bulbous bow, thus resulting in flooding of one of the ballast compartments. The rupture is shown in figure 7.11. The origin of this rupture is a crack that initiates at the upper corner of the bilge box, in a local hot spot between the outer plate and the stiffener web. This crack propagates as the bilge box is folded flat.

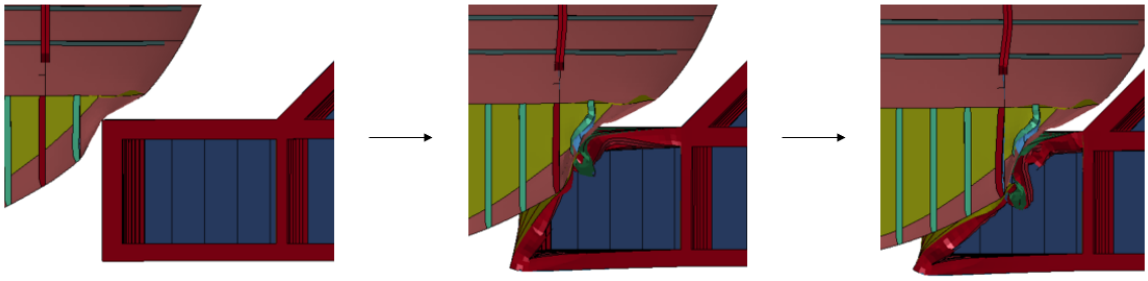

Figure 7.10: Side view of the bilge box crushing process

After penetration of the outer bilge box section, the shuttle tanker forecastle makes contact with the FPSO main hull. The forecastle is then crushed by the main hull in a similar way as described in scenario 1, i.e. plastic bending and progressive buckling of the decks. The major difference in this scenario is the orientation of the contact surface which is vertical in accordance with the FPSO main hull. This can be seen in figure 7.12a which shows the resulting damage in the shuttle tanker after a central impact in scenario 2. Only minor deformations are observed in the main hull of the FPSO as seen in figure 7.12b.

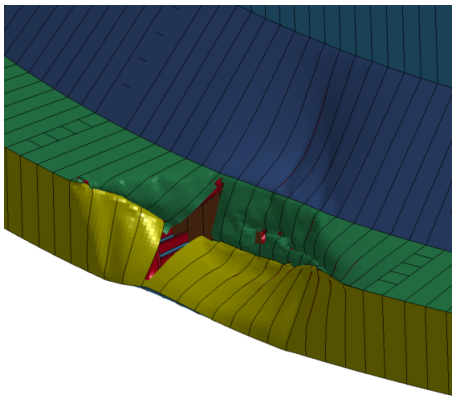

Figure 7.11: Rupture of shell plating in bilge box of the FPSO

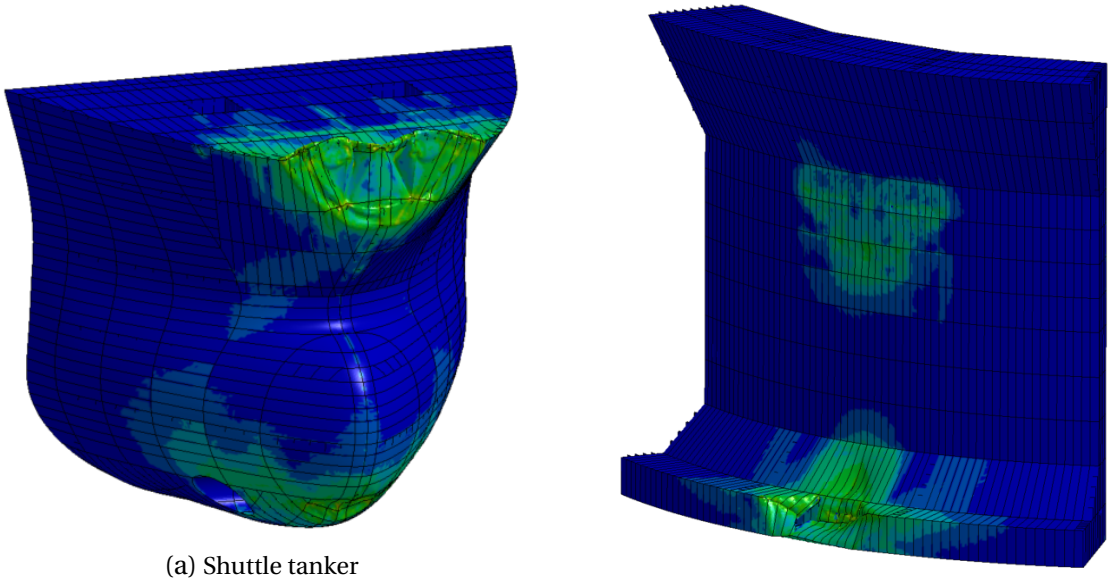

(a) Shuttle tanker

(b) FPSO

Figure 7.12: Damage in the shuttle tanker and the FPSO in scenario 2

In summary, scenario 2 involves two main energy absorbing components: The shuttle tanker forecastle and the FPSO bilge box. This is evident from figure 7.12. A longitudinal cross-section view of scenario 2 is shown in figure 7.13. Since the dissipated energy is equally distributed between the shuttle tanker and the FPSO, see figure 7.6, crushing of the bilge box and forecastle requires an approximately equal amount of energy.

The bulbous bow of the shuttle tanker and the main hull of the FPSO is considered to be equally strong based on the observations from scenario 1 and 2. This can be seen from the force-deformation curves in figure 7.14. When the bulbous bow starts to penetrate the main hull, the slope of the force-deformation curves increases intensely, see figure 7.14a for scenario 1 and figure 7.14b for scenario 2.

An equivalent deformation is used in the force-deformation diagrams. The equivalent deformation was derived based on the internal energy and the resultant reaction force outputs from LS-DYNA. A reversed numerical integration approach, using the trapezoidal rule, was applied to compute the equivalent deformation (i.e. the step size) at every time-step. A common method for computing the deformation is to sample nodal displacements at selected nodes. This method was tested for some of the analyses and the diagrams are included in appendix B. It was found from comparison that the two methods gave quite similar force-deformation curves. However, the equivalent deformation approach was preferred because of time efficiency and the use of global output values, thus avoiding possible uncertainties introduced from bad node selection.

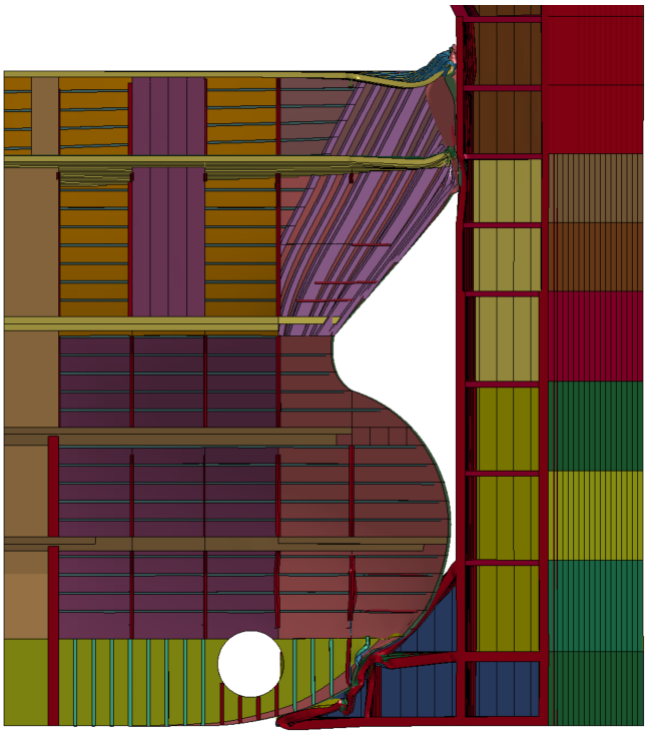

Figure 7.13: Crushing of FPSO bilge box and shuttle tanker forecastle in scenario 2

The force-deformation curves with the equivalent deformation matches the total dissipated energy from the external dynamic analysis with only minor deviations, i.e. the area under the force-deformation curves matches the energy from the external analysis. The maximum deviation was observed for figure 7.14b which deviates by approximately 7%. However, the deviation was normally around 3%, which is reasonable.

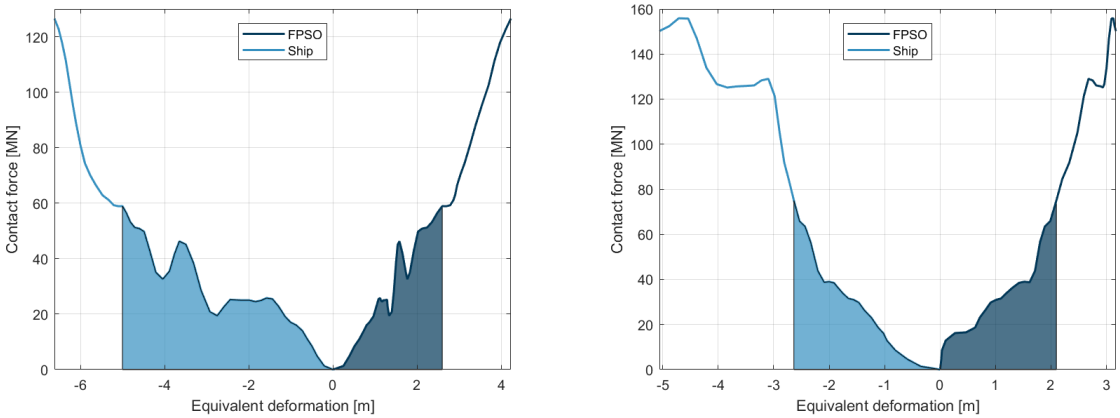


(a) Scenario 1

(b) Scenario 2

Figure 7.14: Force-deformation curves for head-on central impacts with the shuttle tanker

By extending the NLFEA of scenario 1, the bulbous bow eventually penetrates the FPSO hull, resulting in rupture of the shell plating along one of the decks. The damage in the FPSO can be seen in figure 7.15a. Penetration of the main hull requires a lot of energy. Approximately 400 MJ is absorbed at the final time-step of the analysis which is double the amount of dissipated energy involved in scenario 1 and 54% more than the initial kinetic energy. Based on this observation, it is clear that penetration into the cargo compartments, i.e. penetration of the inner hull, is not realistic for drive-off scenarios in the initial offloading phase.

In the extended analysis of scenario 2, it is observed that a crack initiates and propagates along the top of the bilge box fillet, at the boundary to the outer hull. The crack can be seen in figure 7.15b. The total dissipated energy is approximately 250 MJ at this point. This is, however, a conservative estimate since mild steel material properties were used in the NLFEA. The result of the rupture is flooding of the affected double hull compartments at two vertical levels. As the penetration process continues, the inner sections in the bulbous bow starts buckling. The total internal energy at the final time-step of the NLFEA is approximately 600 MJ which is four times the dissipated energy obtained from the external dynamic analysis and over twice the amount of initial kinetic energy involved scenario 2. The cargo storage tanks are still intact.

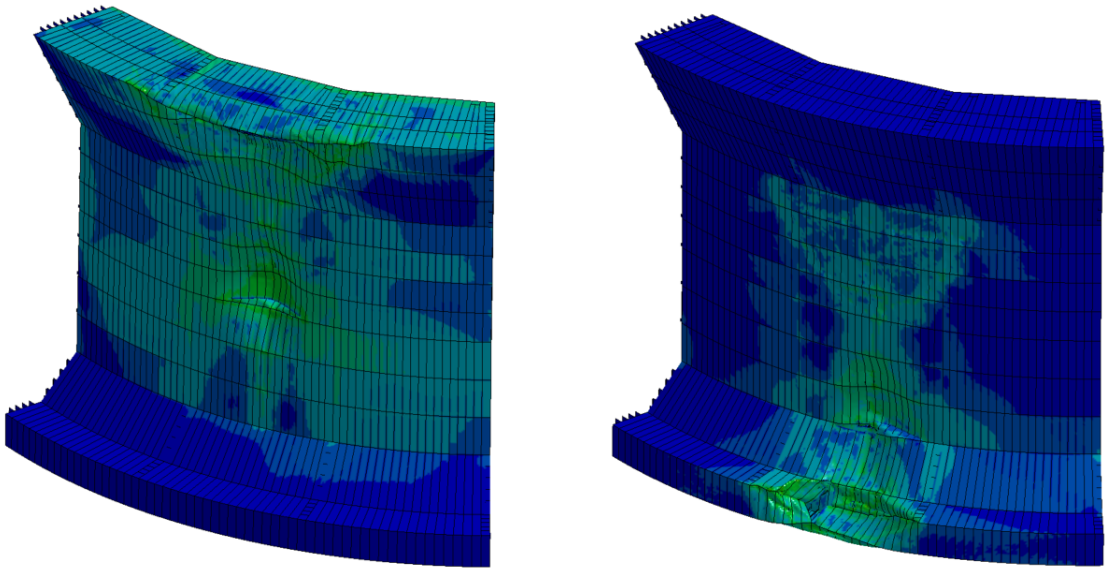

(a) Scenario 1

(b) Scenario 2

Figure 7.15: Damage in the FPSO at the final time-step of the NLFEA

#### 30- and 60-degree glancing impacts

Figure 7.16 shows the development of internal energy in the NLFEA of 30- and 60-degree glancing impacts with the shuttle tanker. Draft variations are according to scenario 1 and 2, as defined in section 3.2. The same scenario numbering is used in the following to define the

drafts. The vertical dashed lines mark the internal energy that corresponds to the dissipated energy from the external dynamic analysis.

It should be mentioned that in the NLFEA of 60-degree impacts, the contact area propagated towards the side boundary of the FPSO model, as seen in figure 7.17. The side boundary is free to move, thus it may affect the resistance in the neighbouring section towards bending and transverse deformation. Ideally, contact should be made in the centre of the FE model to avoid boundary effects. However, only minor displacements were observed in the radial bulkhead that constitutes the side boundary, hence it is assumed that the 60-degree results are reasonable.

Another weakness in the FPSO model is the exclusion of the bulwark structure. This affects the structural response of the main deck and the upper section of the superstructure, making the entire top section less resistant to bending because of the missing stiffness from the bulwark extension. Damage in the superstructure is thus considered without the bulwark structure in mind. This applies for all scenario 1 simulations in this thesis.

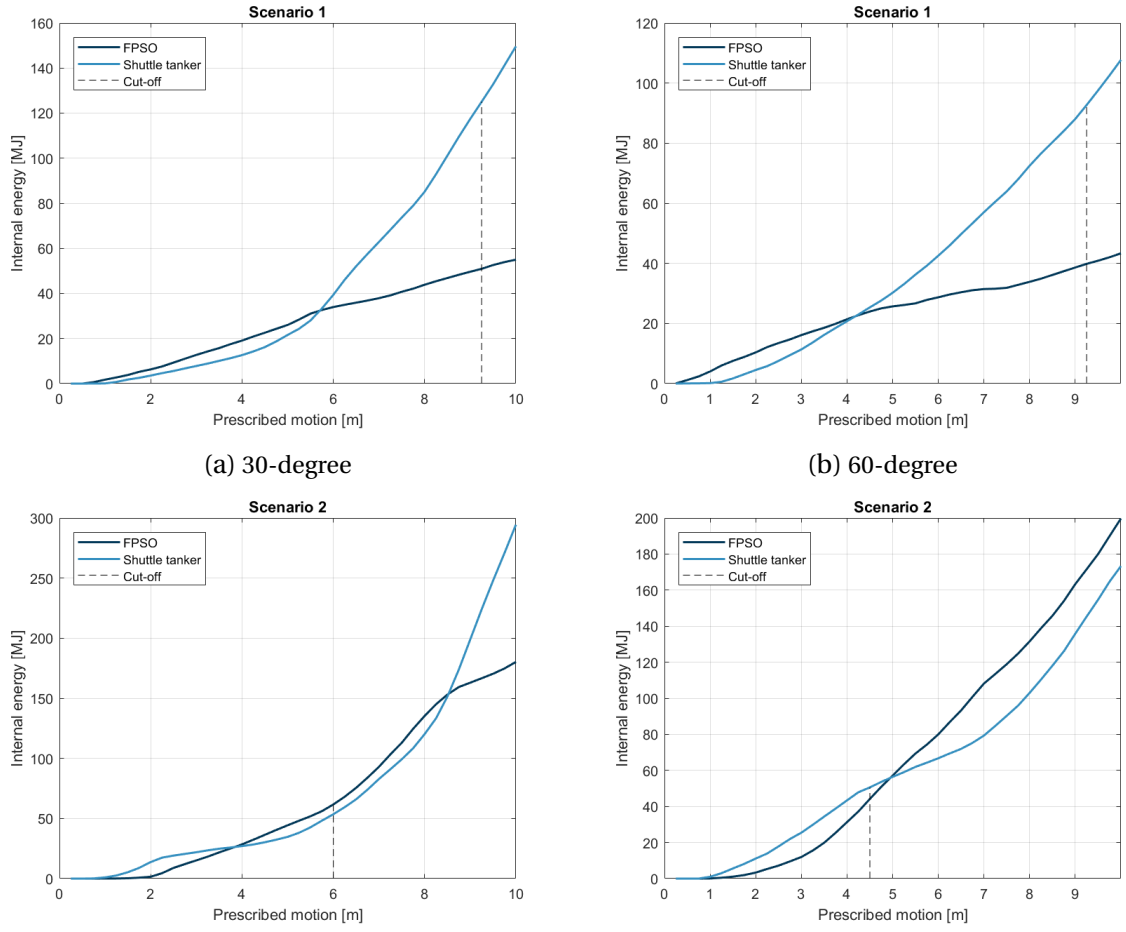


(a) 30-degree

(b) 60-degree

(c) 30-degree

(d) 60-degree

Figure 7.16: Development of internal energy in 30- and 60-degree impacts from the shuttle tanker

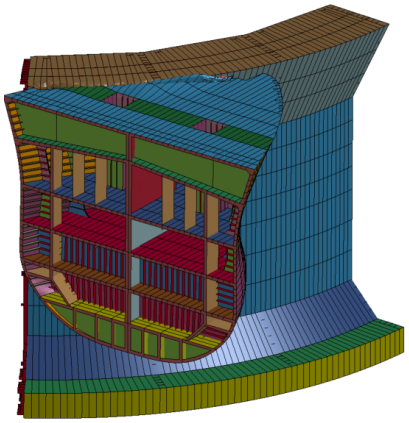

Figure 7.17: 60-degree impact with the shuttle tanker in scenario 1. The final time-step of the NLFEA is shown

It is observed that the ratio of the internal energy between the shuttle tanker and the FPSO strongly depends on the draft variations, similar to central impacts. In scenario 1 (the initial offloading phase), the shuttle tanker absorbs approximately 2.5 times more energy than the FPSO. The energy absorbed by the shuttle tanker constitutes 71.1% and 69.9% of the total dissipated energy in the 30- and the 60-degree impact, respectively. In scenario 2 (the final offloading phase), the ratio of internal energy is closer to one. The shuttle tanker absorbs 46.5% and 53.4% of the total dissipated energy in the 30- and the 60-degree impact, respectively. Based on these observations, it is clear that scenario 2 results in the largest strain energy dissipation in the FPSO.

Figure 7.18 shows the damage in the shuttle tanker and the FPSO after a 30-dergee impact in the initial offloading phase (scenario 1). It is observed that the resistance in the shuttle tanker forecastle is larger in non-central impacts compared to the central impact in the previous subsection. This is because the vertical stiffeners in the front of the forecastle have a more perpendicular orientation to the contact surface. Eventually, the top of the shell plating in the forecastle experience plastic bending and the main deck starts to buckle. The deformation process is similar to the central impact, i.e. plastic bending of the shell plating and progressive folding of the main deck.

An interesting observation is that the FPSO superstructure ruptures in the 30-degree impact in scenario 1. This can be seen in figure 7.18a. The rupture process is shown in figure 7.19. It is believed that this event is of less importance because of the elevation over the sea surface, hence flooding of the compartment will not occur. However, in rough sea the compartment may fill up with sea water. Rupture of the shell plating in the superstructure is not observed in the 60-degree impact. The bulbous bow does not make contact with the FPSO hull in any of the two non-central impacts in scenario 1.

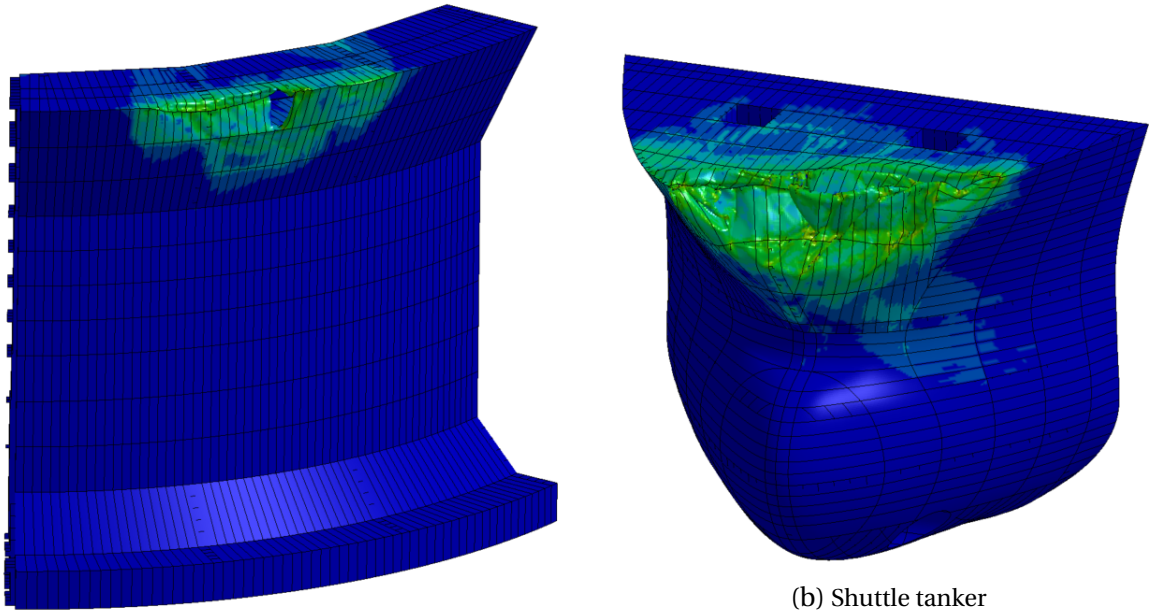

(a) FPSO

(b) Shuttle tanker

Figure 7.18: Damage in the FPSO and the shuttle tanker after a 30-degree impact in scenario 1

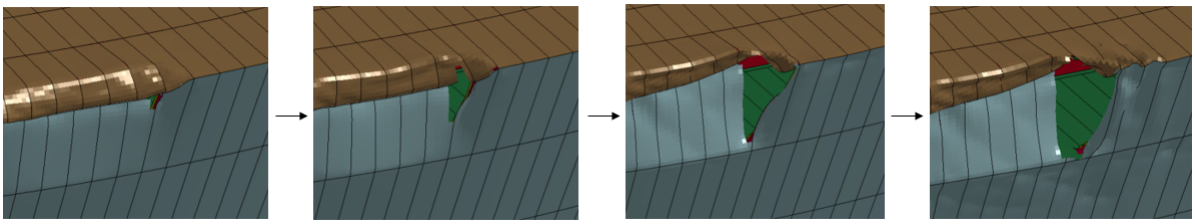

Figure 7.19: Rupture of shell plating in the FPSO superstructure

Figure 7.20 shows the damage after a 30-degree glancing impact in the final offloading phase (scenario 2). Figure 7.21 shows the same scenario, but with a 60-degree impact angle.

In figure 7.20b it is seen that the side section of the bulbous bow is imprinted by the FPSO bilge box. This deformation pattern is even more evident in the 60-degree impact in figure 7.21b. The NLFEA shows a trend towards a more equally shared deformation process between the bulbous bow and the bilge box for increasing impact angles. Plastic deformation of the bilge box is gradually reduced as the impact angle increases and the strength of the bulbous bow seems to reduce when contact is made in the side section. The FPSO main hull is still much stronger than the shuttle tanker forecastle, thus the forecastle is crushed in the normal direction to the main hull in every analysis.

In the 30-degree impact, small cracks are observed in the upper corner of the bilge box, but crack propagation is not that prominent as observed in the central impact. The result is still flooding of the ballast compartment in the outer section of the bilge box.

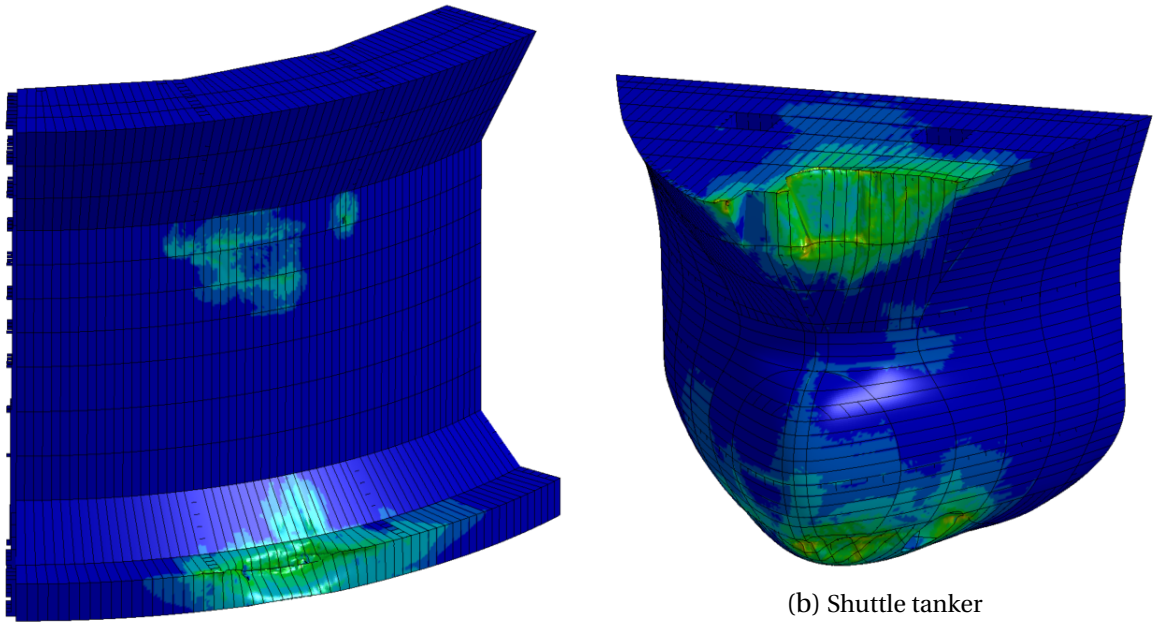

(a) FPSO

(b) Shuttle tanker

Figure 7.20: Damage in the FPSO and the shuttle tanker after a 30-degree impact in scenario 2

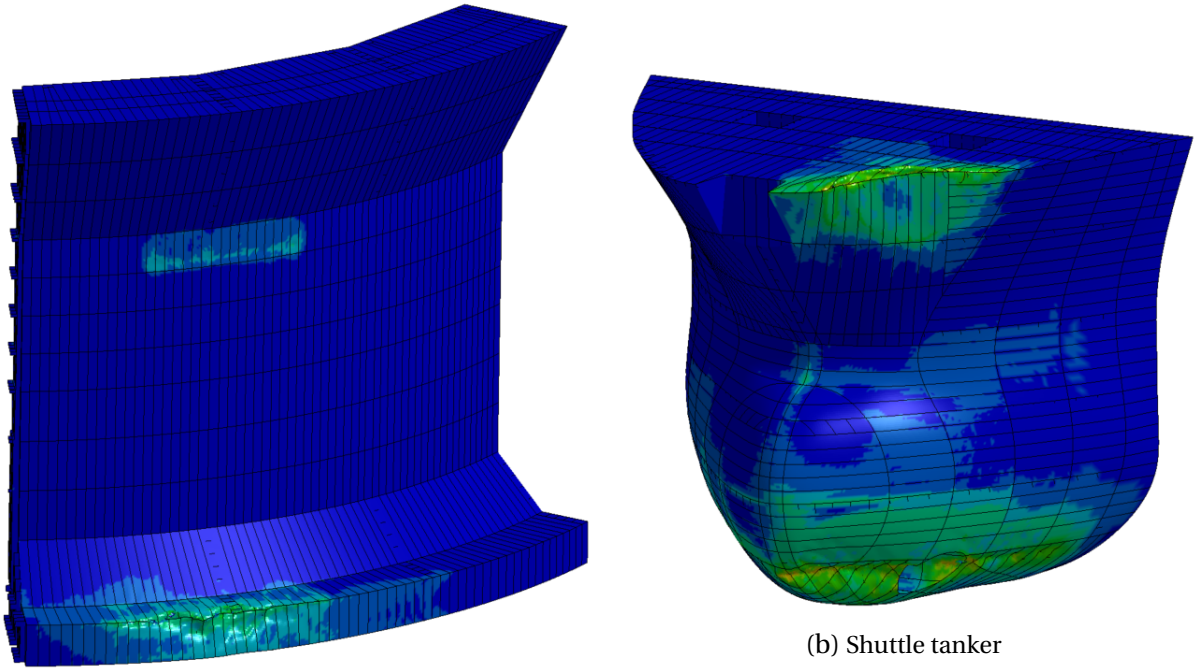

(a) FPSO

(b) Shuttle tanker

Figure 7.21: Damage in the FPSO and the shuttle tanker after a 60-degree impact in scenario 2

Figure 7.22 shows the force-deformation curves for 30- and 60-degree glancing impacts in the initial and final offloading phase (scenario 1 and 2). An equivalent deformation, which is based on the internal energy and the resultant reaction force as described earlier, is used. The total area under the curves corresponds to the dissipated energy found in the external dynamic analysis.

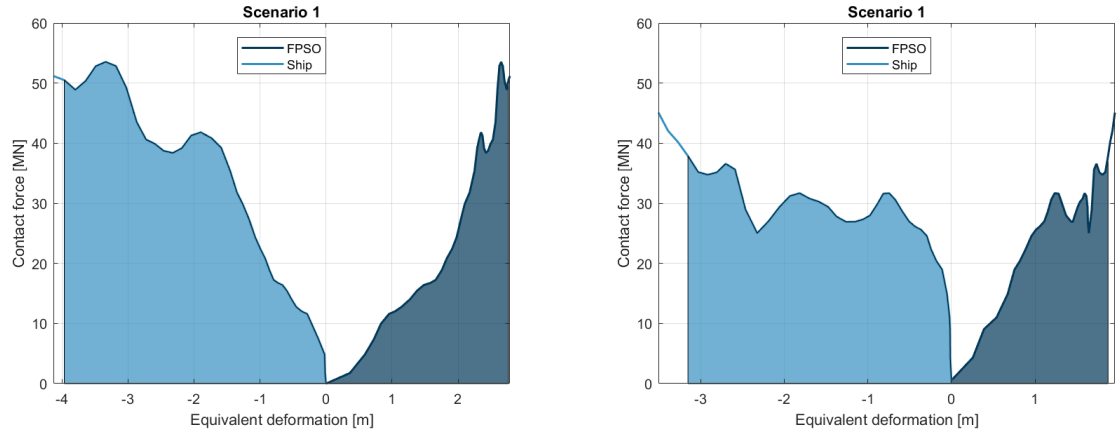


(a) 30-degree




(b) 60-degree

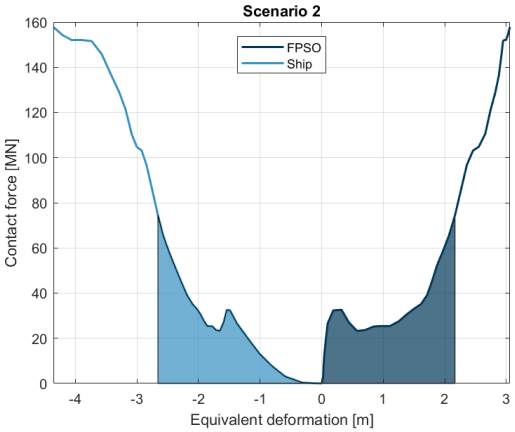


(c) 30-degree

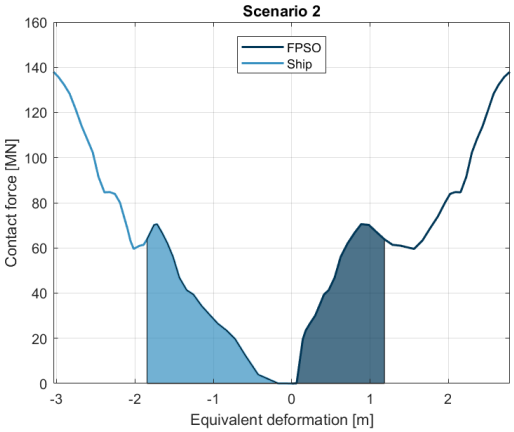


(d) 60-degree

Figure 7.22: Force-deformation curves for 30- and 60-degree impacts from the shuttle tanker

### 7.3.2 Impacts from a supply vessel with X-BOW

This section studies a head-on central impact from a supply vessel with X-BOW. Glancing impacts from a supply vessel with a "traditionally" shaped bow is analysed in chapter 8 using a coupled approach. The user defined material was applied to both the FPSO and the supply vessel. This was unfortunately a mistake made when modifying the LS-DYNA keyword file, thus the effect of the ice-strengthening in the supply vessel is reduced. Originally, Pettersen (2008) used a high strength steel in the ice-strengthened sections in accordance with the DNV ice class, ICE-C. However, it is believed that the FPSO also uses a stronger steel, hence

the results presented in this section are assumed to be reasonable. Still, the relative strength may be incorrect.

Figure 7.23 shows the development of internal energy in the NLFEA of the head-on central impact from the X-BOW supply vessel. Prescribed motion with constant velocity was used. For simplicity, it was assumed that the supply vessel data used in the external dynamic analysis also applies for the current vessel, hence a coupling with the results from section 7.1.2 were enabled. The dashed lines in figure 7.23 mark the total dissipated energy corresponding to the external analysis. Two initial velocities were considered: 2 m/s and 4 m/s.

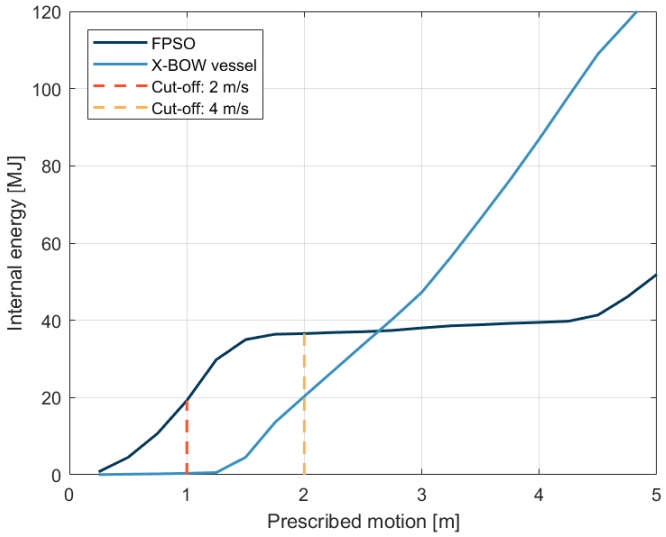


Figure 7.23: Development of internal energy in a head-on central impact with the X-BOW supply vessel

It is observed that the FPSO absorbs the largest amount of energy in both scenarios. If the striking ship velocity is 2 m/s, the FPSO is responsible for approximately all of the energy dissipation. When the initial velocity is 4 m/s, the shell plating in middle section of the supply vessel bow starts to buckle, thus the ratio of internal energy between the bodies levels out. Still, the energy dissipated by the FPSO constitutes 64.3% of the total amount. The structural resistance in the supply vessel bow collapses dramatically after buckling occurs in the shell plating. The bow is crushed flat as the prescribed motion continues. The initiation of the structural collapse can be seen between 1m and 2m of prescribed motion in figure 7.23. The supply vessel bow is very strong up to the initiation of buckling.

Figure 7.24 shows the damage in the FPSO and the supply vessel after an impact with an initial velocity of 2 m/s. From the figure, it can be seen that the sharp X-BOW imprints the main hull of the FPSO. The deformation is local and extends vertically. It is observed that the damage in the FPSO hull is quite similar to the damage caused by the bulbous bow of the shuttle tanker. The difference is that the damage from the blunt bulbous bow dominates in one single deck (depends on the vessel draft) and extends in the horizontal direction. The

damage caused by the X-BOW is distributed among several decks and the imprint has an elliptical shape. This can be seen in figure 7.25 which shows the structural response inside the double hull of the FPSO when penetrated by the X-BOW (7.25a) and the bulbous bow of the shuttle tanker (7.25b). The penetration depth is equal to 1 m in both scenarios and the colour contours are according to the resultant displacement.

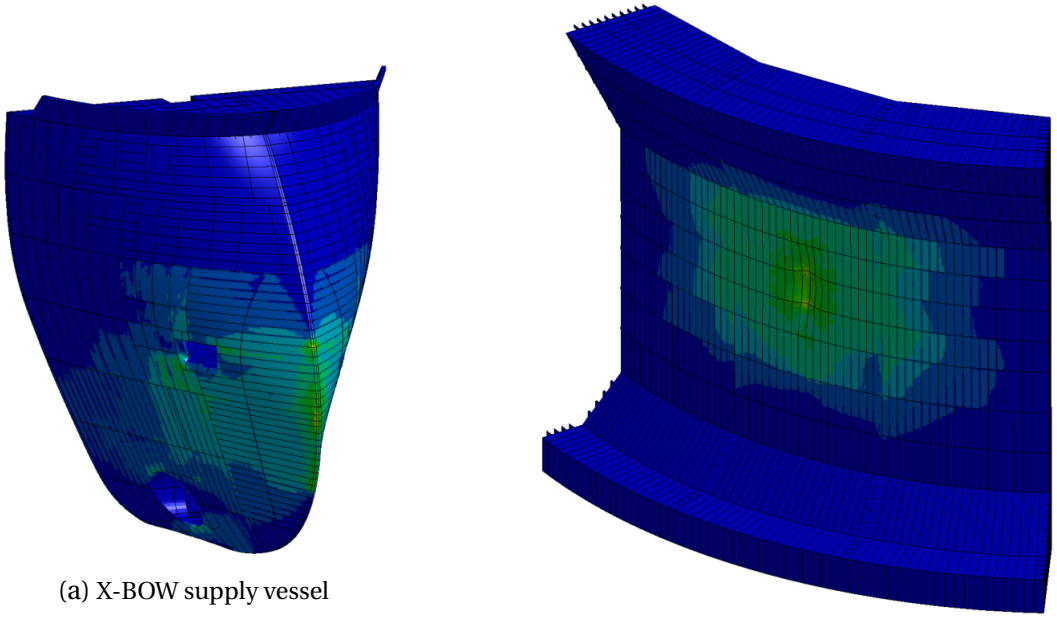

(a) X-BOW supply vessel

(b) FPSO

Figure 7.24: Damage after a head-on central impact with the X-BOW supply vessel. The initial velocity is 2 m/s

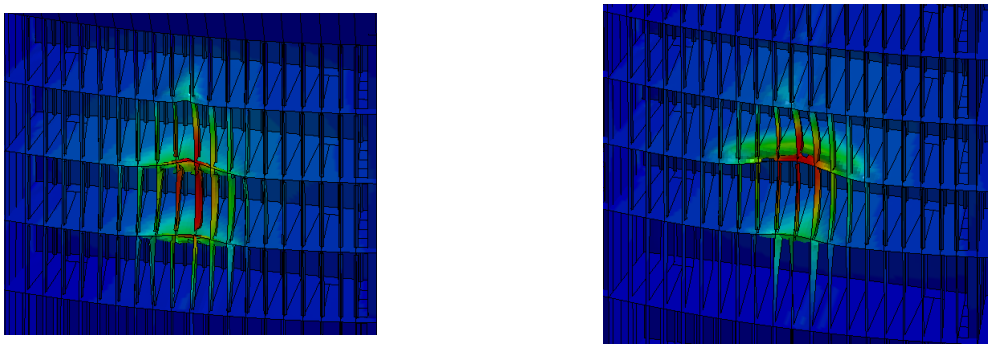

(a) X-BOW supply vessel

(b) Bulbous bow of the shuttle tanker

Figure 7.25: Internal view of the damage in the FPSO hull. The penetration depth is 1 m and the colouring is according to the resultant displacement

Figure 7.26 shows the damage in the supply vessel and the FPSO after a collision with an initial velocity of 4 m/s. It is observed that the shell plating in the supply vessel, in the transition zone between horizontal and vertical stiffening, starts buckling. The deflection extends

vertically across the whole bow section as seen from the vertical stress concentration highlighted by green colour in figure 7.26a. The result is a dramatic reduction of the supply vessel strength. The whole section collapses in longitudinal direction and is crushed flat as the prescribed motion continues. From this point, the FPSO does not experience any further deformation. No ruptures in the FPSO hull is observed.

The dramatic change in relative strength, from a ductile design scenario to a strength design scenario, may be because of the incorrect material properties in the ice-strengthened sections of the supply vessel. However, the transition zone between horizontal and vertical stiffening will be vulnerable with respect to plate buckling, thus a similar structural behaviour may be present in a central impact.

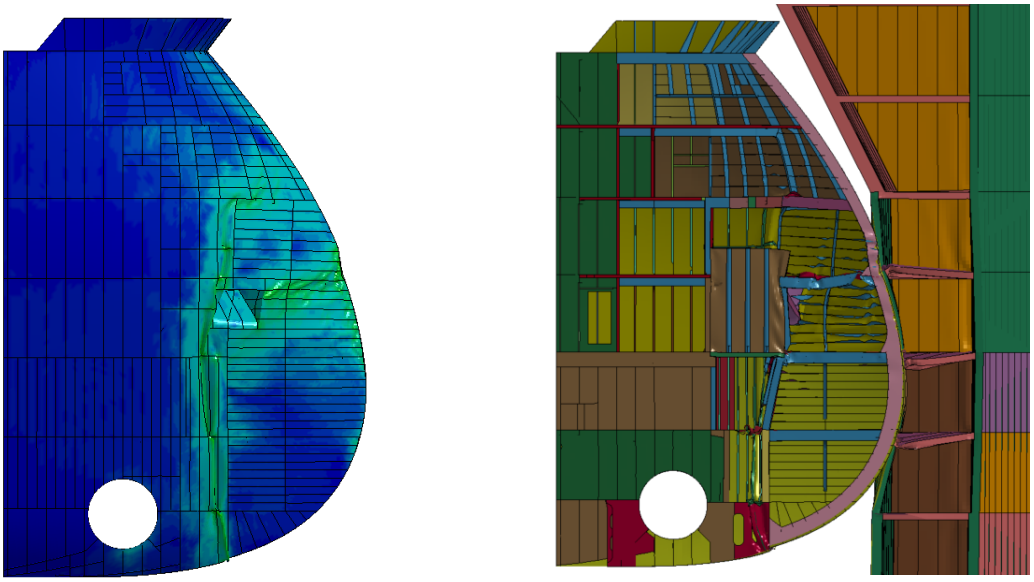

(a) X-BOW supply vessel

(b) Longitudinal cross-section view

Figure 7.26: Damage after a head-on impact with the X-BOW supply vessel. The initial velocity is 4 m/s

Figure 7.27 shows the force-deformation curves for the central impact. An equivalent deformation is used. The first peak value of the supply vessel corresponds to the structural collapse of the inner bow section as described in the previous paragraphs. The orange and the light blue coloured areas mark the dissipated energy involved in the 2 m/s impact and the 4 m/s impact, respectively.

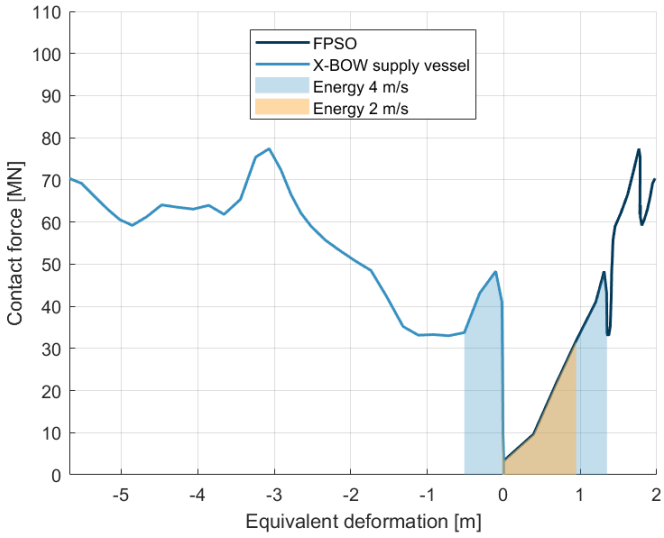


Figure 7.27: Force-deformation curves for head-on impact with the X-BOW supply vessel

### 7.3.3 Impacts from an infinitely rigid shuttle tanker

NLFEA using an infinitely rigid shuttle tanker were carried out in order to establish a lower limit of the energy requred to penetrate the FPSO hull. This corresponds to a ductile design approach. The mild steel material properties from table 6.1 in chapter 6 were applied to the FPSO and the rigid material was applied to the shuttle tanker bow. Figure 7.28 shows the internal energy in the FPSO hull for central impacts in scenario 1 and 2. The points where the outer and inner hulls are punctured are indicated in the figure by a red cross and circle.

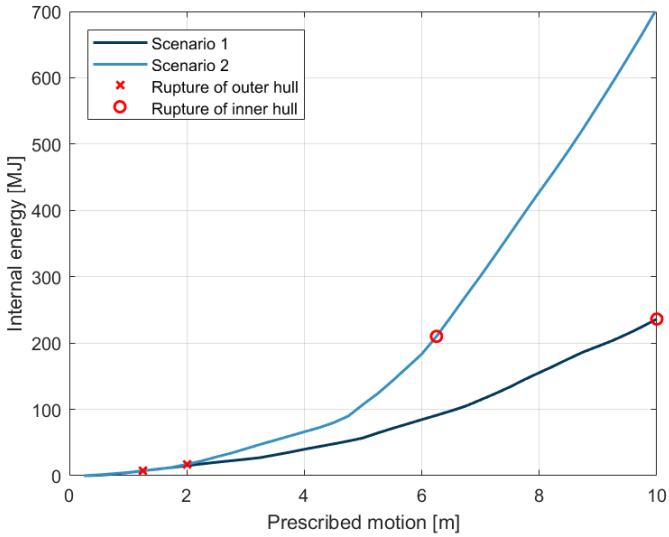


Figure 7.28: Internal energy in the FPSO when subjected to central impacts form a rigid shuttle tanker bow

The lower limits of the required energy were established by computing the average of the internal energy between the scenarios. The lower limit for puncturing of the outer hull was estimated to be 12 MJ, and 223 MJ for puncturing of the inner hull. A cross-section view of the penetration of the inner hull is shown in figure 7.29 for scenario 1 and 2.

The estimated energy limits are unrealistic. The dissipated energy associated with penetration of the FPSO hull when assuming ductile design is much lower compared to a shared-energy scenario. This is because the rigid shuttle tanker easily penetrates through the hull due to the pointy tips of the forecastle. The forecastle front creates a very localized deformation in the hull, thus only a small amount of energy is required to erode the most vulnerable elements. When comparing to the shared-energy analyses in the previous sections, it is evident that this behaviour is incorrect. The shared-energy approach showed that the strength of the FPSO hull is much larger than the shuttle tanker forecastle. A better approach would therefore be to only model the bulbous bow as rigid or sections that corresponds with ice-strengthening.

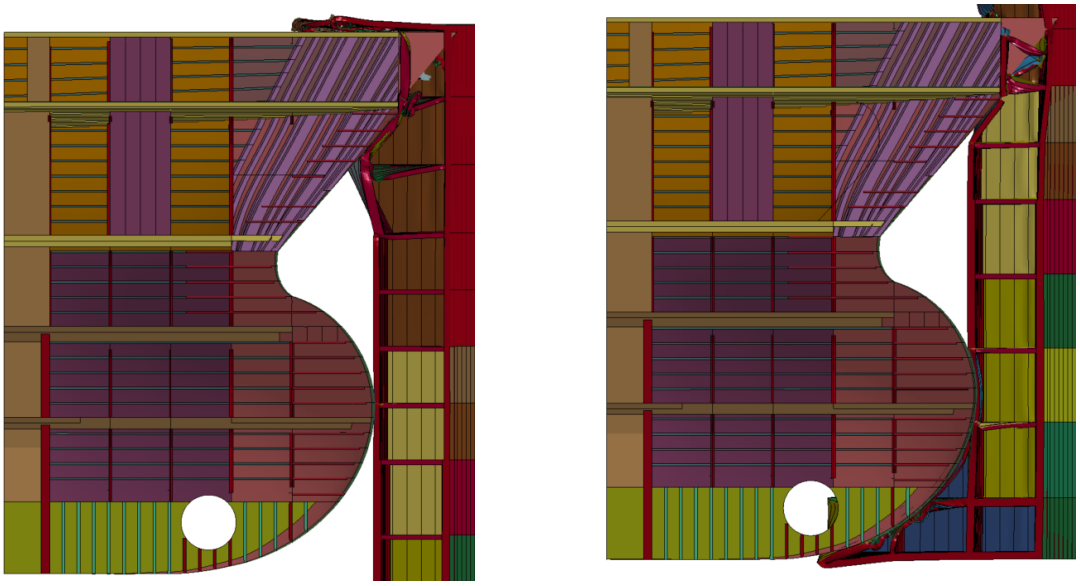

(a) Scenario 1

(b) Scenario 2

Figure 7.29: Penertation of the inner hull by a fully rigid shuttle tanker

In summary, the ductile design approach gives a very wrong impression of the relative damage in this analysis, thus it is not recommended to use ductile design for assessment of shuttle tanker – FPSO collisions. However, ductile design may be reasonable in other collision scenarios. For example, the analysis of the X-BOW supply vessel collision showed that the X-BOW had sufficient strength to penetrate the FPSO hull for initial velocities up to 4 m/s, thus ductile design may be reasonable in that case due to the ice-strengthening and the bow geometry.

# Chapter 8

# Coupled Analysis of Glancing Impacts from a Supply Vessel

## 8.1 30-degree glancing impact

Figure 8.1 shows the time history of the kinetic energy of the striking supply vessel, the internal energy of both the supply vessel and the FPSO, and the total sliding energy. The sliding energy is the sum of the frictional energy and the contact energy which is the energy required to prevent penetration of a master segment by slave nodes as described in section 2.3.2. The initial velocity of the supply vessel is 2 m/s and the mass is 7,500 tonnes, thus the initial kinetic energy is 15 MJ.

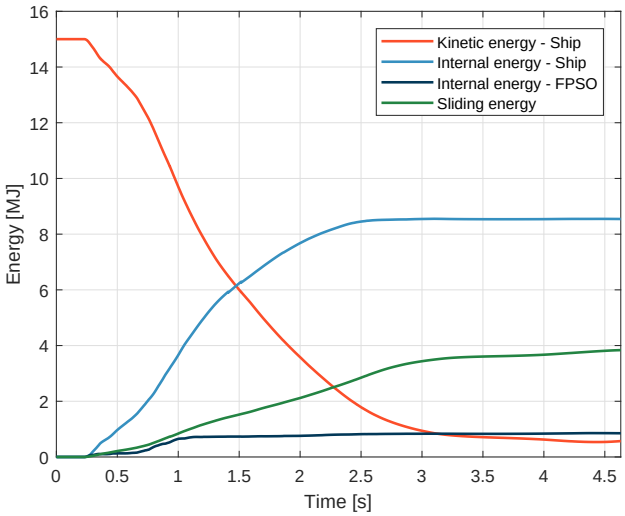


Figure 8.1: Energy involved in a 30-degree glancing impact from a supply vessel

Approximately 96% of the initial kinetic energy is dissipated by impact. Out of the total dissipated energy, 65.1% is absorbed as internal energy, 26.6% is absorbed as sliding energy and 1.4% is absorbed as hourglass energy. For the sliding energy, it is observed that the frictional energy is dominating compared to the contact energy. The ratio of internal energy between the supply vessel and the FPSO is approximately 10, thus the supply vessel is the major energy absorbing object in this analysis.

The hydrodynamic solver used in the coupled model is not fully integrated into LD-DYNA, meaning that the hydrodynamic loads are computed and applied to the model, but global variables are not updated with respect to these hydrodynamic effects. For this reason, the output energy from LS-DYNA is not necessary in balance with the initial energy. Based on discussions with the co-supervisor, it is assumed that the missing 6.9% of the energy is dissipated by wave making forces.

The total amount of dissipated energy in the coupled analysis matches the external dynamic analysis well. However, the considerable sliding energy indicates that the assumption of only strain energy dissipation, made in the decoupled analysis in this thesis, is somewhat incorrect. The consequence is an overestimation of the structural damage in the internal mechanics (e.i. the results in section 7.3).

Figure 8.2 shows the rigid body motions of the supply vessel. As expected, it is observed that the surge motion is heavily reduced. Motions caused by engine thrust in a drive-off scenario are not considered, thus the vessel will drift throughout the impact. Therefore, the final surge velocity is only 0.048 m/s which is in good agreement with the external dynamic analysis. The coupled model shows elements of sway, heave, roll, pitch and yaw motions. The sway and heave motions are moderate which is somewhat unexpected. Still, pitch and yaw motions dominate compared to the sway and heave motions, thus the assumption of insignificant sway and heave motions in the externa dynamic analysis is reasonable. The ship motions throughout the impact can be seen in figure 8.3 which shows the path of the bulbous bow front together with the structural damage in the supply vessel forecastle.

The external dynamic analysis predicts a sticking mechanism with a shared residual motion for the 30-degree supply vessel impact. Due to the fixed boundary conditions of the FPSO, the NLFEA cannot simulate sticking unless the objects hook together because of deformation or structural protrusions that absorbs all the kinetic energy. Thus, when the sticking mechanism applies, the coupled and decoupled approach will estimate different rigid body motions. The static friction coefficient used in the NLFEA is 0.3 which is lower than the one used in the external dynamic analysis ($\mu_0 = 0.6$). As observed in section 7.1 and 7.2, the static friction coefficient $\mu_0$ has a major influence on the sticking-sliding mechanism. If $\mu_0 = 0.3$ is used, sliding with significant pitch and yaw motions occurs. However, the total dissipated energy then becomes 10.3 MJ which is 72% of the dissipated energy in the coupled analysis.

In addition, the residual velocities deviates from the coupled analysis. It is therefore believed that $\mu_0 = 0.6$ generates more reasonable results.

From figure 8.3, it is observed that the supply vessel forecastle is crushed by the FPSO superstructure. The damage in the FPSO is insignificant with only small indentations. The bulbous bow does not make contact with the FPSO hull. Based on these observations, it is clear that glancing impacts from the supply vessel do not constitute a threat to the FPSO. This may, however, change if an ice-strengthened supply vessel is involved or a strong bulbous bow makes contact with the FPSO hull.

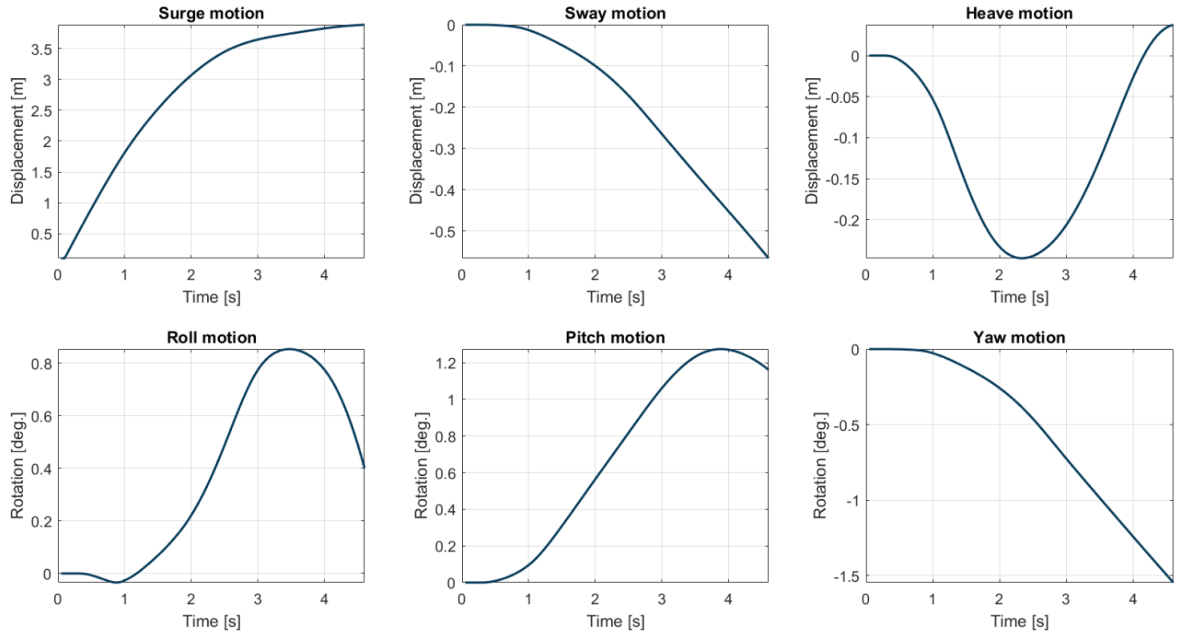


Figure 8.2: Rigid body motions of the supply vessel in a 30-degree glancing impact

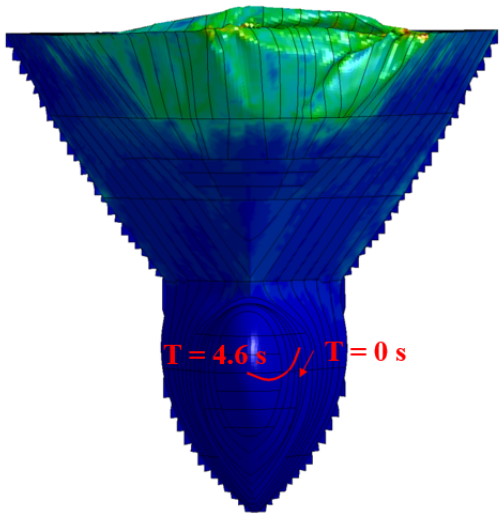


(a) Front view

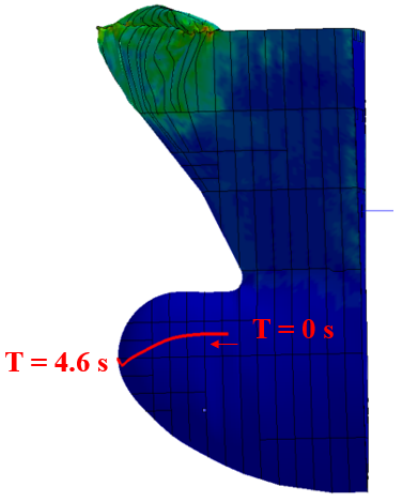


(b) Side view

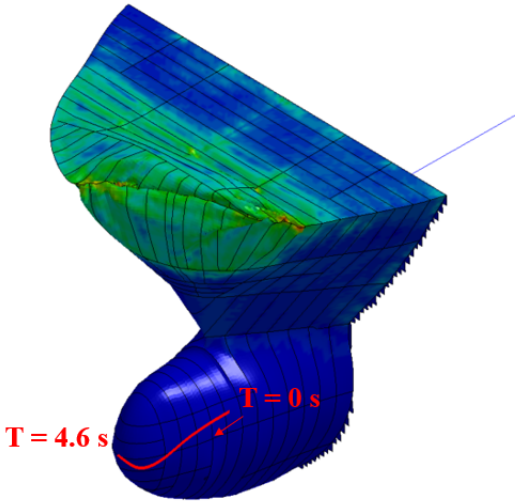


(c) 3D view

Figure 8.3: View of the motion history of the bulbous bow front and the structural damage in the supply vessel forecastle after a 30-degree impact with an initial velocity of 2 m/s

## 8.2 60-degree glancing impact

Figure 8.4 shows the development of energy in the 60-degree glancing impact. The initial conditions are the same as in section 8.1, thus the initial kinetic energy is 15 MJ. The total dissipated energy is 3.9 MJ which is far less than the dissipated energy from the external dynamic analysis. The reason for this large difference is the duration of the sticking mechanism due to the larger friction coefficient used in the external mechanics. The sticking mechanism affects the level of energy dissipation in the succeeding sliding impacts.

Approximately 26% of the initial kinetic energy is dissipated as a combination of internal

energy (9.4%), sliding energy (15.1%), and wave radiation energy (≈1.5%). The hourglass energy is insignificant. An interesting observation is that the friction between the colliding objects is the main energy absorbing mechanism. This may indicate a trend where the sliding energy dominates for large impact angles, thus the reduction of strain energy absorption found in the external dynamic analysis may be larger. The consequence is that the estimated damage in section 7.3 is too large.

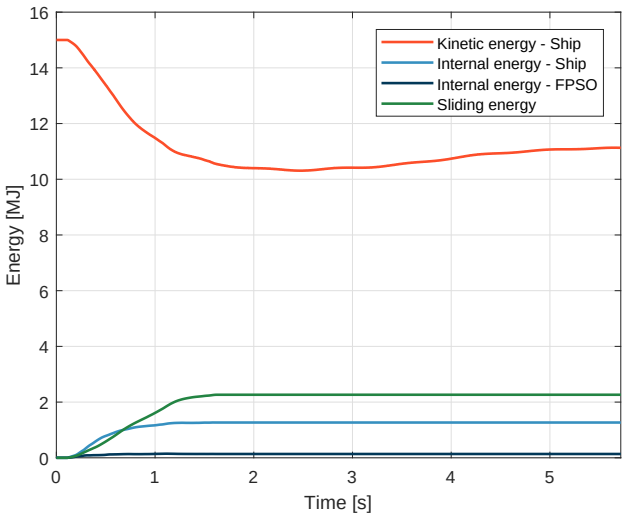


Figure 8.4: Energy involved in a 60-degree glancing impact from a supply vessel

Figure 8.6 shows the rigid body motions of the supply vessel. It is observed that the yaw motion is prominent together with the surge motion. The amplitude of the oscillations in heave and roll are minor, thus these motions are not of importance. This does also apply for the pitch motion. The rigid body motions can be more easily interpreted by looking at the bulbous bow trace lines in figure 8.6.

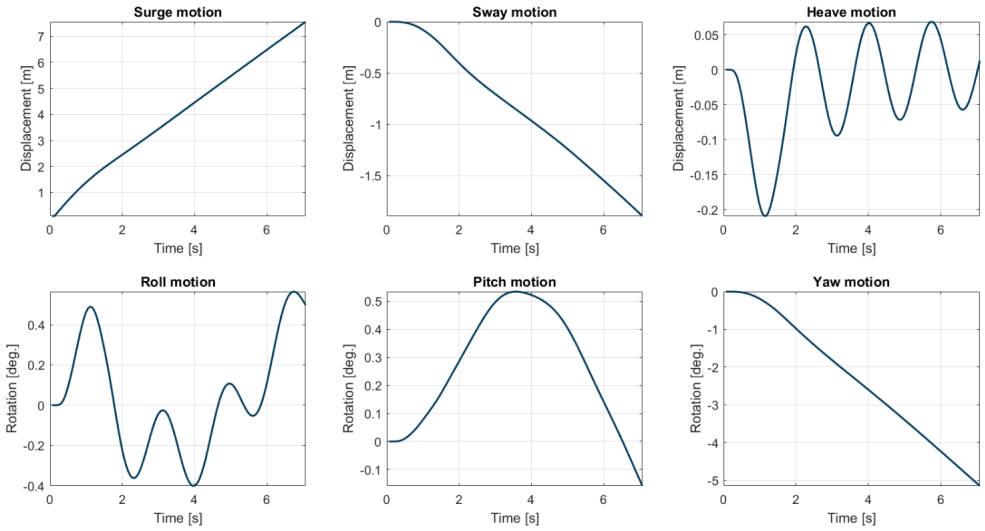


Figure 8.5: Rigid body motions of the supply vessel in a 60-degree glancing impact

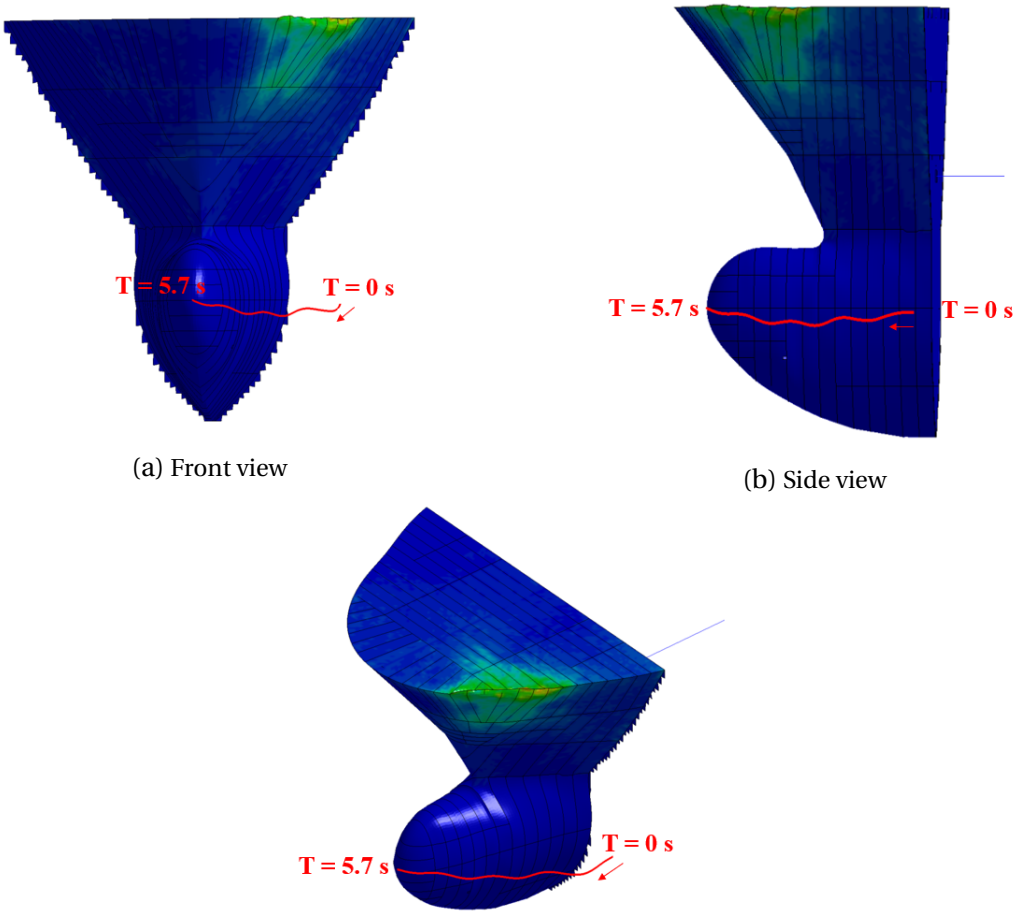


(a) Front view

(b) Side view

(c) 3D view

Figure 8.6: View of the motion history of the bulbous bow front and the structural damage in the supply vessel forecastle after a 60-degree impact with an initial velocity of 2 m/s

It is found that the supply vessel absorbs approximately 9 times more energy than the FPSO: 1.27 MJ versus 0.14 MJ. However, compared to the 30-degree impact and the analyses in section 7.3, the structural damage is insignificant in this scenario. Further discussions of this scenario are thus omitted.

## 8.3 Coupled versus decoupled approach

When comparing the coupled and decoupled approach, it is clear that the inclusion of the rigid body motions and the hydrodynamic effects in the NLFEA gives a better representation of the impact process. A major advantage with the coupled model is the complete time history of the kinetic energy, internal energy, sliding energy and other relevant contributions. This cannot be obtained with the decoupled approach because it only includes the initial and final state of the impact. However, the coupled approach can be challenging to implement into FE softwares. In addition, only the rigid body motions of the striking ship are obtained (as of today).

A major downside with the coupled approach is the very long duration of the NLFEA because a large number of time-steps is required to fully capture the hydrodynamic response. As of today, only shared memory parallel (SMP) processing is available for the coupled model, thus LS-DYNA runs are limited to only one node on HPC systems. In general, massively parallel processing (MPP) solves a LS-DYNA problem faster and enables the use of several nodes on a HPC system. Thus, MPP analysis is usually the preferred method.

# Chapter 9

# Conclusions and Recommendations for Future Work

## 9.1 Conclusions

This thesis has studied the damage in the Sevan 1000 FPSO when subjected to impacts from a 150,000 DWT shuttle, a 7,500 DWT supply vessel and a ULSTEIN X-BOW supply vessel. The focus has been on central and glancing shuttle tanker impacts. Two main impact scenarios were established based on an upper limit drive-off velocity and the variations in draft in accordance with the initial and final offloading phase. A FE model of the Sevan 1000 FPSO was created and implemented into the numerical code LS-DYNA for NLFEA.

The overall conclusion is that the FPSO withstands a collision from the shuttle tanker with good margin. From the 6DOF external dynamic analysis, it was found that the maximum dissipated energy associated with a head-on impact in the initial offloading phase is approximately 204 MJ, while for a similar impact in the final offloading phase the maximum dissipated energy is 147 MJ. For glancing impacts, the energy dissipation is gradually reduced as the impact angle increases. However, the reduction is highly affected by a sticking-sliding mechanism which in turn is affected by the applied static friction coefficient. Head-on impacts from the supply vessel gave a total dissipated energy of 14.5 MJ and 57.8 MJ when the initial velocity is 2 m/s and 4 m/s, respectively.

From the assessment of local structural response, it was found that the FPSO superstructure is crushing the shuttle tanker forecastle, while the bulbous bow of the shuttle tanker is crushing the FPSO bilge box. The bulbous bow starts to show significant damage when contact is made with the main hull of the FPSO. The FPSO hull remains intact in all the drive-off impact scenarios studied, with the exception of a large rupture in the bilge box caused by the bulbous bow and a rupture in the FPSO superstructure that appears in the 30-degree glanc-

ing impact in the initial offloading phase. Flooding of the associated compartments is not believed to affect the FPSO in any major way.

The damage in the FPSO after a glancing impact from the 7,500 DWT supply vessel is insignificant. However, a central impact from the X-BOW supply vessel resulted in significant penetration of the FPSO hull. It was observed that the X-BOW structure eventually started to collapse, hence limiting the damage in the FPSO hull. The structural collapse is most likely because of the mild steel properties that were applied to all the FE models, thus the effect of the ice-strengthening in the X-BOW was reduced. However, the results are assumed to be reasonable since the same material was used in the FPSO.

By using an infinitely rigid shuttle tanker, a lower limit of 12 MJ was obtained for puncturing of the outer hull and 223 MJ for the inner hull of the FPSO. These limits are, however, unreasonable because the resulting deformation does not match the more realistic damage observed in the shared-energy simulations. A ductile design approach is therefore not recommended for assessment of shuttle tanker – FPSO collisions.

From the coupled analysis of glancing supply vessel impacts in section 8.1 and 8.2, it was found that the rigid body motions in surge, pitch and yaw dominates for the striking vessel, but the intensity of each component is dependent on the impact angle. No residual motions are obtained for the FPSO due to the boundary conditions. In addition, it was observed that the importance of the sliding energy increased together with the glancing angle. The coupled NLFEA model matches the external mechanics model well. However, various elements introduced by assumptions, like the sticking-sliding mechanism, makes the results deviate on certain levels.

## 9.2 Recommendations for future work

Recommendations for future work are summarized by the following bullet points:

- Create two seperate contact definitions in LS-DYNA for the forecastle and the bulbous bow of the shuttle tanker so that the contact force can be determined for each structural part.
- Perform NLFEA of shuttle tanker – FPSO impacts, or other shuttle tanker impacts, with the coupled hydrodynamic model developed by Yu & Amdahl (2016) in LS-DYNA. Coupled analysis of shuttle tanker impacts was unfortunately omitted in this thesis due to time limitations. The coupled model by Yu & Amdahl (2016) has so far not been tested for other types of ships than the supply vessel used in this thesis and the work by Yu (2017).

- Perform NLFEA with a FE model of the complete Sevan FPSO to study global rigid body motions. The coupled hydrodynamic model by Yu & Amdahl (2016) can be applied to the striking ship for a wet-dry simulation, where hydrodynamic effects are not considered for the FPSO (constant added mass can be added to the FPSO), or if possible, the coupled model can be applied to both objects for a wet-wet simulation (this would be particularly interesting).
- Study the local structural response in the Sevan 100 FPSO when subjected to impacts from ice-strengthened shuttle tankers.
- Evaluate the stability of the Sevan FPSO with flooded compartments.
- Improve the outputs from the external mechanics model by Liu & Amdahl (2010) so that global rigid body motions can be better determined in all 6 DOFs.
- Parametric study of e.g. friction coefficient, coefficient of restitution and other parameters involved in the external mechanis to improve the accuracy of simplified methods.

# Bibliography


Alsos, H. S. (2008), 'Ship grounding : analysis of ductile fracture, bottom damage and hull girder response'.

Amdahl, J. (2005), SSP300 - Resistance to Shuttle Tanker Collision, Report 2005-02, Amdahl ALS Engineering.

Anderson, T. L. (2005), 'Fracture mechanics: fundamentals and applications'.

Børvik, T., Hopperstad, O. S. & Langseth, M. (2017), TKT4128 Impact Mechanics - Part 2: An Introduction to Penetration and Perforation Mechanics. NTNU, Department of Structural Engineering.

Canship Ugland Ltd (2017), 'M/T Jasmine Knutsen'.
**URL:** *http://www.canship.com/nl/vessels/mt-jasmine-knutsen/*

Chen, H. & Moan, T. (2004), 'Probabilistic modeling and evaluation of collision between shuttle tanker and FPSO in tandem offloading', *Reliability Engineering and System Safety* **84**(2), 169–186.

DNV (2016), 'Rules for classification of ships: Part 5 chapter 1: Ships for navigation in ice'. Det Norske Veritas AS.
**URL:** *http://rules.dnvgl.com/docs/pdf/dnv/rulesship/2016-01/ts501.pdf*

DNV-GL (2016), 'Best practice for hull modelling in Sesam GeniE v7'.

DNV-RP-C204 (2010), 'Design Against Accidental Loads'.

Eni-Norway (2017), 'Goliat'.
**URL:** *http://www.eninorge.com/no/Feltutbygging/Goliat/Fartoy/*

Hallquist, J. O. (2006), *LS-DYNA Theory manual*, Livermore Software Technology Corporation.

Haufe, A., Schweizerhof, K. & DuBios, P. (2013), *Properties & Limits: Review of Shell Element Formulations*, Livermore Software Technology Corporation.

Hopperstad, O. S. & Børvik, T. (2017), TKT4128 Impact Mechanics - Part 1: Modelling of plas-

ticity and failure with explicite finite element methods. NTNU, Department of Structural Engineering.

K. Lundborg, M. E. (2014), 'Human Technical Factors in FPSO-Shuttle Tanker interactions and their influence on the Collision Risk during Operations in the North Sea'.
**URL:** *http://hdl.handle.net/11250/238885*

Knutsen OAS Shipping (2018), 'General specifications of M/T Jasmine Knutsen'.
**URL:** *https://knutsenoas.com/shipping/shuttle-tankers/jasmine-knutsen/*

Langseth, M., Clausen, A. H., & Børvik, T. (2017), TKT4128 Impact mechanics - Part 3: Impact and Energy Absorption. NTNU, Department of Structural Engineering.

Liu, Z. & Amdahl, J. (2010), 'A new formulation of the impact mechanics of ship collisions and its application to a ship-iceberg collision', *Marine Structures* **23**(3), 360–384.
**URL:** *http://search.proquest.com/docview/1671530772/*

Liu, Z. & Amdahl, J. (n.d.), 'On multi-planar impact mechanics in ship collisions'. Note: To be published in the journal Marine Structures.

LSTC and DYNAmore (2018*a*), 'LS-DYNA Support: Contact modeling in LS-DYNA'.
**URL:** *https://www.dynasupport.com/tutorial/contact-modeling-in-ls-dyna*

LSTC and DYNAmore (2018*b*), 'LS-DYNA Support: Differences between implicit ans explicit'.
**URL:** *https://www.dynasupport.com/faq/general/what-are-the-differences-between-implicit-and-explicit*

LSTC and DYNAmore (2018*c*), 'LS-DYNA Support: Mass scaling'.
**URL:** *https://www.dynasupport.com/howtos/general/mass-scaling*

Ma, M. (2014), 'Damage Assessment of Sevan FPSO Subjected to Impacts From Shuttle Tankers'.
**URL:** *http://hdl.handle.net/11250/239248*

Moan, T. (2003), *Finite element modelling and analysis of marine structures*, Vol. UK-03-98 of *Kompendium (Norges teknisk-naturvitenskapelige universitet. Institutt for marin teknikk)*, Akademika forlag, Trondheim.

Moan, T., Amdahl, J. & Ersdal, G. (2017), 'Assessment of ship impact risk to offshore structures - New NORSOK N-003 guidelines', *Marine Structures* .

Norrbin, N. H. (1971), *Theory and observations on the use of a mathematical model for ship manoeuvring in deep and confined waters*, Vol. 68 of *Meddelanden (Statens skeppsprovningsanstalt)*, Göteborg.

NORSOK-N004 (2004), 'Design of steel structures. rev.'.

Pettersen, T. A. (2008), 'Bow Collision Analysis of the Ulstein PX105 Supply Vessel'.

Popov, Y. N., Faddeev, O. V., Kheisin, D. E. & Yakovlev, A. A. (1969), 'Strength of ships sailing in ice', p. 232.

Sevan Marine ASA (2017). Personal communication with Tord Broms Thorsen and Audun Arnesen Nyhus.

Steensen, A. J. (2009), 'Derfor ble Sevan valgt ; Goliat-utbyggingen', *Teknisk ukeblad* **156**(6), 16–17.
**URL:** *https://www.tu.no/artikler/derfor-ble-sevan-valgt/238081*

Storheim, M. (2016), 'Structural response in ship-platform and ship-ice collisions'.

Stronge, W. (2004), *Impact Mechanics*, Cambridge University Press.

Törnqvist, R. (2003), 'Design of crashworthy ship structures'.

Tvedt, E. F. (2014), 'Risk modelling of collision between supply ships and oil- and gas installations'.
**URL:** *http://hdl.handle.net/11250/240968*

Vinnem, J. E., Utne, I. B. & Schjølberg, I. (2015), 'On the need for online decision support in fpso–shuttle tanker collision risk reduction', *Ocean Engineering* **101**, 109–117.

Young, H. D. & Freedman, R. A. (2011), *University Physics with Modern Physics*, Vol. 1, 13th edition edn, Pearson Education Limited.

Yu, Z. (2017), 'Hydrodynamic and structural aspects of ship collisions'.

Yu, Z. & Amdahl, J. (2016), 'Full six degrees of freedom coupled dynamic simulation of ship collision and grounding accidents', *Marine Structures* **47**, 1–22.
**URL:** *http://search.proquest.com/docview/1790930160/*

Yu, Z., Amdahl, J. & Storheim, M. (2016), 'A new approach for coupling external dynamics and internal mechanics in ship collisions', *Marine Structures* **45**, 110–132.
**URL:** *http://search.proquest.com/docview/1758357157/*

# Appendix A

# Added Mass Factors and Radius of Gyration

Popov et al. (1969) derived a series of empirical equations for determining added mass factors and radius of gyration for ships. In this thesis, equation (A1) - (A9) were used to estimate the hydrodynamic coefficients of the shuttle tanker and the supply vessel.

**Added mass factors:**

$$\hat{m}_x = 0 \tag{A1}$$

$$\hat{m}_y = 2 * \frac{T}{B} \tag{A2}$$

$$\hat{m}_x = \frac{2}{3} \frac{BC_{wp}^2}{TC_b\left(1 + C_{wp}\right)} \tag{A3}$$

$$\hat{j}_{xx} = 0.25 \tag{A4}$$

$$\hat{j}_{yy} = \frac{B}{T\left(3 - 2C_{wp}\right)\left(3 - C_{wp}\right)} \tag{A5}$$

$$\hat{j}_{zz} = 0.3 + 0.05\frac{L}{B} \tag{A6}$$

**Radius of gyration:**

$$\hat{R}_{xx}^2 = \frac{C_{wp}B^2}{11.4C_m} + \frac{H^2}{12} \tag{A7}$$

$$\hat{R}_{yy}^2 = 0.07C_{wp}L^2 \tag{A8}$$

$$\hat{R}_{zz}^2 = \frac{L^2}{16} \tag{A9}$$

Here, $T$ is the height of the ship, $B$ is the width of the ship, $L$ is the length of the ship, $C_{wp}$ is the water plane coefficient, $C_b$ is the block coefficient and $C_m$ is the midship section coefficient.

# Appendix B

# Additional Force-Deformation Curves

The force-deformation curves in figure B.1, B.2, B.3 and B.4 are derived by sampling nodal displacements directly from the NLFEA in LS-DYNA. The nodes were selected based on the assumption that they constitute a good representation of the structural deformation. The node sampling approach gave quite similar results to the equivalent deformation approach used in chapter 7.

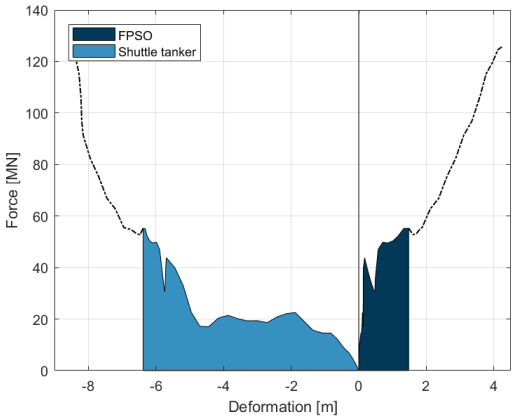


Figure B.1: Shuttle tanker - FPSO collision: Central impact in scenario 1

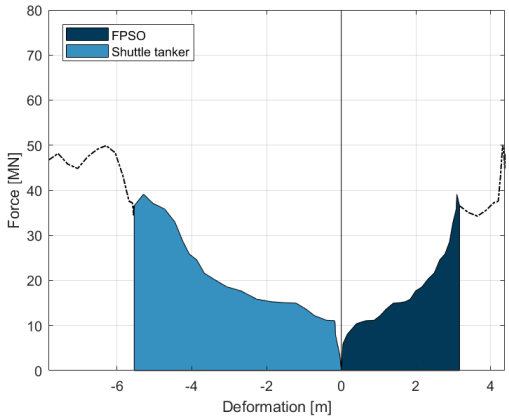


Figure B.2: Shuttle tanker - FPSO collision: Central impact in scenario 2

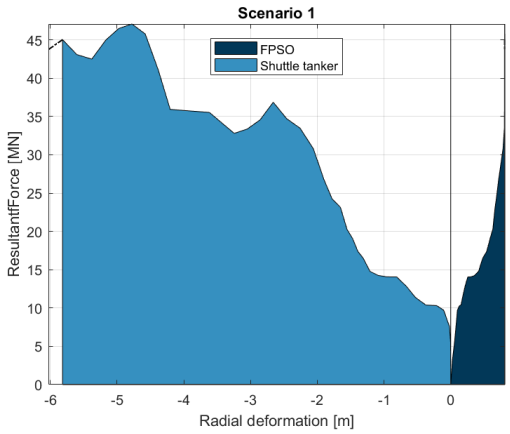


Figure B.3: Shuttle tanker - FPSO collision: 30-degree impact in scenario 1

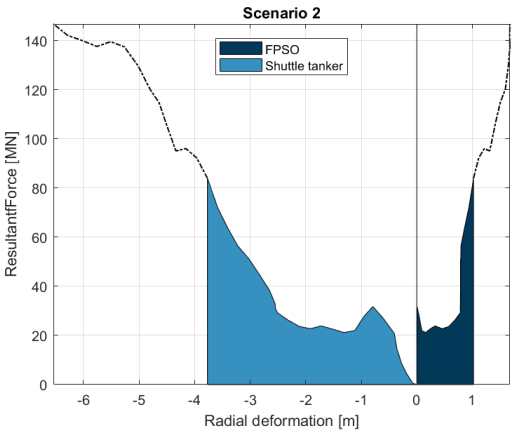


Figure B.4: Shuttle tanker - FPSO collision: 30-degree impact in scenario 2

# Appendix C

# LS-DYNA Keyword Control File

```
*KEYWORD
*TITLE
$#                                                                         title
Sevan 1000 - Shuttle Tanker collision
$ ------------------------------------ CONTROLS ------------------------------------
*CONTROL_ACCURACY
$#      osu       inn    pidosu      iacc
         0         2         0         0
*CONTROL_BULK_VISCOSITY
$#       q1        q2      type     btype
        1.5      0.06        -1         0
*CONTROL_CONTACT
$#   slsfac    rwpnal    islchk    shlthk    penopt    thkchg     orien   enmass
        0.1       1.0         1         0         1         0         1        0
$#   usrstr    usrfrc     nsbcs    interm     xpene    ssthk      ecdt  tiedprj
         0         0         0         0       4.0         0         0        0
$#    sfric     dfric       edc       vfc        th     th_sf    pen_sf
         0.0       0.0       0.0       0.0       0.0       0.0       0.0
$#   ignore    frceng   skiprwg   outseg   spotstp   spotdel   spothin
         1         0         0         0         0         0       0.0
$#     isym    nserod    rwgaps    rwgdth     rwksf      icov    swradf    ithoff
         0         0         1       0.0       1.0         0       0.0         0
$#   shledg    pstiff    ithcnt    tdcnof     ftall    unused    shltrw
         0         0         0         0         0              0.0
*CONTROL_DYNAMIC_RELAXATION
$#   nrcyck      drtol     drfctr    drterm     tssfdr    irelal     edttl    idrflg
        250      0.001      0.995       0.0       0.0         0      0.04      -999
*CONTROL_ENERGY
$#      hgen      rwen     slnten     rylen
         2         2          2         2
*CONTROL_HOURGLASS
$#       ihq        qh
```

```
         4       0.03
*CONTROL_MPP_DECOMPOSITION_CONTACT_DISTRIBUTE
$#      id1       id2       id3       id4       id5
         1         2         3         0         0
*CONTROL_MPP_IO_LSTC_REDUCE
*CONTROL_MPP_IO_NODUMP
*CONTROL_SHELL
$#   wrpang     esort     irnxx    istupd    theory       bwc     miter      proj
      20.0         0        -1         0         2         2         1         0
$#  rotascl    intgrd    lamsht    cstyp6    tshell
       1.0         0         0         1         0
$#  psstupd   sidt4tu      cntco    itsflg    irquad    w-mode   stretch      icrq
         0         0         0         0         2       0.0       0.0         0
$#   nfail1    nfail4   psnfail    keepcs     delfr   drcpsid   drcprm
         0         0         0         0         0         0       1.0
*CONTROL_SOLUTION
$#      soln       nlq     isnan     lcint
         0         0         1      1001
*CONTROL_TERMINATION
$#   endtim    endcyc     dtmin    endeng    endmas
       2.0         0       0.0       0.0       0.0
*CONTROL_TIMESTEP
$#   dtinit    tssfac      isdo    tslimt     dt2ms      lctm     erode     ms1st
       0.0       0.9         0       0.0-2.5000E-6         0         0         0
$#   dt2msf   dt2mslc     imscl    unused    unused     rmscl
       0.0         0         0                         0.0
$ ---------------------------------- DATABASE ----------------------------------
*DATABASE_GLSTAT
$#      dt    binary      lcur     ioopt
     0.05         2         0         1
*DATABASE_MATSUM
$#      dt    binary      lcur     ioopt
     0.05         2         0         1
*DATABASE_RCFORC
$#      dt    binary      lcur     ioopt
     0.05         2         0         1
*DATABASE_SLEOUT
$#      dt    binary      lcur     ioopt
     0.05         2         0         1
*DATABASE_SPCFORC
$#      dt    binary      lcur     ioopt
     0.05         2         0         1
*DATABASE_SSSTAT
$#      dt    binary      lcur     ioopt
     0.05         2         0         1
*DATABASE_BINARY_D3PLOT
$#      dt      lcdt      beam     npltc     psetid
```

```
      0.05         0         0         0         0
$#    ioopt
         0
*DATABASE_EXTENT_BINARY
$#    neiph     neips    maxint    strflg    sigflg    epsflg    rltflg    engflg
         0         0         3         0         1         1         1         1
$#  cmpflg    ieverp    beamip     dcomp      shge     stssz    n3thdt   ialemat
         0         0         0         1         1         1         2         1
$# nintsld   pkp_sen      sclp     hydro    msscl     therm    intout    nodout
         0         0       1.0         0         0         0
$#     dtdt    resplt     neipb
         0         0         0
*DATABASE_FORMAT
$#    iform    ibinary
         0         0
$ ------------------------------ Bounadry conditions --------------------------------
*BOUNDARY_PRESCRIBED_MOTION_SET_ID
$#       id                                                               heading
         1Ship Motion
$#     nsid       dof       vad      lcid        sf       vid     death     birth
         5         1         0         1       1.0          01.00000E28       0.0
*BOUNDARY_SPC_SET_ID
$#       id                                                               heading
         1BC_FPSO
$#     nsid       cid      dofx      dofy      dofz     dofrx     dofry     dofrz
         2         0         1         1         1         1         1         1
$ ---------------------------------- CONTACT ----------------------------------------
*CONTACT_AUTOMATIC_SURFACE_TO_SURFACE_ID
$#      cid                                                                title
         1FPSO - Ship
$#     ssid      msid     sstyp     mstyp    sboxid    mboxid       spr       mpr
         2         1         2         2         0         0         1         2
$#       fs        fd        dc        vc       vdc   penchk        bt        dt
       0.3       0.0       0.0       0.0       0.0         0          0.01.00000E20
$#      sfs       sfm       sst       mst      sfst      sfmt       fsf       vsf
       1.0       1.0       0.0       0.0       1.0       1.0       1.0       1.0
*CONTACT_AUTOMATIC_SINGLE_SURFACE_ID
$#      cid                                                                title
         2FPSO - Internal
$#     ssid      msid     sstyp     mstyp    sboxid    mboxid       spr       mpr
         1         0         2         0         0         0         0         0
$#       fs        fd        dc        vc       vdc   penchk        bt        dt
       0.3       0.0       0.0       0.0       0.0         0          0.01.00000E20
$#      sfs       sfm       sst       mst      sfst      sfmt       fsf       vsf
       1.0       1.0       0.0       0.0       1.0       1.0       1.0       1.0
*CONTACT_AUTOMATIC_SINGLE_SURFACE_ID
$#      cid                                                                title
```

```
          3Ship  Intern
$#     ssid        msid       sstyp       mstyp      sboxid      mboxid         spr         mpr
         2           0           2           0           0           0           0           0
$#       fs          fd          dc          vc         vdc     penchk          bt          dt
       0.3         0.0         0.0         0.0         0.0           0        0.01.00000E20
$#      sfs         sfm         sst         mst        sfst        sfmt         fsf         vsf
       1.0         1.0         0.0         0.0         1.0         1.0         1.0         1.0
$ ---------- MATERIAL MODELS ----------
*MAT_USER_DEFINED_MATERIAL_MODELS_TITLE
User_Material
$#      mid          ro          mt         lmc         nhv      iortho       ibulk          ig
         17.83000E-9          46          10           3           0           4           3
$#    ivect       ifail      itherm      ihyper        ieos        lmca      unused      unused
         1           1           0           0           0           0
$#       p1          p2          p3          p4          p5          p6          p7          p8
  207000.0         0.3     79615.4    172500.0       235.0       670.0        0.24         0.0
$#       p1          p2          p3          p4          p5          p6          p7          p8
      0.71         1.0         0.0         0.0         0.0         0.0         0.0         0.0
*MAT_RIGID_TITLE
Rigid_Material
$#      mid          ro           e          pr           n      couple           m       alias
         27.83000E-8  207000.0         0.3         0.0         0.0         0.0
$#      cmo        con1        con2
       1.0           5           7
$#lco or a1          a2          a3          v1          v2          v3
       0.0         0.0         0.0         0.0         0.0         0.0
$ ---------- INITIAL VELOCITY ----------
$ Can be used to reduce initial stress concentrations in the ship (not used)
*INITIAL_VELOCITY
$#     nsid      nsidex       boxid      irigid        icid
$         3           0           0           0           0
$#       vx          vy          vz         vxr         vyr         vzr
$    5000.0         0.0         0.0         0.0         0.0         0.0
$ ---------- CURVE ----------
*DEFINE_CURVE_TITLE
VelocityProfile
$#     lcid        sidr         sfa         sfo        offa        offo      dattyp       lcint
         1           0         1.0         1.0         0.0         0.0           0           0
$#                   a1                      o1
                    0.0                  5000.0
                   10.0                  5000.0
$ ---------- VECTOR ----------
*DEFINE_VECTOR_TITLE
Ship_direction
$#      vid          xt          yt          zt          xh          yh          zh         cid
         1         0.0         0.0         0.0         1.0         0.0         0.0           0
$ ---------- DAMPING ----------
```

```
*DAMPING_GLOBAL
$#     lcid      valdmp        stx        sty        stz        srx        sry        srz
         0         0.0        0.0        0.0        0.0        0.0        0.0        0.0
$ ---------- INCLUDE GEOMETRY ----------
*INCLUDE
SevanFPSO_MainHull.key
ShuttleTanker_V18.key
$ ------------------------------------------------------------------------------
*END
```

# Appendix D

# External Mechanics MATLAB Script

```
clear
close all
clc

%% ============= External dynamicis: Ship - FPSO collision ===============
% ========================================================================
% ------------------------------------------------------------------------
%           Stronge3d-function made by: Dr. Z. Liu, March, 2013
%           Input script by:            S.A. Hagen, April, 2018
% ------------------------------------------------------------------------

%   Object A: FPSO
%   Object B: Shuttle tanker


%% ======================== Impact scenario ============================
    angle = 30;                     % [deg.]    Impact angle
    Vel   = 1.9;                    % [m/s]     Impact velocity

% ========================================================================
%                               FPSO data
% ========================================================================
% Type: Sevan 1000
Ha = 42.00;             % [m]   Height      (main deck)
Da = 93.0;              % [m]   Diameter    (Main hull - Ballast)
%Da = 104.0;            % [m]   Diameter    (Main deck - Full load)
Ta = 20.00;             % [m]   Draft       (Ballast WL)
%Ta = 28.30;            % [m]   Draft       (Full load WL)
Cxa = 0;                % [m]   COG x
Cya = 0;                % [m]   COG y
Cza = 27.7;             % [m]   COG z       (Ballast, from bottom)
%Cza = 26.1;            % [m]   COG z       (Full load, from bottom)
```

```
33 Zga = Ta - Cza;          % [m]   Vertical distance from waterline to COG
34 %m_fpso = 215.0E6;       % [kg]  FPSO mass   (Fully loaded)
35 m_fpso = 155.0E6;        % [kg]  FPSO mass   (Ballast)
36
37 % Assumed added mass factors:
38 Amx = 1.0;                          %       Surge
39 Amy = 1.0;                          %       Sway
40 Amz = 1.0;                          %       Heave
41 Am = [Amx,Amy,Amz];
42 Amrol = 1.0;                        %       Roll
43 Ampit = 1.0;                        %       Pitch
44 Amyaw = 1.0;                        %       Yaw
45 Amr=[Amrol,Ampit,Amyaw];
46
47 % Inertia radius squared:
48 Ixx = (1/12)*m_fpso*(3*(93/2)^2 + Ha^2);    % mass moment of inetria
49                                              % for cylinder (= Iyy).
50 rxa = Ixx/m_fpso;          % [m^2]
51 rya = Ixx/m_fpso;          % [m^2]
52 rza = 0.5*(93/2)^2;        % [m^2]          Main hull diameter = 93.0 m
53 Ra  = [rxa,rya,rza];
54
55 % Writing out FPSO data:
56 fprintf('\n---------------- FPSO data ----------------\n');
57 fprintf('Inertia radius squared: \n');
58 fprintf('\tRoll   [m^2]   = %f\n', rxa);
59 fprintf('\tPitch  [m^2]   = %f\n', rya);
60 fprintf('\tYaw    [m^2]   = %f\n', rza);
61 fprintf(' ------------------------------------\n');
62 fprintf('\tRoll   [m]     = %f\n', sqrt(rxa));
63 fprintf('\tPitch  [m]     = %f\n', sqrt(rya));
64 fprintf('\tYaw    [m]     = %f\n', sqrt(rza));
65 fprintf(' ------------------------------------\n');
66
67 % ========================================================================
68 %                          Shuttle tanker data
69 % ========================================================================
70 % Type: Samsung, Jasmine Knutsen
71 Hb  = 28.600;              % [m]   Height (from FEM model)
72 Lb  = 262.00;              % [m]   Length
73 Bb  = 46.00;               % [m]   Breadth
74 %Tb  = 9.3;                % [m]   Draft Ballast
75 Tb  = 19.0;                % [m]   Draft design (fully loaded)
76 m_ship = 150E06;           % [kg]  Tanker mass (fully loaded)
77 %m_ship = 90E06;           % [kg]  Tanker mass (ballast)
78 Cxb = Lb/2;                % [m]   CoG x (assumed)
79 Cyb = 0;                   % [m]   CoG y (assumed)
```

```
80  Czb = 12.650;              % [m]   CoG z (assumed), Ballast + Full load
81                             %                  -> from bottom of ship
82  Zgb = Tb - Czb;            % [m]   Vertical distance from water line to CoG
83  Cwp = 0.9;                 % [-]   Waterplane coefficent
84  Cm  = 0.9;                 % [-]   Mid-section coefficient
85  Cb  = 0.8;                 % [-]   Block cooeficent
86
87  % Added mass factors (purely empirical):
88  Bmx = 0.0;                                  %       Surge
89  Bmy = 2*Tb/Bb;                              %       Sway
90  Bmz = 2/3*Bb*Cwp^2/(Tb*Cb*(1+Cwp));         %       Heave
91  Bm = [Bmx,Bmy,Bmz];
92  Bmrol = 0.25;                               %       Roll
93  Bmpit = Bb/(Tb*(3-2*Cwp)*(3-Cwp));          %       Pitch
94  Bmyaw = 0.3 + 0.05*(Lb/Bb);                 %       Yaw
95  Bmr=[Bmrol,Bmpit,Bmyaw];
96
97  % Inertia radius squared:
98  rxb = (Cwp*Bb^2)/(11.4*Cm)+Hb^2/12;         %       Rx^2
99  ryb = 0.07*Cwp*Lb^2;                        %       Ry^2
100 rzb = Lb^2/16;                             %       Rz^2
101 Rb = [rxb,ryb,rzb];
102
103 fprintf('---------------- Tanker data ------------------\n');
104 fprintf('Added mass factor:\n');
105 fprintf('\tAmx    = %f\n', Bmx);
106 fprintf('\tAmy    = %f\n', Bmy);
107 fprintf('\tAmz    = %f\n', Bmz);
108 fprintf('\tRoll   = %f\n', Bmrol);
109 fprintf('\tPitch  = %f\n', Bmpit);
110 fprintf('\tYaw    = %f\n', Bmyaw);
111
112 % Writing out inertia radius for tanker:
113 fprintf('Inertia radius squared: \n');
114 fprintf('\tRoll   [m^2]     = %f\n', rxb);
115 fprintf('\tPitch  [m^2]     = %f\n', ryb);
116 fprintf('\tYaw    [m^2]     = %f\n', rzb);
117 fprintf(' - - - - - - - - - - - - - - - - - - - - - - - -\n');
118 fprintf('\tIxx    [tonn*mm^2] = %e\n', rxb*m_ship*1E3);
119 fprintf('\tIyy    [tonn*mm^2] = %e\n', ryb*m_ship*1E3);
120 fprintf('\tIzz    [tonn*mm^2] = %e\n', rzb*m_ship*1E3);
121 fprintf(' - - - - - - - - - - - - - - - - - - - - - - - -\n');
122 fprintf('Inertia radius: \n');
123 fprintf('\tRoll   [m]      = %f\n', sqrt(rxb));
124 fprintf('\tPitch  [m]      = %f\n', sqrt(ryb));
125 fprintf('\tYaw    [m]      = %f\n', sqrt(rzb));
126 fprintf(' - - - - - - - - - - - - - - - - - - - - - - - -\n');
```

```
127
128 %% ======================== Contact surface ============================
129 % FPSO in ballast:
130 alpha = 90*cosd(angle); % [deg] Waterline angle
131 gama = 0;                % [deg] The angle between body frame A and B
132 betap = 0;               % [deg] The normal frame angle
133 % FPSO in full load:
134 %alpha = 90*cosd(angle);% [deg] Waterline angle
135 %gama = 0;               % [deg] The angle between body frame A and B
136 %betap = -26.6;          % [deg] The normal frame angle
137
138 % Collision point under tanker's body frame:
139 % Collision point under FPSO's body frame:%
140 cp_a = [-(Da/2)*cosd(angle)                  % x-coordinate
141         -(Da/2)*sind(angle)                  % y-coordinate
142         -(Cza-3.25)];                        % z-coordinate (ballast)
143                                              % Height BB: 3.25 m
144 % Assuming semicircle bow (in the horizontal plane)
145 cp_b = [(Lb/2 - (Bb/2)*(1 - cosd(angle)))   % x-coordinate
146         (Bb/2)*sind(angle)                   % y-coordinate
147         -Czb];                               % z-coordinate (fully loaded)
148
149 %% ======================== Impact velocity ============================
150 % Velocity of FPSO under FPSO's body frame:
151 ve_a = [0 0 0]';   %[m/s]     [Vx Vy Vz]
152
153 % Velocity of ship under ship's body frame:
154 ve_b = [Vel 0 0]'; %[m/s]     [Vx Vy Vz]
155
156 %% ========================== Friction ================================
157 % Static friction between ship and FPSO:
158 %   Steel-to-steel factor = 0.3
159 %   tangential deformation factor (equivalent) = 0.3
160 %   => Efficient friction factor = 0.6
161 miu0 = 0.6;
162
163 % Restitution factor e (0 = plastic, 1 = elastic):
164 res = 0;
165
166 %% ======================== Run analysis ==============================
167 % INFO: the "strong3d()" subroutine is available from the Department of
168 % Marine Technology at Norwegian University of Science and Technology
169 % (NTNU)
170
171 [tt,ttm,dvv,ve_af,ve_bf,flag,miu,mass1,mass2] = ...
172     stronge3d(m_fpso,m_ship,Am,Bm,Amr,Bmr,Ra,Rb,alpha,gama,...
173     betap,cp_a,cp_b,res,miu0,ve_a,ve_b);
```

```
174
175 % OUTPUT PARAMETERS:
176 % tt     : total dissipated energy [J]
177 % ttm    : an array for dissipated energy in each direction [J]
178 % dvv    : relative velocity increase under the local frame n1n2n3
179 % ve_af : velocity after impact of object a under body frame of object a
180 % ve_bf : velocity after impact of object b under body frame of object b
181 % flag   : stick (1) or slide (2)
182 % miu    : static friction factor between object a and b
183 % mass1 : mass matrix for object a
184 % mass2 : mass matrix for object b
185
186 %% ============================ RESULTS ================================
187 ve_af = double(ve_af);
188 ve_bf = double(ve_bf);
189 % ---------------------- Write out results ------------------------
190 fprintf('\n\n------------------ RESULTS ------------------\n');
191 fprintf('Total dissipated energy:\n');
192 fprintf('\tE_tot [MJ]  = %6.2f\n', tt*1E-06);
193 fprintf('\nDissipated energy in each direction');
194 fprintf('(local coordinate system):\n');
195 fprintf('\tEx    [MJ]  = %6.2f\n', ttm(1)*1E-06);
196 fprintf('\tEy    [MJ]  = %6.2f\n', ttm(2)*1E-06);
197 fprintf('\tEz    [MJ]  = %6.2f\n\n', ttm(3)*1E-06);
198 fprintf('\tEr    [MJ]  = %6.2f   (Parallel to impact surface)\n', ...
199     (ttm(1) + ttm(2))*1E-06);
200 fprintf('\tEz    [MJ]  = %6.2f   (Perpendicular to impact surface)\n', ...
201     ttm(3)*1E-06);
202 fprintf('\nFPSO velocity after impact:\n');
203 fprintf('\tVx    [m/s] = %f\n', ve_af(1));
204 fprintf('\tVy    [m/s] = %f\n', ve_af(2));
205 fprintf('\tVz    [m/s] = %f\n', ve_af(3));
206 fprintf('\nShip velocity after impact:\n');
207 fprintf('\tVx    [m/s] = %f\n', ve_bf(1));
208 fprintf('\tVy    [m/s] = %f\n', ve_bf(2));
209 fprintf('\tVz    [m/s] = %f\n', ve_bf(3));
210
211 fprintf('\nImpact type:\n');
212 fprintf('\tCase: %s\n', flag);
213 fprintf('\tNormal friction coeffisient:');
214 fprintf('%f (static friction factor?)\n', miu);
215
216 % END OF INPUT-SCRIPT
```